Spectroscopy of ^{257,258}Db in the vicinity of the N=152 deformed shell gap

M. Vostinar

UNIVERSITÉ CAEN NORMANDIE

Normandie Université

Université de Caen Normandie
U.F.R. de Sciences
École doctorale SIMEM

Thèse de doctorat

présentée et soutenue le: 23. novembre 2015.

par

Mme Marija Voštinar

pour obtenir le

Doctorat de l'Université de Caen Normandie

Spécialité: Constituants élémentaires et physique théorique

Spectroscopy of ^{257,258}Db in the vicinity of the N=152 deformed shell gap

Directeur de thèse : *Hervé Savajols*

GANIL spiral2 laboratoire commun CEA/DSM CNRS/IN2P3

Jury

Dr Rolf-Dietmar Herzberg	Professor, The University of Liverpool	(Rapporteur)
Dr Benoît Gall	Professeur, IPHC - Université de Strasbourg	(Rapporteur)
Dr Francesca Gulminelli	Professeur, Université de Caen Normandie	(Examinateur)
Dr Araceli Lopez-Martens	Directeur de Recherche CNRS	(Examinateur)
Dr Héloïse Goutte	Ingénieur Chercheur CEA	(Examinateur)
Dr Hervé Savajols	Chargé de Recherche CNRS	(Directeur)

GANIL T 2015 04

Contents

Acknowledgments

I would like to thank Rolf-Dietmar Herzberg and Benoît Gall for accepting to be my referees as well as Francesca Gulminelli, Araceli Lopez-Martens and Héloïse Goutte for accepting to be the members of the jury.

Next, I would like to thank my original supervisors Herve Savajols and Julien Pancin for giving me an opportunity to do a thesis. For all of their guidance, support and help, and of course friendship. I have learned a lot in these three years, but I have also changed a lot as well.

I would like to give a special thanks to Fritz Peter Heßberger for giving me the data on ^{258}Db, and for accepting me as his own student. I know it was not easy, but I have learned a lot!

Additionally, I would like to thank Julien Piot for agreeing to share the experiment of ^{257}Db with me and giving me the data for the thesis. Moreover, I would like to thank Christelle Stodel for all the help and useful advices especially in the last year of the thesis. As well Dieter Ackermann for providing the MoDSS, it provided a unique opportunity to work with latest detector systems and electronics and corresponding analysis and acquisition codes. Once more Waely (Araceli Lopez-Martens) for useful advices concerning the analysis especially at the begging and the help during GANIL experiments.

A special thanks to Alex for surviving this with me, for teaching me how to program and for all the support and understanding.

I would also like to thank the people of physics group at GANIL as well as the technicians both at GANIL and at GSI. All the five experiments, and some offline tests, would have not been the same without all of you.

Finally I would like to thank all the students and post-docs, without you it would have not been as fun! A special thanks for Florent, Jose-Luis, Bego, Marine, Andrew and Julia you become a part of my life.

And last but not the least to my family for all the support and understanding during all of these years. It was a long journey.

Introduction

The existence of specific numbers of protons and neutrons which give extra stability to the nuclei was observed for the first time in 1934 by W. Elsasser [1]. This stability was explained by the presence of an important energy gap where the last levels before the gap are completely filled with protons or neutrons and the levels after are completely empty. However, at that time, the existing theoretical models were able to reproduce only the first three "magic" numbers (2, 8 and 20). The problem was solved in 1948 when M. Goeppert-Mayer and O. Haxsel, J.H.D. Jansen and H.E. Suess [2, 3] modified the existing shell model by adding a spin orbit term to the effective potential used to describe the structure of a nucleus. Since then the search for the next "magic" number (shell closure) has been one of the main research topics in nuclear physics.
Theoretically the next shell closure is predicted to be in the vicinity of the superheavy (Z>104) elements. However its exact position differs from one model to the other. These differences arise due to the incomplete understanding of the physics processes responsible for the formation and stability of transfermium ($Z > 100$) nuclei. Indeed according to the macroscopic models, nuclei are no longer stable beyond proton numbers around $Z = 100$. For these nuclei the long range repulsive Coulomb potential of the positively charged protons inside the nucleus is enough to overcome the short range attractive strong nuclear force, thus making the nucleus unstable. However, transfermium nuclei have been observed experimentally [4]. These elements owe their existence to their underlying shell structure. Detailed spectroscopic studies of the structure of transfermium nuclei can shade light on the mechanisms that cause the stability of the heaviest elements permitting a better parametrization of the theoretical models.
A region of enhanced stability was observed for nuclei with neutron number around $N = 152$ [5]. Theoretically a deformed neutron shell gap at $N = 152$ is formed due to the splitting of the $i_{11/2}$ and $j_{15/2}$ orbitals. It should be noted that the production of such elements faces significant technical limitations caused by the low production cross sections. Nevertheless, the size [6] and the strength [7] of this gap were experimentally determined, as well as its influence on nuclei like $^{255}_{103}Lr_{152}$ [8] and $^{256}_{104}Rf_{152}$ [9, 10]. Valuable information on the existence of superheavy elements

can be obtained by studying the evolution of the $N = 152$ deformed shell gap for nuclei heavier than $^{256}_{104}$Rf, such as $_{105}$Db for example.

The first chapter of this thesis follows the evolution of the theoretical models used to describe the nucleus, up to the modern ones which include the transfermium region. Additionally, the description is given on the known properties of the heavy and superheavy elements such as their: shapes, organization of their shells and decay modes.

The second chapter concentrates on the explanation of the theoretical and experimental aspects of the fusion-evaporation reaction, the process used for the production of transfermium elements. A detailed description of the two facilities, in which the isotopes presented in this thesis were synthesized, is given. Additionally the new generation facility S^3 (the Super Separator Spectrometer), currently under construction, is described. This facility will address the technical difficulties connected to the production of the heaviest elements, providing higher rates and better detection systems.

The third chapter is dedicated to the description of the new tracking detector which will be installed at S^3 and used for the spectroscopy studies of superheavy elements. Physics processes governing the working principle of a gas detector are explained at the beginning of the chapter. They are followed by the description of the developed detector prototypes. The end of the chapter is dedicated to the discussion on the current performances of these detectors as well as on the improvements achieved so far.

The fourth chapter discusses the results obtained from the study of ^{257}Db. This experiment was performed at GANIL with a goal to determine the energy of the previously observed levels in ^{257}Db and its daughters.

In the last chapter the results obtained from the study of ^{258}Db are discussed. This isotope was produced at GSI to address some open questions left from the previous studies of ^{258}Db isotope.

Introduction

L'existence de nombres bien définis de protons et de neutrons conférant aux noyaux une stabilité accrue a été observée pour la première fois en 1934 par W. Elsasser [1]. Cela s'explique par la présence d'un important gap en énergie entre les derniers niveaux complètement occupés (le cœur) et les premiers niveaux totalement vides (valence). Cependant, les modèles théoriques de l'époque ne permettaient de reproduire que les trois premiers nombres "magiques" (2, 8 et 20). Ce problème a été partiellement résolu en 1948, conjointement par M. Goeppert-Mayer et O. Haxel ainsi que J.H.D. Jansen et H.E. Suess [2,3], en introduisant un terme de spin-orbite au potentiel effectif utilisé par le modèle en couche pour décrire la structure des noyaux. La détermination des prochains nombres "magiques" est alors devenue l'un des principaux sujets de recherche en physique nucléaire.
La fermeture de couche suivante est prédite théoriquement dans la région des éléments super-lourds ($Z > 104$). Cependant, sa position exacte varie d'un modèle à l'autre. Ces différences proviennent du fait que notre compréhension des phénomènes physiques responsables de la formation et de la stabilité des noyaux au-delà du Fermium (transfermium, $Z > 100$) est incomplète. En effet, d'après le modèle macroscopique, les derniers noyaux stables se trouvent à $Z = 100$. Pour ces noyaux, la répulsion Coulombienne à longue portée, crée par les protons à l'intérieur du noyau, est plus importante que l'attraction à courte portée de l'interaction forte. Cependant, des éléments possédant un Z plus élevé que le Fermium ont été produits et étudiés expérimentalement [4]. Ces noyaux doivent leur existence à des interactions sous-jacentes à leur structure. Des études spectroscopiques détaillées des noyaux $Z > 100$ permettraient d'éclairer les zones d'ombres qui demeurent actuellement sur les mécanismes responsables de la stabilité des éléments les plus lourds et ainsi de mieux contraindre les paramètres des modèles théoriques.
Une région de stabilité plus élevée a été observée pour les noyaux dont le nombre de neutron avoisine 152 [5]. De manière théorique, un gap neutron déformé se forme à $N = 152$ du fait de la levée de dégénérescence entre les orbites $i_{11/2}$ et $j_{15/2}$. Il est à noter que l'étude de tels éléments est limitée par une section efficace de production très faible. La taille [6] et la constance [7] de ce gap ont cependant été déterminées expérimentalement, de même que son influence sur les noyaux comme le ^{255}Lr [8] et ^{256}Rf [9, 10]. Des informations capitales sur l'existence des éléments super lourds peuvent être obtenues en s'intéressant à l'évolution de ce gap déformé $N = 152$ pour les noyaux plus lourds que le ^{256}Rf, comme par exemple le $_{105}$Db.

Le premier chapitre de cette thèse suivra l'évolution des modèles théoriques util-

isés pour décrire les noyaux, du modèle de la goutte liquide jusqu'aux modèles contemporains incluant les noyaux transfermium. Une description des propriétés connues des éléments lourds et super lourds (telles que leurs formes, leur structure nucléaire et leur modes de décroissance) est également donnée.

Le second chapitre se concentre sur les aspects théoriques et expérimentaux des réactions de fusion-évaporation, qui est le processus de production des éléments tansfermium. Les deux installations ayant accueillies les expériences lors desquelles les isotopes étudiés dans cette thèse ont été produits sont décrites de manière détaillée. Le spectromètre S^3 (Super Separator Spectrometer) est également exposé. Ce dernier s'attachera à résoudre les difficultés techniques classiquement rencontrées lors de la production des éléments les plus lourds, offrant un taux de production plus élevé et un meilleur système de détection.

Le troisième chapitre est dédié à la description du nouveau détecteur qui sera installé sur S^3 pour suivre la trajectoire des produits, suites à la réaction de fusion-évaporation lors de la production d'éléments super lourds. Les processus physiques régissant le principe de fonctionnement d'un détecteur gazeux y seront expliqués. S'en suivra une description des différents prototypes qui ont été développé pour le moment. Ce chapitre se conclura par une discussion sur les performances actuelles de ces prototypes ainsi que sur les améliorations qui y ont été apportées jusqu'à présent.

Le quatrième chapitre présentera et interprétera les résultats de l'analyse des données obtenues lors de l'expérience sur le ^{257}Db. Celle-ci s'est déroulée au GANIL, avec pour but de déterminer les énergies des états précédemment observés dans le ^{257}Db et ses noyaux fils.

Le dernier chapitre se focalisera sur l'isotope de ^{258}Db, produit à GSI pour tenter de répondre à certaines questions laissées sans réponses par l'étude faite précédemment sur ce noyau. Les résultats obtenus y seront exposés et discutés.

Chapter 1

Physical background

This chapter gives the physics background necessary for the interpretation of the data discussed in the manuscript. In the first section 1.1 the evolution of different theoretical models used to describe the nucleus, up to the modern ones, is given. This is followed by the description of different properties characterizing the heavy and superheavy elements, such as their shapes, organization of their shells (1.2 and 1.4) and decay modes (1.3). The main references used for this chapter are [11–15]. Additional references can be found in the text itself.

1.1 Nuclear models

Many different theories describing the nucleus have been developed since its discovery. This section gives a general overview of some of the main models (shell model, self-consistent mean-field models...) in a chronological way. The last part of the section is dedicated to the models used today for the description of superheavy elements.

1.1.1 Liquid drop model

The oldest model used to describe the nucleus is the Liquid Drop Model (LDM). LDM is a macroscopic theory which considers the nucleus as a charged droplet made of incompressible quantum fluid with constant density. This model allowed prediction of the total energy of the nucleus as well as binding energies, masses and to some extent fission barriers.
The binding energy (B.E.) is defined as the energy required to break up the nucleus into its constituents, protons and neutrons. It is given by Bethe-Weizsäcker formula [16, 17]:

$$B.E. = a_v A - a_s A^{2/3} - a_c Z(Z-1)A^{-1/3} - a_a (N-Z)^2 A^{-1} \pm \delta \qquad (1.1)$$

where Z, N and A refer to proton, neutron and mass number respectively. The last two terms in the equation 1.1 are a consequence of the microscopic nature of the nucleus. The different terms in the equation 1.1 present:

- The volume term $a_v A$ represents the short nuclear force acting on the nucleons inside the nucleus as if all of them are surrounded by infinite number of protons and neutrons. Consequently it has to be corrected for the nucleons on the surface of the nucleus.
- The surface term $a_s A^{2/3}$. The nucleons on the surface of a nucleus with a finite radius experience reduced binding energy due to the fact that they are not completely surrounded by other nucleons.
- The Coulomb term $a_c Z(Z-1)A^{-1/3}$. Positively charged protons in the volume of the nucleus cause a Coulomb repulsion which needs to be taken into account. It can be seen that the term becomes more significant with the increase in the proton number, while the increase of the mass without changing the proton number will reduce its influence.
- The asymmetry energy term $a_a(N-Z)^2 A^{-1}$. Is a non-classical term and it arises from the Pauli exclusion principle.
- The pairing term δ is a consequence of pairing of like nucleons. The even-even nuclei are more stable and δ is positive, for odd-odd nuclei δ is negative and for even-odd (odd-even) δ is zero.

The LDM, defined as such, was able to explain the deviation of the valley of stability from the $N = Z$ to more neutron rich nuclei. Additionally it calculated the binding energy per nucleon for nuclei around the valley of stability with the standard parametrization parameters, a_v, a_s, a_c and a_a determined from fits on the entire chart of nuclei [11]. The binding energy obtained in this way is around 8 MeV per nucleon except for nuclei beyond Fermium (Z=100) where the binding energies are lower and nuclei become unstable against fission. This will be discussed in the following section.

Spontaneous fission

Splitting of a nucleus in highly energetic fragments is called fission. Only the first three terms (volume, surface and Coulomb) of the Bethe-Weizsäcker formula (equation 1.1) contribute to the description of fission. The probability for a nucleus to fission can be described with the fissility parameter, where the probability

increases with the increase of the parameter. The fissility parameter can be defined as [18]:

$$x = \left(\frac{Z^2}{A}\right)\left(\frac{Z^2}{A}\right)^{-1}_{crit} \tag{1.2}$$

the second term $(Z^2/A)_{crit}$ is the critical value at which the spherical shape becomes unstable with the Coulomb repulsion counteracting the effect of the surface tension. The fission probability calculated with LDM for $92 < Z < 110$ can be seen in figure 1.1 as a dashed line. This figure shows that elements with Z>104 ($x \approx 0.88$, for angular momentum zero) should not exist due to the fact that, according to the LDM, the fission barrier vanishes in this region. However these elements were experimentally produced and studied, indicating that the LDM is not taking into account all the phenomena playing a role in the stability of these nuclei. Further investigation of the figure indicates that the LDM systematically underestimates the binding energies for heavy nuclei and is not able to explain the increased stability ("magic numbers") of certain nuclei.

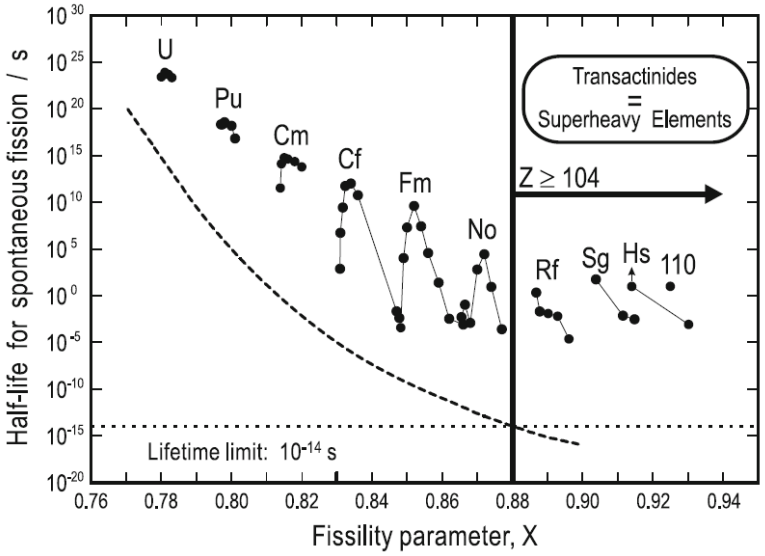

Figure 1.1: Experimental spontaneous fission half-lives for heavy even-even nuclei (circles) compared to the prediction of the LDM as a function of the fissility parameter x (dashed line). The horizontal dotted line shows the minimum lifetime for the formation of a chemical element. Figure adapted from [11].

1.1.2 Shell model

To overcome the drawbacks of the LDM a new model (shell model) based on microscopic effects was introduced. The first shell model was based on the atomic shell model. In the atomic model electrons are moving in orbits in an external central potential created by the nucleus. The electrons do not collide with each other. However the nucleons inside of the nucleus create their own potential in which they move. Consequently, this adopted model was not able to describe certain physical phenomena of the nucleus and was soon modified. The modification of the model was done in 1948, by M. Goeppert-Mayer and O. Haxsel, J. H. D. Jansen and H. E. Suess [2, 3], when a spin-orbit term was added to the isotropic potential in which the nucleons are moving. This model (spherical shell model) was reproducing well the behavior of spherical nuclei with closed shells, but was unable to explain the behavior of all other nuclei. The issue was solved in 1955. when S. G. Nilsson included the deformed nuclei (nuclei outside of the shell closures) in the shell model [19].

Nuclear deformation

Nuclei outside of shell closures do not have a spherical shape, but rather a deformed one. The nuclear deformation can take different forms which depend on the equipotential surface $R(\theta, \phi)$ of the nucleus. It can be expressed in terms of spherical harmonics:

$$R(\theta, \phi) = R_0 \left[1 + \sum_{\lambda=2}^{\infty} \sum_{\mu=-\lambda}^{\lambda} \alpha_{\lambda\mu} Y_{\lambda\mu}(\theta, \phi) \right] \tag{1.3}$$

where θ and ϕ are polar coordinates, R_0 is the the radius of a sphere, $\alpha_{\lambda\mu}$ are coefficients which describe the differences between the equilibrium spherical shape and the deformation. For axially symmetric deformations, with the z-axis as symmetry axis, all $\alpha_{\lambda\mu}$ vanish except for μ=0. These variables $\alpha_{\lambda 0}$ are also called β_λ, ν_λ or ϵ_λ. The notation ϵ_λ will be adopted for the rest of the manuscript. The shape of the nucleus (figure 1.2) depends on the value of the parameter λ ("multipolarity"). For λ=0 the nucleus is spherically symmetric, for λ=2 it has an oblate or prolate shape (quadrupole deformation), λ=3 gives an octupole deformation, etc...

Nilsson model

To reproduce the correct shell structure of deformed nuclei, Nilsson introduced a deformed harmonic oscillator potential:

$$V = \frac{1}{2} M \left(\omega_\perp^2 \left(x^2 + y^2 \right) + \omega_\parallel^2 z^2 \right) - C \overrightarrow{l} \cdot \overrightarrow{s} - D l^2 \tag{1.4}$$

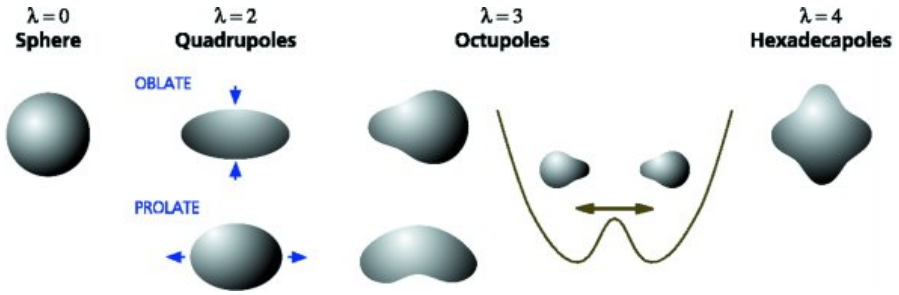

Figure 1.2: Nuclear shapes. Figure adopted from [20].

where z is the symmetry axis, s is the spin and l is the orbital angular momentum of a single particle, C and D are constants, $\omega_\perp$ and $\omega_\parallel$ are oscillator frequencies which defer from each other only if a deformation exists. The deformation parameter (ϵ) was introduced in the following way:

$$\omega_\perp = \omega_0 \left(1 + \frac{1}{3}\epsilon\right) \tag{1.5}$$

$$\omega_\parallel = \omega_0 \left(1 - \frac{2}{3}\epsilon\right) \tag{1.6}$$

where ω_0 is the oscillator frequency for spherical harmonic oscillator and ϵ describes the elongation of the nucleus. The relation between ϵ and the geometric deformation parameter β (see previous section 1.1.2) in the following way $\beta = 1/3\epsilon\sqrt{16\pi/5}$. In the case when $\omega_\perp > \omega_\parallel$ (positive deformation) the nucleus is long and narrow, it has a prolate shape. In the opposite case of negative deformation the nucleus is flat and has an oblate shape. For such a system (deformed nucleus) the quantum number $j = l + s$ is not preserved anymore (figure 1.3). The only preserved quantum numbers are parity π and the projection of the total angular momentum j on the symmetry axis Ω. Each Ω presents a single particle state called Nilsson level. Nilsson levels are usually characterized with asymptotic labels $\Omega^\pi[N, n_z, \Lambda]$:

- Λ and Σ are the projections of orbital angular momentum (l) and the spin (s) on the symmetry axis (figure 1.3). $\Omega = \Lambda \pm \Sigma = \Lambda \pm 1/2$
- N is the main oscillator quantum number, in spherical case it defines the shells
- n_z contains the number of radial nodes in the wave function in z (symmetry axis) direction
- Parity is defined as $\pi = (-1)^N$.

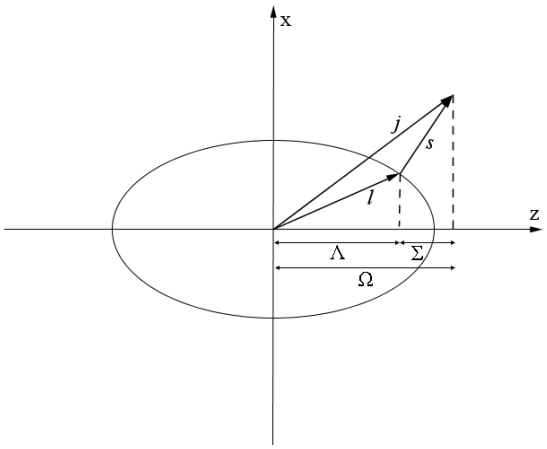

Figure 1.3: The single particle angular momenta s, l and j, and their projection on the symmetry axis (z) Σ, Λ and Ω in axially deformed potential.

The energies of the single particle states can be obtained by solving the Nilsson Hamiltonian. The plot of the energies of the single particle states Ω^{π} as a function of the quadrupole deformation (ϵ_2) of the nucleus is called Nilsson diagram.
For each orbit with angular momentum j there are $2j+1$ values of Ω. Each $\pm\Omega$ state is a two-fold degenerate state, where the low Ω states favor prolate shapes and high Ω states favor oblate shapes (figure 1.4).

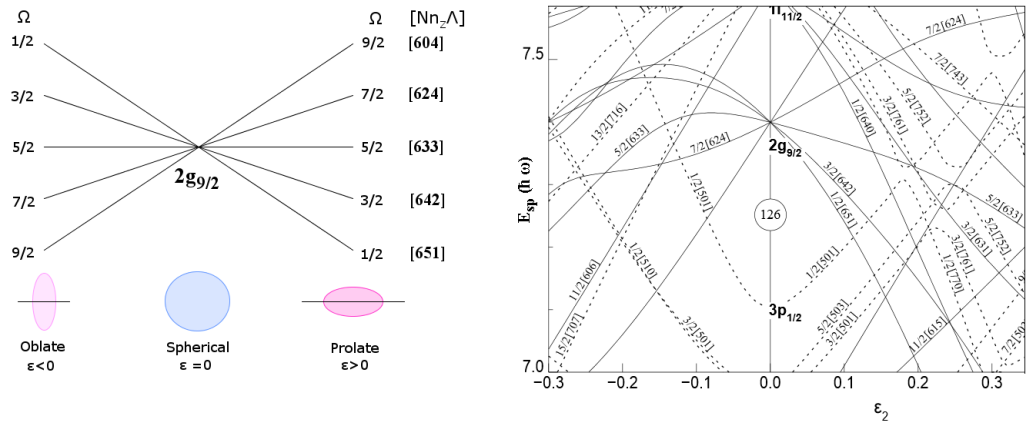

Figure 1.4: Left: Splitting of energy levels of different Ω value with deformation for the $2g_{9/2}$ state. Right: Example of the Nilsson diagram at N=126, figure adapted from [21].

Figure 1.4 on the left hand side shows the $2g_{9/2}$ state. This state is 10-fold degenerate in a spherical potential because all $2j+1$ projections of the angular

momentum lie at the same energy. The state splits into 5 doubly degenerate states ($\Omega = \pm 1/2, \pm 3/2, \pm 5/2, \pm 7/2, \pm 9/2$) in a deformed nucleus. On the right hand side, the Nilsson diagram for $N = 126$ shell is presented. For $\epsilon_2 = 0$ a gap is visible indicating a shell closure. The splitting of the state can be seen for $\epsilon_2 \neq 0$. Figures 1.5 and 1.6 show a Nilsson diagram for protons ($Z > 80$) and neutrons ($N > 120$) respectively. The single particle states in the figures are labeled with the previously described notation ($\Omega^{\pi}[N, n_z, \Lambda]$), the numbers in circles show the proton (neutron) numbers at which nuclei display effects of increased stability.
The Nilsson model (deformed shell model) reproduces well the single particle energies. However, it is not able to reproduce the total energy of the nucleus and consequently the binding energies and masses. To overcome this issue V. M. Strutinsky introduced a new method in 1967 [23] which is discussed in the following section.

1.1.3 Strutinsky model

The two previous sections introduced the LDM (1.1.1) and the Nilsson (1.1.2) model. It was mentioned that the first one is able to reproduce the total energy of the nucleus (macroscopic properties) but is insensitive to the single particle energies (microscopic properties). On the other hand, the Nilsson model reproduces well the single particle states of the nucleus but it is not able to reproduce the total energy of the nucleus as well as its masses. Starting from this point, Strutinsky decided to combine these two models in order to make a general model which would be able to reproduce both macroscopic and microscopic properties of the nucleus. For the Strutinsky model, the total energy of the nucleus is separated in two parts. The first part is derived form the LDM. The second part is derived from the shell model and is considered as small deviation from the uniform distribution of the LDM energy [23]. The total energy (E_{tot}) is then given by:

$$E_{tot} = E_{LD} + E_{sh}(neutrons) + E_{sh}(protons) \tag{1.7}$$

The shell correction energy E_{sh} is calculated as a difference between the sum over discrete energy levels of the shell model and a smeared energy function of the LDM in the same energy range. This gives the difference between the single particle energies (e) and the average behavior (e_ν) of the nucleus.
The discrete level energy density $g(e)$ is defined as the sum over all energy levels (ϵ_ν) of this difference:

$$g(e) = \sum_{\nu} \delta(e - e_\nu) \tag{1.8}$$

The smeared energy density $\tilde{g}(e)$ is given by:

$$\tilde{g}(e) = \frac{1}{\gamma\sqrt{\pi}} \sum_{\nu} f_{corr} \left(\frac{e - e_\nu}{\gamma} \right) \; exp \left(-\frac{(e - e_\nu)^2}{\gamma^2} \right) \tag{1.9}$$

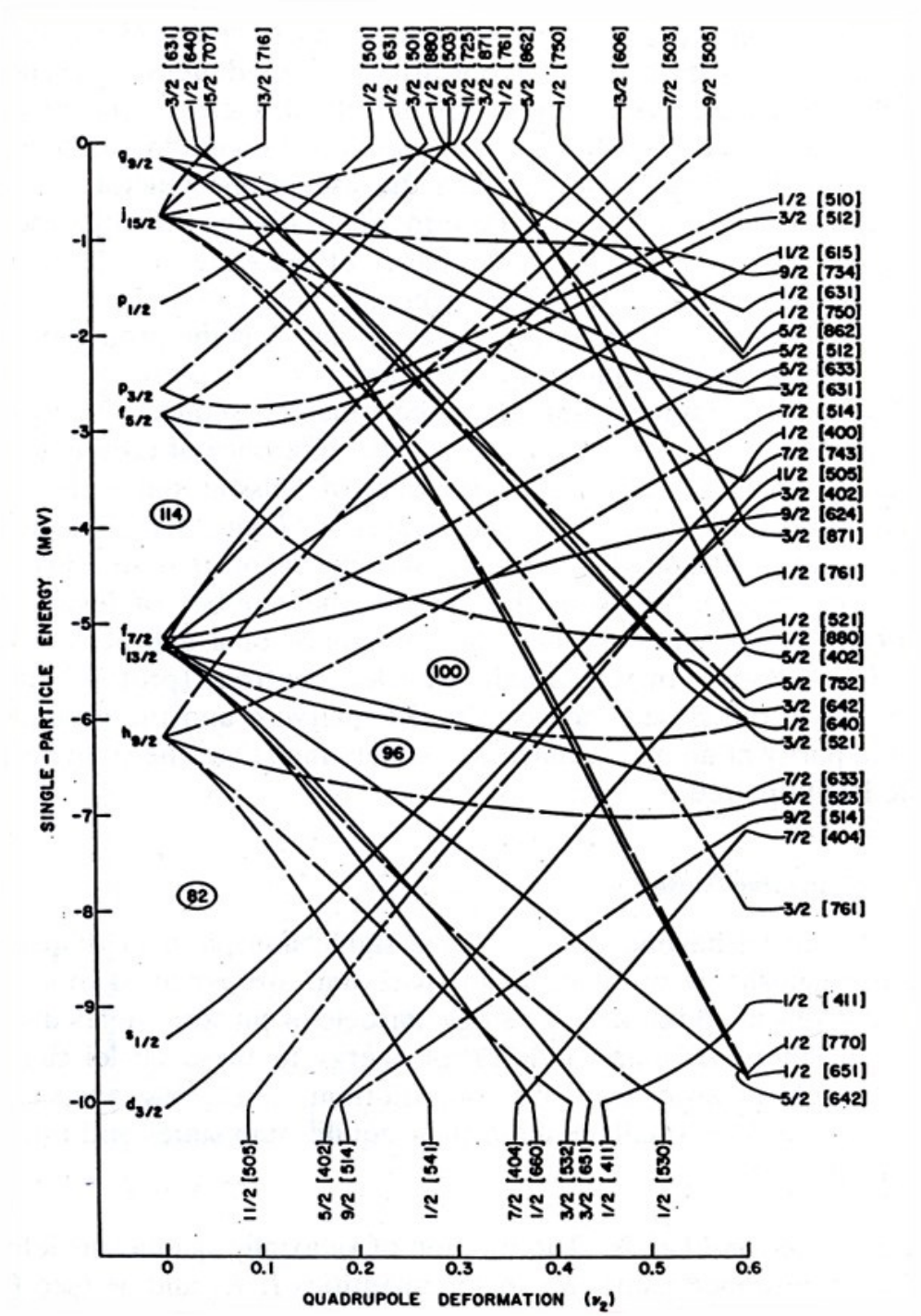

Figure 1.5: Nilsson diagram for protons with Z>80. Adapted from [22].

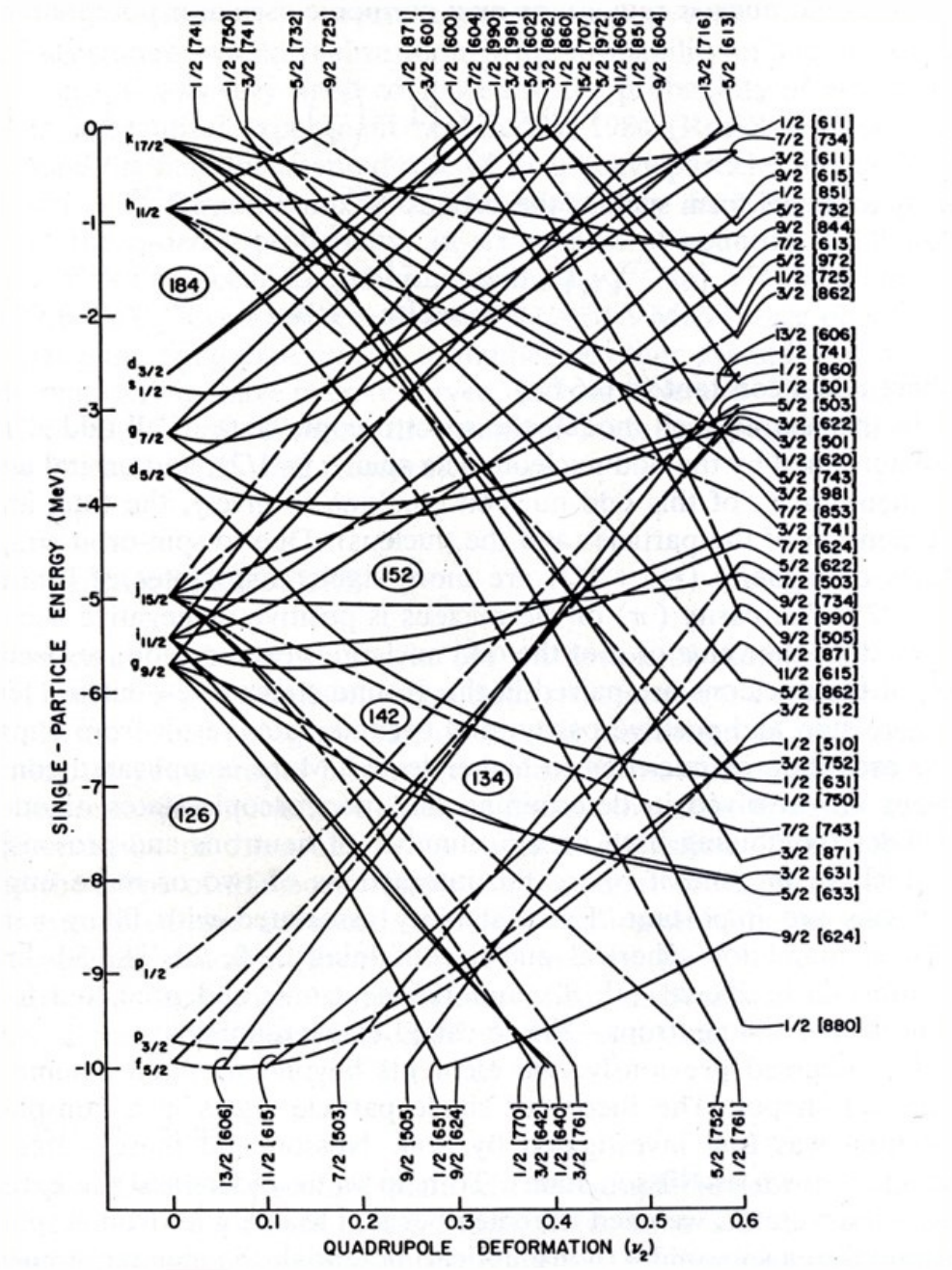

Figure 1.6: Nilsson diagram for neutrons with N>120. Adapted from [22].

here $\gamma = \hbar\omega_0$ is the shell spacing, ω_0 is the oscillator frequency for spherical harmonic oscillator, f_{corr} is a correction function which keeps the long range variations (bigger than γ) unchanged. Finally the shell correction energy E_{sh} is:

$$E_{sh} = 2\sum e_\nu - 2\int e\tilde{g}(e)de \tag{1.10}$$

If the shell correction energy is negative, the total energy of the nucleus is decreased and the binding energy is increased, giving a more stable nucleus. For example the shell correction energy for spherical nuclei is negative.
This model was able to predict the next shell closures after lead ($^{208}\mathrm{Pb}^{82}_{126}$). One of the main impacts of the model was the prediction that the next shell closure for protons does not necessarily have to be the same as for neutrons (at $N = 126$) [24]. In other words, the magic number in protons and neutrons can be different, which was not the case up to ^{208}Pb. As a result, Meldner proposed in 1967 that the next shell closure for protons would appear at 114 [25]. Later in 1969. Nilsson proposed 184 as the next neutron shell closure [26].
The Strutinsky model is used as a base for the microscopic-macroscopic (mic-mac) models.

1.1.4 Self-consistent mean-field models

The sections 1.1.2 to 1.1.3 presented the theoretical models based on the shell model. This section will breafly present another type of approach to describe the structure of nuclei: The mean-field models.
The essential difference between these two types of models is that the shell models consider the nucleons as independent particles moving in an external potential without interacting with each other whereas the non-relativistic mean-field models consider that the nucleons move in the nucleus with a kinetic energy and interact through the many-body force. The potential is then derived from the effective interaction between the nucleons with the help of Hartree-Fock method.
The starting point of the Hartree-Fock method is a N-body Hamiltonian:

$$H = \sum_{i=1}^{N} T(i) + \sum_{i<j=1}^{N} V^{(2)}(i,j) + \sum_{i<j<k=1}^{N} V^{(3)}(i,j,k) + ... \tag{1.11}$$

The first term presents the sum of the kinetic energies of the particles, the second term presents the two-body force, the third term presents the three-body force and so on. The quantum description of such a system requires the knowledge of the N-body wave function Ψ_{α_i}. The Hartree-Fock method introduces a simple approximation to this N-body problem to solve the Hamiltonian and obtain the total energy of the system. The method is assuming that fermions (non relativistic case) do not interact with each other except through an average self-consistent

mean-field. Consequently the complex N-body nuclear wave function can be written as a Slater determinant of single particle states. Or said differently the N-body wave function (Ψ_{α_i}) is an antisymmetrized product of single particle wave functions (ψ_{α_1}, ψ_{α_2}, ... ψ_{α_N}). The single particle wave functions are not known, and they are determined by demanding that they are the set of wave functions which minimize the total energy (E_{HF}). Minimization of the total energy gives the Hartree-Fock ground state. The minimization can be achieved using the Raylegh-Ritz variational principle over all possible variations of single particle components. The resulting wave equation then takes the following form:

$$\frac{\partial E_{HF}[\psi_{\alpha_i}]}{\partial \psi_{\alpha_k}(\overrightarrow{r})} = \left[-\frac{\hbar^2}{2m} \triangle \psi_{\alpha_k} + U_H \psi_{\alpha_k} + U_F \psi_{\alpha_k}\right](\overrightarrow{r}) - \epsilon_{\alpha_k} \psi_{\alpha_k}(\overrightarrow{r}) = 0 \qquad (1.12)$$

where ϵ_{α_k} is the total energy difference before and after removing the particle in state α_k. The potential in equation 1.12 consists of two parts: U_H the Hartree (local, direct) potential and U_F the Fock (non-local, exchange) potential. These potentials can be written as follows:

$$[U_H \psi_{\alpha_k}](\overrightarrow{r}) = \int d\overrightarrow{r\prime} \sum_{j=1}^{N} \psi^*_{\alpha_j}(\overrightarrow{r\prime}) v_{NN}(\overrightarrow{r}, \overrightarrow{r\prime}) \psi_{\alpha_j}(\overrightarrow{r\prime}) \psi_{\alpha_k}(\overrightarrow{r}) \qquad (1.13)$$

$$[U_F \psi_{\alpha_k}](\overrightarrow{r}) = -\int d\overrightarrow{r\prime} \sum_{j=1}^{N} \psi^*_{\alpha_j}(\overrightarrow{r\prime}) v_{NN}(\overrightarrow{r}, \overrightarrow{r\prime}) \psi_{\alpha_j}(\overrightarrow{r}) \psi_{\alpha_k}(\overrightarrow{r\prime}) \qquad (1.14)$$

where $v_{NN}(\overrightarrow{r}, \overrightarrow{r\prime})$ is the two body force acting between particles at $\overrightarrow{r}$ and $\overrightarrow{r\prime}$. The non-local (Fock) part of the equation is a consequence of the fact that two particles are non-distinguishable under exchange. A second look at equation 1.12 shows that the wave equation is a non-local equation and depends on the single particle wave functions, the same wave functions which are supposed to be determined with this equation. In order to solve this equation an iterative procedure is used. As input parameters, these equations require effective interactions. Different effective interactions are chosen depending on the properties which need to be treated. At first, the effective interactions were derived directly from the bare nucleon-nucleon interaction.

The Hartree-Fock (HF) calculation does not take into account pairing effects. A generalization of the Hartree-Fock method was done by introducing pairing effects into the Hamiltonian. This method is known as Hartree-Fock-Bogolyubov (HFB). This method become competitive to the mic-mac theories when the effective interactions used for it started to be adjusted to observables of finite nuclei [28]. The zero-range Skyrme and finite range Gogny forces are mostly used as input parameters.

All of these models can provide estimation for the next shell closures for both

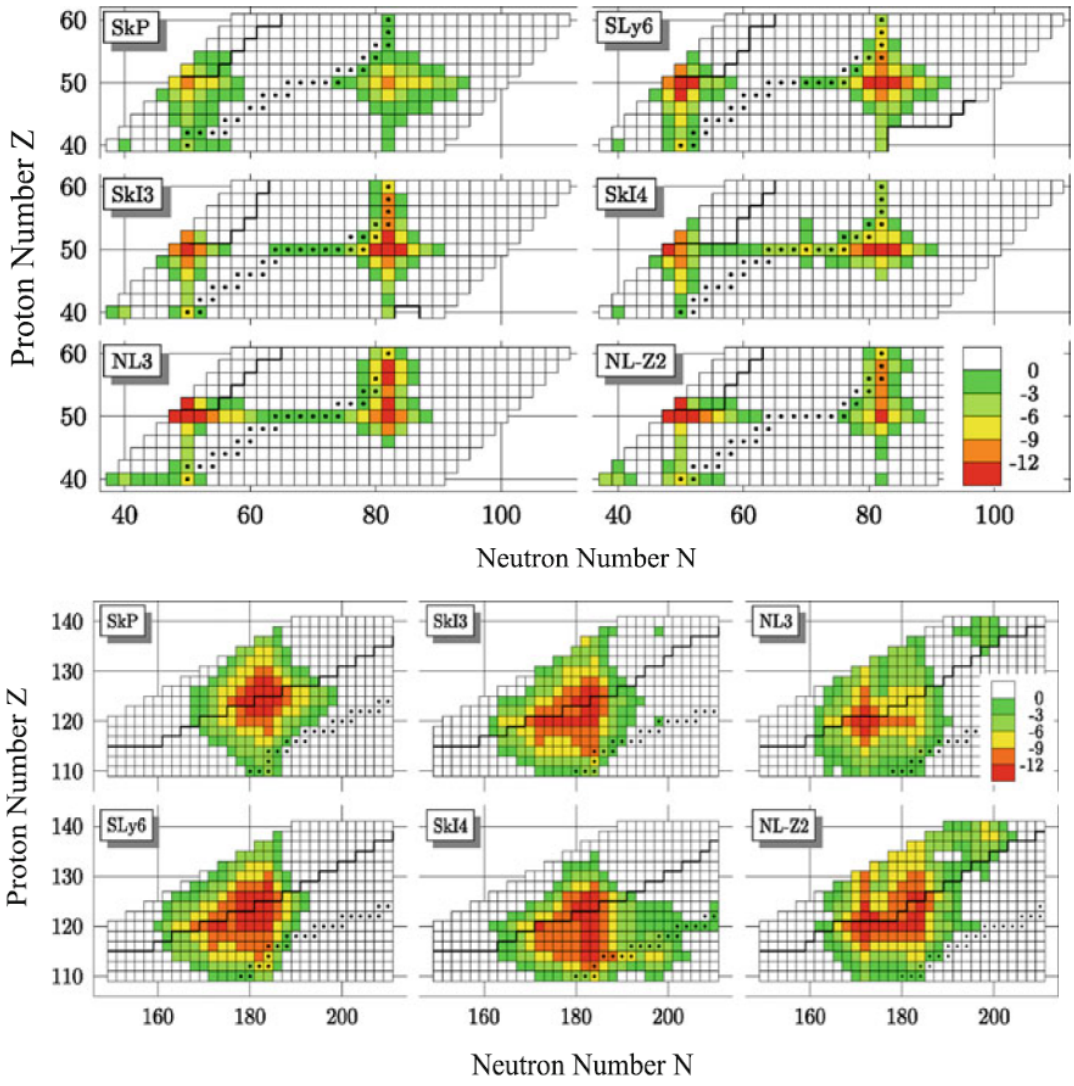

Figure 1.7: The behavior of shell stabilization in the tin region (SHE) on top (bottom) calculated with different parametrization of SHF and RMF. Figure adopted from [27].

protons and neutrons. A trend can be observed in the calculations, showing that the non-relativistic mean-field models favor $Z = 124$, 126 and $N = 184$ for the next shell closures, while relativistic models favor $Z = 120$ and $N = 172$ ([24] and references therein).
An interesting prediction for the next shell closure based on Self-Consistent Mean-Field (SCMF) models was proposed in 2001 by Bender [27]. Figure 1.7 shows calculations for the shell closures in the region of Sn (top) and super heavy region (bottom). The calculations were performed using several parametrizations of the Skyrme Hartree-Fock (SHF) and Relativistic Mean-Filed (RMF) models. The figure 1.7 on the top shows that the shell stabilization closely follows the magic numbers around Sn ($Z = 50$). However bottom figure 1.7 shows an island of shell stabilization in a wide region of SHE. The results are comparable between the two models and all parameterizations [27].

1.2 Nuclear rotation

As it was discussed in the previous section 1.1.2, most of the nuclei have a deformed rather than spherical shape. These deformations bring extra stability to the nuclei and existence of heavy elements (outside of the island of spherical stability) which would not be observed otherwise. For example, the nuclei in the region of Db (Z=105, studied in this work) are quadrupole deformed. A deformation of a nucleus introduces a new degree of freedom in the form of rotation. The rotation of a nucleus is possible only if the wave function of a system rotated by a small angle is different from the wave function of a non-rotated system. This explains why the rotation is present in deformed and not in spherical nuclei. The rotation of the nucleus is expressed in a form of collective excitation which is detectable.
The total angular momentum (I) of a nucleus rotating about an axis is expressed as the sum of the collective rotation of the nuclear core (R) and the rotation of the individual nucleons ($J = \sum_{i=1}^{A} j_i$):

$$I = R + J \tag{1.15}$$

In figure 1.8 it can be seen that the projection of the total angular momentum (I) on the symmetry axis gives quantum number K. It is clear that the K quantum number is not influenced by the variations in the collective rotation (R) of the nucleus. Consequently a rotational band is built from a combination of rotational states with the same quantum number K. This quantum number is further used to characterize the rotational band.
The projection (K) of the total angular momentum (I) on the symmetry axis is zero when the sum of the angular momentum of valence nucleons (J) is equal to zero (figure 1.8). Consequently the ground state rotational band of an even mass

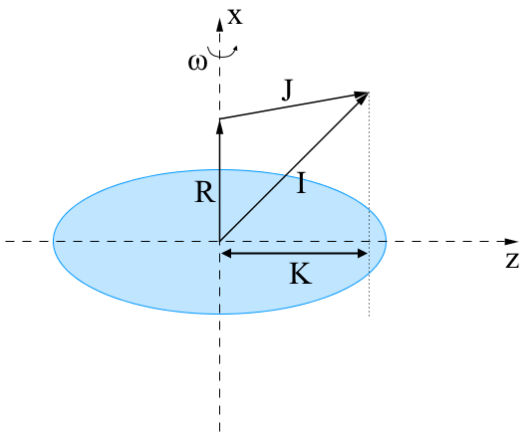

Figure 1.8: Schematic representation of a rotating nucleus, showing the collective angular momentum R, the angular momentum of valence nucleons J and the total angular momentum I with the projection K on the symmetry axis (z).

nucleus is built on top of $K = 0$.
Figure 1.9 shows the rotational bands built on top of $K = 0$, ground state (on the left hand side) and $K = 3$ and 8 (on the right hand side) for the even mass nucleus of ^{254}No. It can be noted that the ground state rotational band built on $K = 0$ consists of states with even spins connected by electric quadrupole (E2) transitions. On the other hand the rotational band built on $K = 3$ shows states with integer spins bigger than three, connected by both electric quadrupole (E2) and magnetic dipole (M1) transitions. Electromagnetic transitions are discussed in section 1.3.3.
The lack of odd spin states for the ground state rotational band is due to the underlying symmetry. The eigenvalues of the rotational Hamiltonian show that the wave functions have to obey the relation $(-1)^I|I >= R(180^0)|I >$. This relation is fulfilled for even but not for odd spin states. For $K > 0$ the symmetry is broken and all states are possible.
In the case of a deformed nucleus the rotational energy ($E(I)$) can be expressed as:

$$E(I,K) = \frac{\hbar^2}{2\Im}\left[I(I+1) - K^2\right] \tag{1.16}$$

where $\Im$ is the moment of inertia.
It should be emphasized that the nuclear moment of inertia is not exactly the same as the moment of inertia of the rigid body. The moment of inertia of the deformed nucleus varies with the spin and can be considered partly rigid body and partly fluid body with a rigid core and a "fluid" of valence nucleons. The picture is additionally complicated by pairing effects. Moment of inertia of the deformed

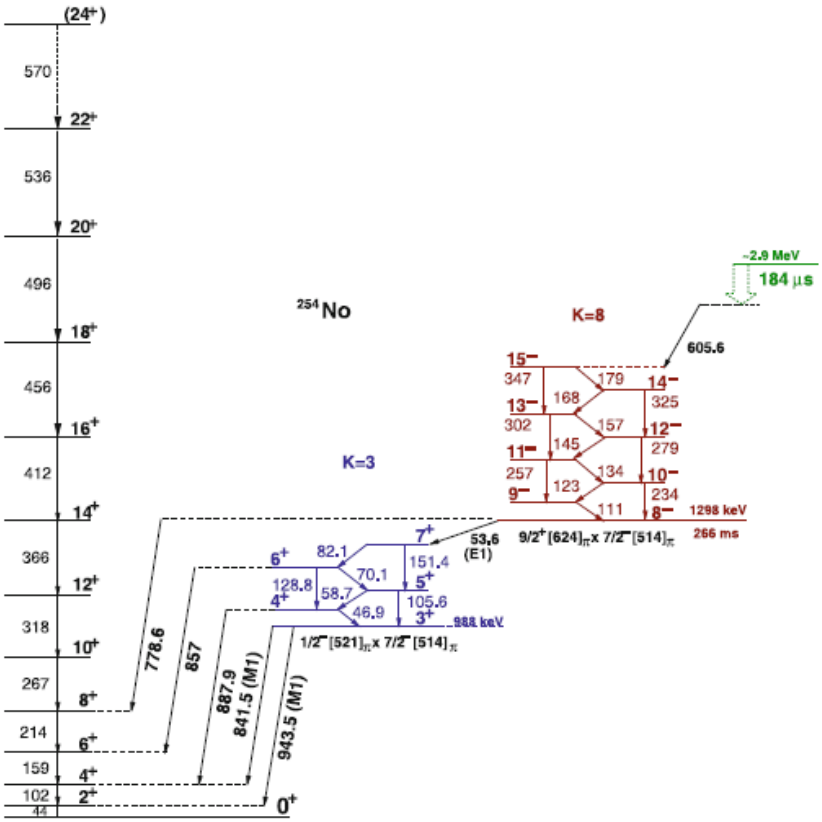

Figure 1.9: Rotational bands of ^{254}No nucleus are shown. The ground state rotation band built on $K = 0$ is shown on the left, the rotational band built on $K = 3$ and $K = 8$ are shown on the right. Figure adopted from [11].

nucleus can be calculated using for example cranked relativistic Hartree-Fock-Bogoliubov theory [28].

1.3 Decay modes

Previous sections give an overview of the theoretical models used to describe the properties and the structure of nuclei. Experimentally the study of these nuclei is achieved by analyzing their radioactive decays. A superheavy nucleus can decay by α emission, fission, electromagnetic and β decay (figure 1.10). Decay modes used to probe the structure of ^{257,258}Db and their daughters are described in the following section.

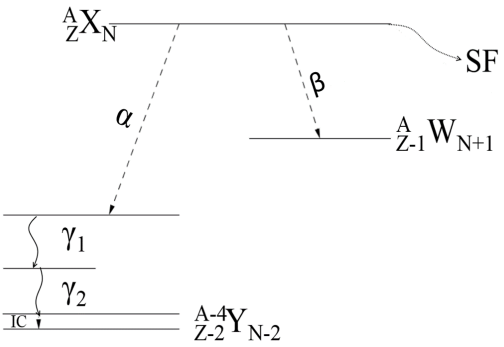

Figure 1.10: Different decay modes of a SHE ($^{A}_{Z}X_{N}$) and γ-ray and internal conversion decay of the daughter nuclei ($^{A-4}_{Z-2}Y_{N-2}$). SF corresponds to spontaneous fission.

1.3.1 Alpha decay

Alpha decay is characterized by the emission of an α particle, helium ($^{4}He^{2+}$) nuclei, from a mother nucleus X (mass m_X) with discrete energy E_α and can be presented in the following form:

$$^{A}_{Z}X_{N} \rightarrow ^{A-4}_{Z-2}Y_{N-2} + \alpha \tag{1.17}$$

where Y is the daughter nucleus with mass m_Y. The energy conservation during the α emission can be written as follows:

$$Q_\alpha = (m_X - m_Y - m_\alpha)c^2 = T_Y + T_\alpha \tag{1.18}$$

where T_Y and T_α are the kinetic energies of the decay fragments (daughter nucleus and the α particle). The Q-values (Q_α) correspond to the sum of the kinetic

energies of the decay fragments. The emission of an α particle occurs spontaneously for $Q_\alpha > 0$. Due to the conservation of the linear momentum, the kinetic energy of the α particle can be expressed as a function of the Q_α value in the following way:

$$T_\alpha = \frac{Q_\alpha}{1 + \frac{m_\alpha}{m_Y}} \tag{1.19}$$

On the quantum mechanical point of view the α particle is preformed in the nucleus and tunnels through the Coulomb barrier with a certain probability λ. This probability follows the Geiger-Nuttall law:

$$log(\lambda) = A + \frac{B(Z)}{\sqrt{T_\alpha}} \tag{1.20}$$

where A is a constant and B depends on the proton number (Z). Determining the probability for the α decay to occur gives an insight in the structure of the mother nucleus since the half-life ($T_{1/2}$) is dependent on the decay probability (λ) in the following way:

$$T_{1/2} = \frac{ln(2)}{\lambda} \tag{1.21}$$

The difference in the angular momentum between the mother and the daughter nucleus is restrained in the following way:

$$|j_i - j_f| \leq l_\alpha \leq |j_i + j_f| \tag{1.22}$$

where j_i and j_f are the total angular momenta of the initial and final state in the mother and daughter nucleus respectively, and l_α is the angular momentum carried out by the α particle.
The α decay can change the parity π defined as:

$$\pi = (-1)^l \tag{1.23}$$

Consequently the parity is conserved for even values of the angular momentum l, and changed for odd values of l.
The α decay of the mother nucleus can populate a number of different states in the daughter nucleus, allowing a structure study of its single particle states. If the angular momentum between the initial state of the mother nucleus differs form the final state of the daughter nucleus the transition may be hindered increasing the half-life of the decay. The hindrance factor can than be expressed as followed:

$$HF = \frac{T_\alpha^{exp}}{T_\alpha^{theo}} = \frac{T_{1/2}/(b_\alpha i_\alpha)}{T_\alpha^{theo}} \tag{1.24}$$

where $T_{1/2}$ and b_α are the half-life and the branching ratio of the mother nucleus for a specific state and i_α is the intensity of the selected α line compared to all other α transitions. These values are obtained experimentally. T_α^{theo} is the theoretically calculated half-life of the mother nucleus. Several methods, such as the method proposed by Rasmussen [29], or the semi-empirical formula proposed by Poenaru [30] with the parameter modification proposed by Rurarz [31], can be used to calculate the theoretical value of the half-life.
Unambiguous identification of an isotope is possible due to the fact that an α decay can be correlated to a specific state of a particular isotope. If the α decay chain finishes in a known isotope it is then possible to go backward along the chain and identify the originally produced isotope. This method was used in the search for new elements.

1.3.2 Electron capture

Electron Capture (EC) is a type of a β decay and it occurs in proton-rich nuclei. It is similar to the β^+ decay with a difference that a positron (e^+) is not emitted but rather an electron (e^-), from the inner shells of the atomic nucleus, is captured by the nucleus leaving the neutrino (ν) to be the only emitted particle in the process. Due to the nature of this process the necessary energy can be smaller than the one required for the creation of the electron-positron pair ($2 \cdot 511$ keV), as it is the case for β^+ decay. Consequently, a nucleus which can decay by a β^+ emission can also decay by EC, but not vice-versa.
The EC can be presented in the following form (figure 1.10):

$$ {}_ZX_N^A + e^- -> {}_{Z-1}W_{N+1}^A + \nu \tag{1.25}$$

were X is the mother and W is the daughter nucleus, e^- is the electron form the electron shell of the mother nucleus and ν is the neutrino which is emitted in the process. The energy conservation during the EC process can be written as follows:

$$ Q_\beta = m_X c^2 - m_W c^2 - Bn \tag{1.26}$$

where Bn is the binding energy of the captured n-shell electron. Due to the fact that the positron is not emitted in the process the neutrino has an exact energy depending on the difference in the energies of the mother and daughter nucleus. This characteristic is different compared to the β^+ decay where the energy of the positron as well as the neutrino has continuous values between zero and the energy difference between mother and daughter nuclei.
Capturing an electron form the atomic shell of the nucleus results in a vacancy in the inner shell of the atom, as a result the EC decay is followed by an emission of X-ray and/or Auger electrons due to deexcitation in the electron shell of the

daughter nucleus.
Assuming a zero rest mass of the neutrino and that the capture occurs on the K-shell electron, because the electron density at the nucleus level is the biggest for these electrons, the EC constant (λ_{EC}) can be written as:

$$\lambda_{EC} = \frac{E_{\nu_e}^2}{\pi^2 c^3 \hbar^4} g^2 |M'_{fi}|^2 \left(\frac{Z m_e c^2}{4\pi\epsilon\hbar^2} \right)^3 \tag{1.27}$$

where $|M'_{fi}|$ is the nuclear matrix element and Z is the proton number of the mother nucleus. It can be further observed that the EC is favored for high Z nuclei.

1.3.3 Electromagnetic decay

An electromagnetic decay is an internal process in which the initial and final number of protons and neutrons stays the same. It is a consequence of a de-excitation of a nucleus where the released energy is either emitted as a γ-ray photon or is transferred to an atomic electron (internal conversion), see figure 1.11. These two transitions are competing processes which give useful information on the nuclear structure of the observed nucleus.

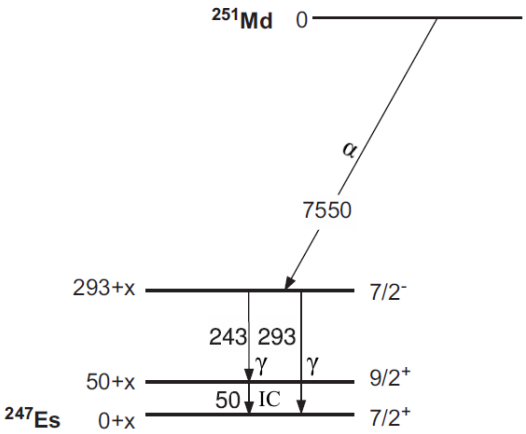

Figure 1.11: Deexcitation of the excited states in the ^{247}Es isotope. Both γ-ray and conversion electron emission (IC) are visible. Figure adopted from [32].

Gamma decay

The de-excitation of a nucleus from an excited state to the ground state via emission of γ-rays can be achieved in one or several steps. The energy (E_γ) of the

emitted γ-ray corresponds to the difference in energy between the initial (E_i) and final (E_f) state inside of the nucleus ($E_\gamma = E_i - E_f$). The γ-ray particle can remove an angular momentum as well as change the parity between the two levels. The angular momentum (l) and parity (π) are constrained by selection rules. The angular momentum selection rule falls in:

$$|j_i - j_f| \leq l \leq j_i + j_f \tag{1.28}$$

where j_i and j_f are the total angular momentum of the initial and final state in the nucleus and l is the angular momentum carried out by the emitted γ photon. Another selection rule is dictated by the parity of the transition. Generally there is two types of electromagnetic transitions, electric for which the sum $j_i + j_f + l_\gamma$ takes an even value and magnetic for which the sum takes an odd value. Depending on the difference in the angular momentum (Δl) the electromagnetic transitions can have different multipoles (see table 1.1): dipole, quadrupole, octupole, etc... The probability λ for a γ-ray transition to occur was modeled on the basis of single particle states by Weisskopf:

$$\lambda_{electric} = 10^{21} \frac{4.4(l+1)}{l[(2l+1)!!]^2} \left(\frac{3}{l+3}\right)^2 \left(\frac{E_\gamma}{197}\right)^{2l+1} R^{2l} s^{-1} \tag{1.29}$$

$$\lambda_{magnetic} = 10^{21} \frac{1.9(l+1)}{l[(2l+1)!!]} \left(\frac{3}{l+3}\right)^2 \left(\frac{E_\gamma}{197}\right)^{2l+1} R^{2l-2} s^{-1} \tag{1.30}$$

where l is the angular momentum taken by the photon, E_γ is the energy of the γ-ray and R is the nuclear radius in femtometers (fm).

Name	Dipole	Quadrupole	Octupole	Hexadecapole
No parity change	M1	E2	M3	E4
Parity change	E1	M2	E3	M4
Selection rule, Δj	0,±1	0,±1, ±2	0, ±1, ±2, ±3	0, ±1, ±2, ±3, ±4

Table 1.1: Electromagnetic transition selection rules for the lowest multipoles.

Internal conversion

The internal conversion is an electromagnetic process which competes with γ-ray emission. In the process the de-excitation energy of the nucleus is transferred to one of the electrons in the electron shell of the atom. The electron is then ejected from the atom if its binding energy is smaller than the transferred energy. Electrons from inner atomic shells like K, L, etc... are more likely affected by internal conversion as their wave function can overlap with the one from the nucleus, especially in the

case of heavy elements.
The energy of the emitted electron (E_e) can be expressed as follows:

$$E_e = \Delta E - E_B \tag{1.31}$$

where ΔE is the energy corresponding to the difference between the two levels in the nucleus and E_B is the binding energy of the electron. The conversion electrons are accompanied by a characteristic X-rays as well as Auger and Coster-Krönig electrons. These photons are emitted since the electrons from the higher shells of the atom deexcite to the deep vacancy left by the ejected electron through different patterns [33]. If the energy released due to the deexcitation of the atom is high enough to eject an electron from one of the outer shells of the atom the IC is followed by emission of Auger or Coster-Krönig electrons. The difference between the two is that in the case of Coster-Krönig electrons one of the two remaining vacancies in the electron shells is positioned in the same major shell as the original vacancy which does not have to be the case for the Auger electrons [34].
The probability of the conversion of a transition is given by the Internal Conversion Coefficient (ICC or α). ICC is the ratio between the probability to emit an electron and the probability to emit a γ-ray for a given transition:

$$\alpha = \frac{\lambda_e}{\lambda_\gamma} \tag{1.32}$$

ICC can also be presented as the sum of the partial coefficients of individual atomic shells:

$$\alpha = \alpha_K + \alpha_L + \alpha_M + ... \tag{1.33}$$

The total probability of an electromagnetic transition (λ) is expressed as a function of the probability for γ decay and for internal conversion:

$$\lambda = \lambda_\gamma(1 + \alpha) \tag{1.34}$$

The ICC for electric transitions, in a non-relativistic case, is expressed as:

$$\alpha(EL) \simeq \frac{Z^3}{n^3}\left(\frac{L}{L+1}\right)\left(\frac{e^2}{4\pi\epsilon_0\hbar c}\right)^4\left(\frac{2m_ec^2}{E}\right)^{L+5/2} \tag{1.35}$$

and for magnetic transition:

$$\alpha(ML) \simeq \frac{Z^3}{n^3}\left(\frac{e^2}{4\pi\epsilon_0\hbar c}\right)^4\left(\frac{2m_ec^2}{E}\right)^{L+3/2} \tag{1.36}$$

The dependance on the Z^3 (proton number) and $1/E_\gamma$ (energy of the transition) indicates that the internal conversion dominates for heavier elements and for lower transition energies compared to lighter nuclei. On the other hand, the ICC is inversely proportional to the principal quantum number n of the bound electron wave function, indicating that the electrons from higher electron shells participate less to the internal conversion process. Even though these approximations give a reasonable description of the physical properties of the ICC, it is not possible to treat the electrons non-relativistically. The typical transition energy is between 0.5 and 1 MeV meaning that the approximation $E_e << m_e c^2$ is not valid and more rigorous models (such as Hartree-Fock) have to be used for the calculation of theoretical ICC.

1.4 Nuclear isomers

Some nuclei present strongly inhibited electromagnetic transitions, which were discussed in the previous section 1.3.3. The consequence of this inhibition is an increased half life. Nuclei in these long lived excited (metastable) states are called isomers. The excitation energy of such a state can be up to several MeV. There is no strict definition of the minimum half life of an isomeric state, except that it has to be longer than the one of a typical non-isomeric state. Nuclear isomers (figure 1.12) can be separated in three groups [35]: Shape isomers, Spin traps and K-traps.

Shape isomers, figure 1.12 on the left, occur when there is a secondary energy minimum at large elongations of the nucleus (the primary energy minimum corresponds to the ground state). These isomers can decay by γ-ray emission or fission (if the fission barrier is low enough).

Spin traps, middle figure 1.12, are a consequence of the inability to meet the spin selection rules (conservation of the angular momentum). The decay requires a large change in spin so an emission of high multipolarity (λ) radiation. The low probability for such a transition (see equations 1.29 and 1.30) increases the half-life of such a state producing spin trap isomers.

K-traps, figure 1.12 on the right, are a type of spin trap isomers. Unlike spin traps, their existence does not depend only on the magnitude of the nuclear spin vector, as the spin traps, but also on its orientation. This type of isomers arises only for deformed nuclei for which just the quantum number K (projection of the total angular momentum on the symmetry axis (figure 1.8)) and parity (π) are preserved.

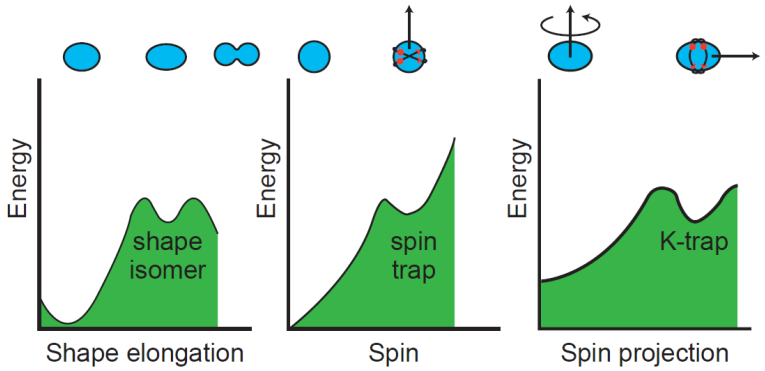

Figure 1.12: Excitation energy as a function of various nuclear variables (shape elongation (left), spin (middle), spin projection (right)). The secondary energy minima are responsible for the different kinds of isomers: shape isomers (left), spin traps (middle) and K-traps (right). In each case the relevant nuclear shapes are illustrated; where appropriate, angular momentum vectors are shown as arrows. For both the spin trap and the K-trap, the angular momentum comes from a small number of orbiting nucleons (two are illustrated in red in each case). Figure adopted from [35].

The strict selection rule requires that the multipolarity of the decay radiation (λ) is at least as large as the change in the K-value, $\lambda \geq \Delta K$. However, due to symmetry breaking processes, these forbidden transitions are more hindered than forbidden [35]. The degree of forbiddenness of a given transition is ruled by the decay probability [36]:

$$\nu = \Delta K - \lambda \tag{1.37}$$

Empirically each degree of K-forbiddenness increases the lifetime of a state for a factor of 20 [36]. The hindrance factor (F_w) is defined as:

$$F_w = \frac{T^{\gamma}_{1/2}(exp)}{T^{\gamma}_{1/2}(theo)} \tag{1.38}$$

where $T^{\gamma}_{1/2}(exp)$ and $T^{\gamma}_{1/2}(theo)$ are experimentally and theoretically (calculated by the Weisskopf estimation method (section 1.3.3)) determined half-lives for γ-ray emission from the observed state.

Chapter 2

Experimental techniques for production and detection of SHE

Chapter 1 describes the physics background of the heavy and superheavy elements. However in order to study these elements it is necessary to artificially produce them. Production of such elements for experimental studies faces a number of technical challenges, such as small production cross sections and short half-lives. Development of the production facilities and multi-detector systems combined with techniques such as recoil tagging or generic correlations allow for full investigation in the region of heavy and superheavy elements.
This chapter is, in the first part, dedicated to the description of the production procedure (fusion-evaporation reaction 2.1) and the different facilities 2.2 used for the synthesis of the studied elements. Additionally it gives an overview of a new facility (S^3) which is currently under construction 2.2.3. The second part of the chapter describes the techniques (2.3) and the multi-detector systems (2.4) used for the identification and study of the produced elements.

2.1 Fusion-evaporation reaction

The standard method used for the production of heavy and superheavy elements is fusion-evaporation reaction.
As can be seen in figure 2.1 several channels are in competition. When the energy of the interacting nuclei (projectile and target) is high enough to overcome the Coulomb barrier and low enough to not pass the fission barrier (causing quasi fission 2.1), a Compound Nucleus (CN) in an excited state is formed. This CN can either do a prompt fission (figure 2.1) or go to the evaporation channel. If the CN went to the evaporation channel it can further deexcite by emitting light particles (α particles, protons, neutrons, etc...). This process is called the evaporation phase

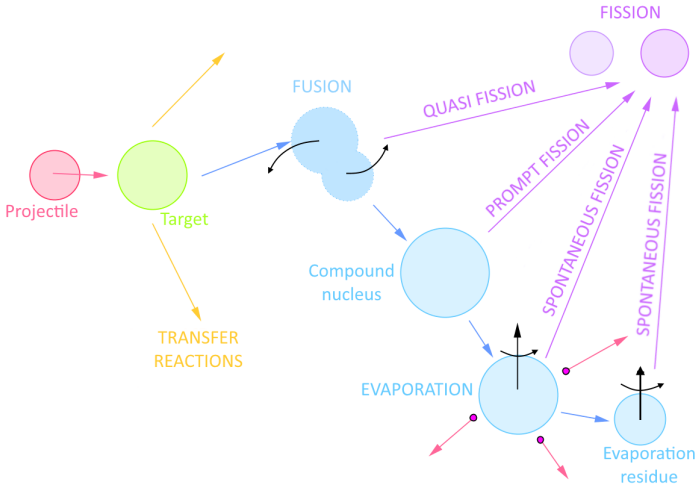

Figure 2.1: Schematic representation of the projectile-target interaction leading to a fusion-evaporation reaction and creation of the evaporation residue. Channels competitive to fusion-evaporation reaction are indicated.

and it is in constant competition with spontaneous fission (figure 2.1). If the CN survives the evaporation phase without fissioning, an Evaporation Residue (ER) is formed. This is the last step of the fusion-evaporation reaction. This ER further decays by α, β, γ and X-ray emission or by fission. The decay channels of the ER are the ones studied by delayed and prompt spectroscopy. In this work, the α delayed spectroscopy was used to study the ER produced in the two performed experiments.
The amount of excitation energy of the CN at Coulomb barrier depends on the projectile and target masses [37]:

$$E_x = B_C - Q \tag{2.1}$$

where $Q = M_{CN} - (M_P + M_T)$, M_P, M_T and M_{CN} are the masses of the projectile, target and CN respectively, B_C is the energy of the Coulomb barrier.

The production cross section for the fusion-evaporation reaction is calculated as:

$$\sigma_{er} = \sigma_c \, P_{CN} \, W_{sur} \tag{2.2}$$

where

- $\sigma_c \, P_{CN}$ present the probability for capture and formation of the CN

- W_{sur} is the survival probability of the CN to create the ER (figure 2.1). It is calculated on the basis of statistical models [38, 39].

The fusion probability ($\sigma_c\, P_{CN}$) is divided in two parts which are calculated separately. The first part calculates the overcoming of the Coulomb barrier for the interacting nuclei to fuse using either a quantum coupled channels method or a semi-classical approximation [38]. The formation probability (P_{CN}) of the fusion system to form a CN is the most complicated to calculate and several models were developed for this purpose. These models can be divided in three categories: Di-Nuclear System (DNS) [40, 41], Fusion by diffusion [42, 43] and Phenomenological model [39, 44].
DNS model describes fusion as a transfer of nucleon or a cluster of nucleons from the lighter system to the heavier one until the lighter system disappears and a CN is formed. On the other hand, the Fusion by diffusion models use one-dimensional Brownian motion of a particle suspended in a viscous fluid at temperature in the presence of a repulsive parabolic potential for describing the formation probability. The phenomenological model calculates the probability within the two-center shell model [39].

From the experimental point of view two types of fusion-evaporation reactions can be distinguished: cold and hot fusion-evaporation reaction.
Cold fusion-evaporation reactions use lead (Pb) or bismuth (Bi) targets in combination with medium-mass heavy ion projectile beams (^{48}Ca, ^{50}Ti, ^{54}Cr, etc). The interaction produces a CN with low amount of excitation energy (cold system), which results in emission of one to two neutrons. Due to the low excitation of the CN, its survival probability is increased. However the cross sections decreases dramatically for elements up to $Z = 110$ with the increase of the projectile mass (figure 2.2 on the left).
The cold fusion-evaporation reactions were used to produce elements up to $Z = 113$ [45], and are used for the production of ^{257,258}Db in this work.
The nuclei from $Z = 112$ to $Z = 118$ [46] were produced in hot fusion evaporation reactions. These reactions are based on more asymmetric systems (bombarding actinide targets with calcium (^{48}Ca) beam) producing a CN with higher excitation energies and causing more neutron evaporation [47]. Attempts of using projectiles like titanium (^{50}Ti) or chromium (^{54}Cr) were made for the production of even heavier nuclei. However these reactions were unsuccessful. Figure 2.2 on the right, shows the evolution of the hot fusion-evaporation cross section in dependance of the CN neutron number for different projectiles and actinide target combinations. It can be noted that the cross section decreases with the increase of neutron and proton number for light projectiles, on the other hand an increase of the cross section is visible for calcium beam at masses beyond $Z = 110$.

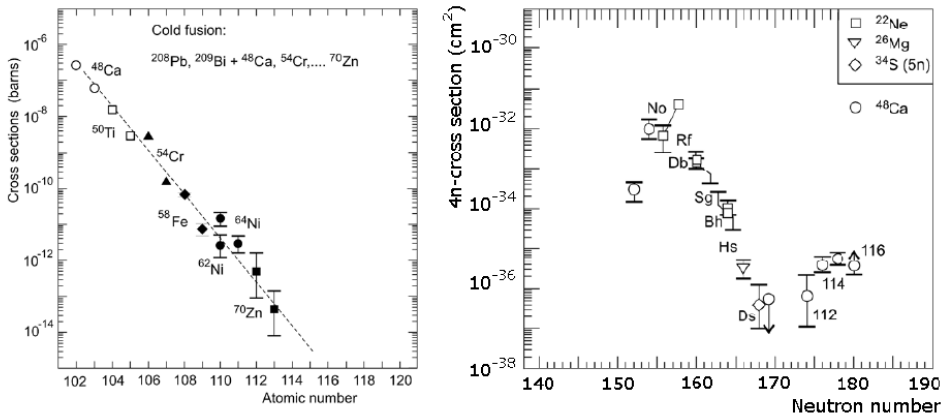

Figure 2.2: Left: Maximal experimental cross sections of the 1n evaporation channel in the cold fusion reactions of ^{208}Pb and ^{209}Bi target nuclei with different projectiles (indicated in figure) as a function of CN atomic number (dashed line is drawn to guide the eye). Right: Experimental cross sections at the maximum of 4n-evaporation channels in hot fusion reactions leading to the formation of isotopes of elements 102-110 at different neutron numbers of the CN. Additionally experimental cross sections for isotopes 112-116 produced in reactions actinide + calcium are shown. Figures adopted from [37].

2.2 Spectrometers and separators

The description of the two facilities used for the production of the two studied isotopes of ^{257}Db 2.2.1 and ^{258}Db 2.2.2 are described in this section. Additionally a description of the new facility S^3, which is currently under construction at GANIL, is given in 2.2.3.

2.2.1 The LISE spectrometer

LISE (Ligne d'Ions Super Epluchés) is a doubly achromatic spectrometer at the GANIL-SPIRAL1 facility, used for the study of exotic nuclei at 0^o [48]. It can operate in several modes: standard (LISE3), LISE-2K and FULIS (FUsion at LISe) [49].
In this section only the FULIS mode will be discussed. This mode was used for the performed experiment on ^{257}Db (chapter 4).
The primary beam is guided through the LISE spectrometer up to the target position b (figure 2.3) at the entrance of the Wien filter [51]. This part of the LISE spectrometer consists of the reaction chamber, the Wien filter (used for separation) and the detection chamber positioned at the focal plane of the LISE beam line in D6 room (figure 2.4).

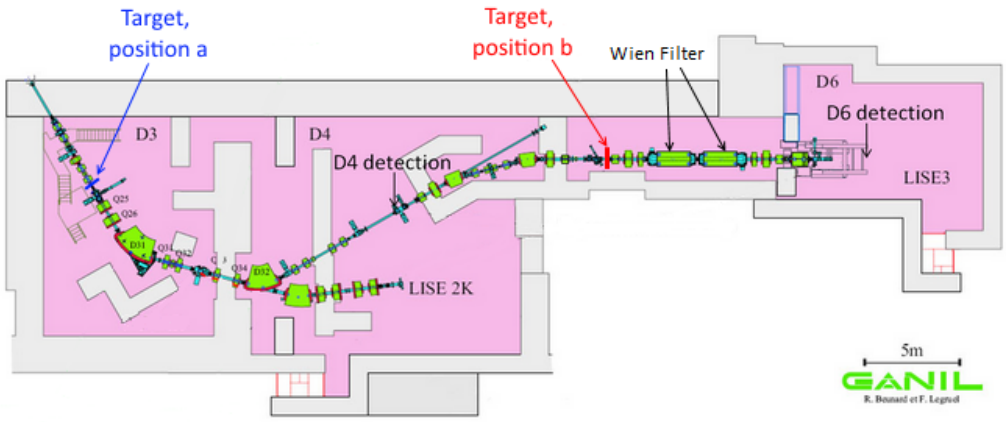

Figure 2.3: The LISE spectrometer, with the indication of Wien filter and possible target positions.

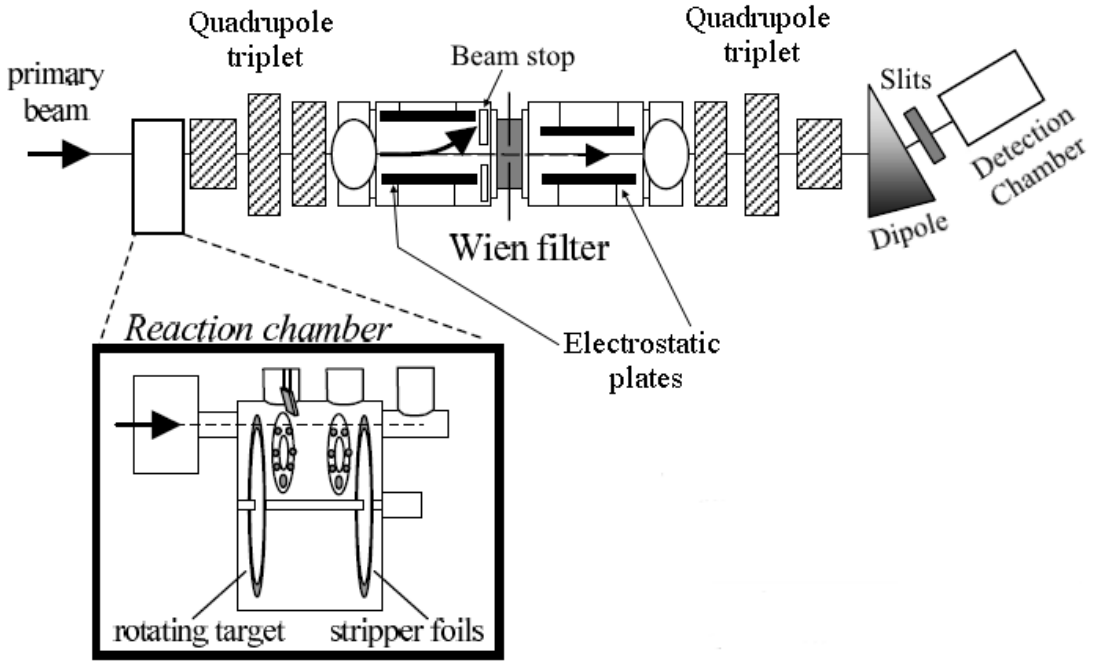

Figure 2.4: Schematic drawing of the FULIS set up at LISE, including from left to right: the reaction chamber with the rotating wheels, the Wien filter, the last dipole, the moving slits and the detection chamber. Figure adopted from [50].

The reaction chamber, in vacuum, contains two rotating wheels of 743 mm external diameter corresponding to 670 mm at the beam impact point. The rotation of the wheels can go up to 2000 rpm, which allows targets with low melting temperatures as bismuth (Bi) or lead (Pb) to sustain high intensity primary beams. The wheels are separated in eighteen segments. The first wheel is used as the target carrier, while the second wheel supports carbon stripper foils for re-equilibration of the charge state of the evaporation residues. The target wheel rotation is synchronized with the beam time structure.
The Wien filter is a 12 m long device used, in this case, to separate the evaporation residues from the transfer products. It is made out of two quadrupole triplets and two large gap dipole magnets inside of which two sets of electrostatic plates designed for high voltage (up to ±250 kV) are placed (figure 2.4). The electrostatic plates produce a vertical electric field ($\overrightarrow{E}$), while the magnets produce a magnetic field ($\overrightarrow{B}$) perpendicular to the electric one. The combination of the electric and magnetic fields selects a specific velocity for which the electric force compensates the magnetic force:

$$\overrightarrow{F_{tot}} = q\ \overrightarrow{E}\ + q\ (\overrightarrow{v}\ \times\ \overrightarrow{B}) = 0 \tag{2.3}$$

Or differently said, the nuclei with velocity $v = E/B \pm \Delta v$. Final adjustment of the velocity range Δv is done by opening and closing the vertical slits positioned between the last dipole magnet and the detection chamber (figure 2.4). Additional background suppression can be achieved through Bρ selection using the last dipole magnet positioned at the end of the Wien filter [50].
LISE is characterized with an angular acceptance of ±20 mrad and a velocity acceptance of ±5%.

Production of ^{257}Db at LISE

Nuclei of ^{257}Db were produced in cold fusion evaporation reaction ^{209}Bi(^{50}Ti,2n)^{257}Db. A molecule of CpTi$(CH_3)_3$ synthesized at IPHC Strasbourg was used to produce a continuous $^{50}Ti^{10+}$ beam with the MIVOC technique [52]. The beam was accelerated to an energy of 4.88 MeV/u to match the peak of the excitation function of the 2n evaporation channel (figure 4.13). It was sent to LISE-D3 room and guided through the spectrometer up to the primary target positioned at the entrance of the Wien filter (figure 2.3, target position b). The average beam intensity at the target position was 300 pnA.
Seventeen targets of ^{209}Bi were mounted on the target wheel (figure 2.5). Thirteen of these targets were made out of Bi_2O_3 with a thickness between 361 and 405 μg/cm^2, and 4 from metallic Bi with a thickness of ∼450 μg/cm^2. The second wheel held carbon foils with a thickness of 35 ± 5 μg/cm^2. The rotation speed of the wheel was set to 1500 rpm in order to keep the targets temperature below the

melting point. ^{257}Db nuclei were separated from the rest of the products by the

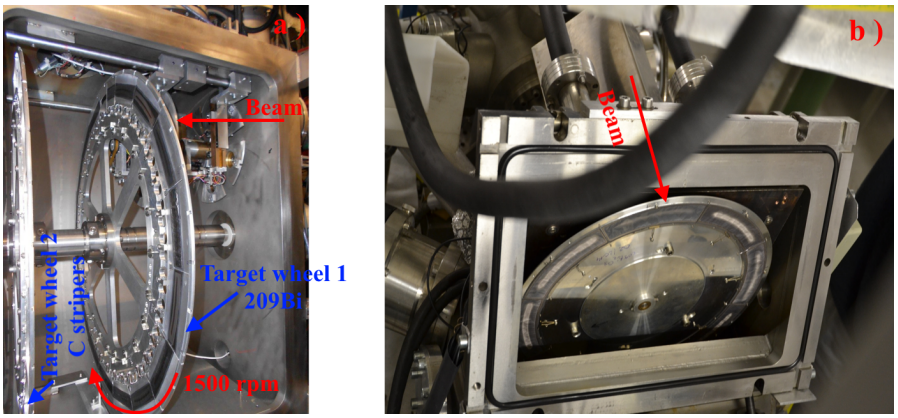

Figure 2.5: a) Target wheels at the entrance of the Wien filter in LISE-D6 room. b) Target wheel at the entrance of SHIP.

Wien filter and sent to the detection setup (Chapter 2.4.1) positioned at the final focal plane in D6 room (figure 2.4).

2.2.2 The SHIP separator

SHIP (Separator of Heavy Ion reaction Products) is a separator at GSI facility, used for the study of heavy, superheavy and elements at the proton drip line [53] (elements with short half lives and small cross sections). In order to use the highest possible beam intensities a rotating target wheel is mounted at the beginning of the 12 m long velocity filter (figure 2.6). The target wheel has a 355 mm diameter, while the distance between the centers of two opposite targets is 310 mm (figure 2.5). A thin C foil (30 μg/cm^2) is positioned 130 mm downstream of the target for charge equilibration.
The filter uses a combination of electric and magnetic fields to separate the evaporation residues by their kinetic properties. ER selection is done in a similar way as with Wien filter at GANIL (Chapter 2.2.1), meaning that the residues are separated according to their velocity $v = E/B \pm \Delta v$.
Even though the separator works on the principle of the Wien filter, it does not have a "classical" Wien filter configuration due to technical reasons at that time (1976). In principle, it is a "double Wien filter" configured in a mirror symmetry. Each of them has a quadrupole triplet, two dipole magnets and an electric condenser designed for high voltage up to $\pm$350 kV. The velocity selection can be adjusted by the horizontal slits positioned in the middle of the filter [53]. However the selection is not perfect and some projectile and target like nuclei still pass the SHIP separator. Two types of projectile like nuclei which pass SHIP can be

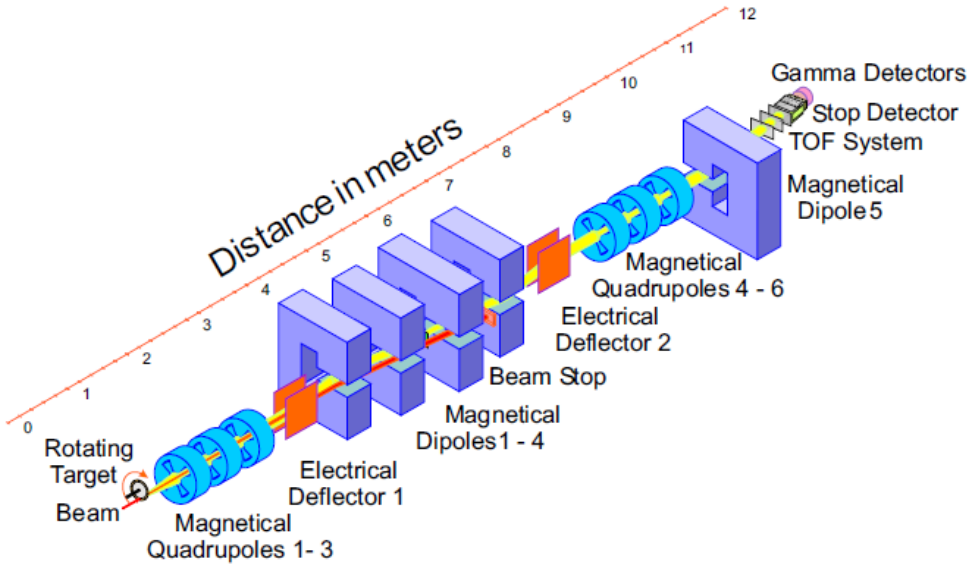

Figure 2.6: SHIP separator, with the indication of different magnets, target position, and detector setup position

identified: scattered projectiles with velocities close to the velocity of the ER, and projectiles with energies close to the beam energy. In order to suppress this background, an additional magnetic dipole (dipole 5 in figure 2.6) was added in 1994 (see also Chapter 2.2.1).
The curvature radius (r) of an ion in a magnetic field ($\overrightarrow{B}$) is given by:

$$r = \overrightarrow{B} \times m\frac{\overrightarrow{v}}{q} = \overrightarrow{B} \times \frac{\overrightarrow{p}}{q} \tag{2.4}$$

where m, q and $\overrightarrow{v}$ are the mass, charge and velocity of the ion, while $\overrightarrow{p} = m\overrightarrow{v}$ is the momentum of the ion.
Scattered projectiles have velocities which are close to the velocity of the ER, however their mass is, in our case, about a factor of five lower, additionally they are considered as highly stripped meaning that their mean charge state is not so different than the charge state of the ER (20-30 % lower). This means that in the same magnetic field these particles will have a curvature radius which is approximately five times lower than the curvature radius of the ER, leading to a bigger deflection of these particles by the magnetic dipole compared to the ER.
On the other hand, the projectiles with energies close to the beam energy actually have the same linear momentum ($\overrightarrow{p}$) as the ER, while having low charge state. This leads to a higher curvature radius in the same magnetic field and a deflection which is smaller than for the ER.

The separator SHIP is characterized with a vertical and horizontal angular acceptance of ±2.7 msr, a velocity acceptance of ±5 % and a charge acceptance of ±10 %.

Production of ^{258}Db at SHIP

The nuclei of ^{258}Db were produced in cold fusion evaporation reaction ^{209}Bi(^{50}Ti,1n)^{258}Db. Pure metallic Ti was used to produce a pulsed $^{50}Ti^{8+}$ beam which was accelerated to an energy of 4.72-4.724 AMeV and had an intensity of 500 pnA on the average at the target position. The linear accelerator UNILAC [54] provides 50 pulses/s: 5 ms of beam followed by 15 ms without beam. Additionally to this experiment, two other experiments were running "parasitically" which left 38.8 pulses/s to be sent to the rotating target of SHIP (figure 2.6). Again, the rotation of the target wheel is synchronized with the pulse structure of the beam [53]. Eight ^{209}Bi targets with a thickness of 415 μg/cm^2 were mounted. A thin carbon foil (30 μg/cm^2) was set behind the target at a distance of 130 mm for charge equilibration. The ^{258}Db nuclei were produced in a 1n cold fusion-evaporation reaction. The evaporation residues were selected by the SHIP separator and sent to the detection area (Chapter 2.4.1) at the final focal plane of SHIP (figure 2.6).

2.2.3 The S^3 spectrometer

The Super Separator Spectrometer (S^3) is a new generation device designed for fundamental physics experiments, with the very high intensity stable ion beams of the superconducting linear accelerator of the SPIRAL2 facility at GANIL [55]. The linear accelerator will provide heavy beams with energies from 2 to 14 MeV/u, and intensities which could exceed 10 pμA, depending on the nature of the ions and target [56]. Such beams will offer an opportunity to overcome the low cross section limitations far from the region of nuclear stability, in the vicinity of superheavy elements, and regions beyond the drip lines, especially around ^{100}Sn [57].
The Super Separator Spectrometer (S^3) is a multipurpose device designed to cope with the high intensity beams produced by the SPIRAL2 accelerator. In order to achieve a 10^{13} beam rejection power, S^3 will be composed of a high acceptance momentum acrhromat followed by a mass spectrometer (mass achromat) with a mass resolution approaching 1/300.
The principal physics cases covered by this device can be separated in four categories [55]:

- Production of super and very heavy elements for the purpose of spectroscopy studies and ground state properties measurements depending on the production rate.

- Production of neutron deficient nuclei (at the proton drip line) for spectroscopy studies, as well as $N = Z$ nuclei for: single particle structure, collectivity, shape coexistence, ground state properties, etc...
- Production of neutron rich nuclei by multi-nucleon transfer for the purpose of single particle structure and magicity evolution studies.
- Ion-ion atomic interactions for atomic physics studies, Fast Ion Slow Ion Collisions (FISIC).

Additionally S^3 will be connected to the DESIR experimental area through the low energy branch REGLIS [55].

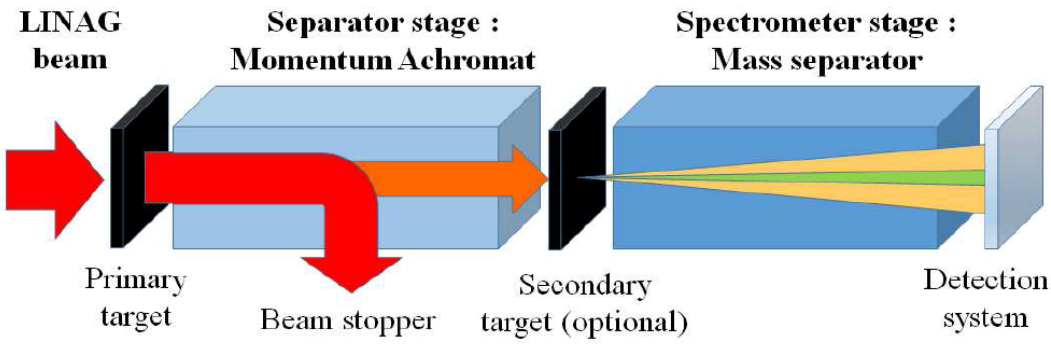

Figure 2.7: Schematic representation of S^3 design. Figure adopted from [58].

A schematic representation of S^3 can be found in figure 2.7. The spectrometer itself is made out of two parts: the momentum achromat for primary beam rejection and the mass separator to select the reaction products. The primary target is positioned before the first stage of the separator, and the detection system at the final focal plane.
Two types of primary targets, and therefore two types of rotating wheels, will be used at S^3 for stable and actinide targets [59]. The targets are confined in a specialized target chamber. Targets made of stable isotopes (ie. lead or bismuth) will be mounted on a large 37 cm radius wheel rotating at ∼3000 rpm. The actinide targets will be mounted on a smaller wheel (8 cm radius) rotating at ∼5000 rpm [58, 59]. A prototype target wheel was tested at LISE,GANIL [59].
The spectrometer is designed to handle beam intensities of 10 pμA or higher. Therefore a two stage device is designed. The first one is the Momentum Achromat (MA) and the second one is the Mass Separator (MS). The primary beam rejection of 99.9% is performed by the momentum achromate. The achromat uses two identical magnetic dipoles to produce a Bρ dispersive plane where the primary

rejection is performed [56, 58]. The first magnetic dipole is specially designed magnet, opened on one side, working at the room temperature. The separated primary beam is sent to a specially designed beam dump. Additional stopping is provided by moving "fingers" and slits to cut unwanted charge states. The third selection is performed in the MS which is made out of an electrostatic dipole coupled to a magnetic dipole to provide an achromatic image at the final focal plane dispersive in m/q (mass/charge) [58, 60].
The optical modes of S^3 are designed to support each of the previously mentioned physics programs. Consequently four different configurations can be set for the moment:

- *High resolution* mode is used for experiments where a high mass resolving power is needed such as $N = Z$ experiments, or for superheavy elements where $\delta M/M$ is small. The obtained mass resolving power at the final focal plane is $R_M = 382$ [58]. This can be seen in figure 2.8, top.
- *High transmission* mode is used for large emittance reactions. The transmission of the residues is increased while the mass resolving power is slightly decreased (figure 2.8, middle).
- *Converging mode* maximizes the transmission of the evaporation residues for experiments which require small beam spot at the focal plane (REGLIS [61]) or do not require good mass resolution (implantation in the focal plane detector of SIRIUS (chapter 3)).
- *High beam rejection* mode is currently identical to the High resolution mode, but could be improved depending on the needs. It is designed for experiments with low cross sections (like superheavy production) to suppress the primary beam as much as possible.

The decay spectroscopy station for SHE (SIRIUS) is discussed in chapter 3.

2.3 Decay spectroscopy

Spectroscopy studies of superheavy elements are possible only if they are artificially produced. Previous sections of this chapter were dedicated to the description of the production facilities. This section gives an insight to the techniques used for probing the structure of the elements such as generic correlation method [62]. A description of specific multi-detector systems used for the experiments is given at the end of the chapter.

Different decay modes present in the region of SHE are described in Chapter 1.3. It

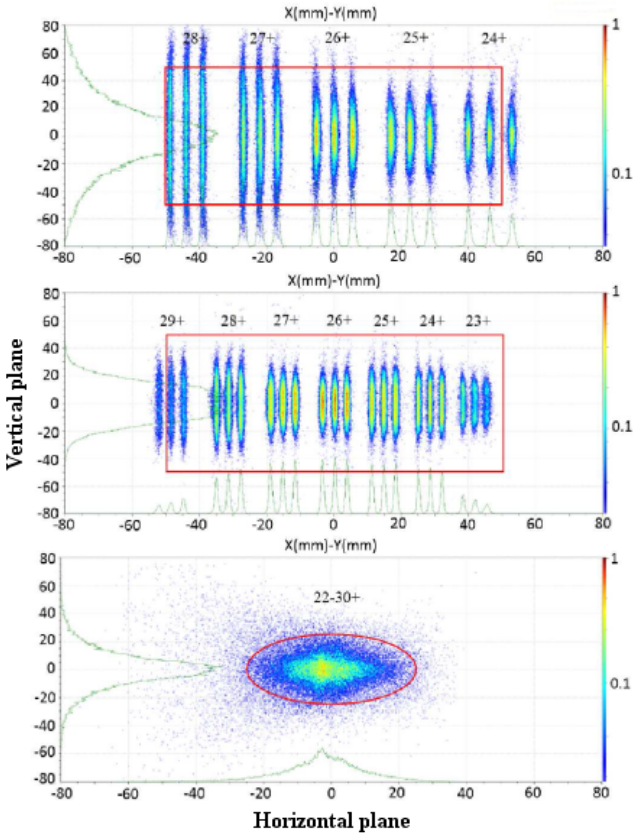

Figure 2.8: Distribution at the final focal plane, showing the five transmitted charge states ($Q_0 = 26+$) of the nuclide of interest and the first two neighboring masses ($A = 99$,100 and 101), for the ^{100}Sn experiment in high mass resolution mode (top), high transmission mode (middle) and converging mode (bottom). In red are detector apertures, DSSD for the first two and gas cell for the last mode. Figure adopted from [58].

was mentioned in chapter 1.3.1 that the α decay of the SHE can provide information both on the structure of the element as well as the structure of the daughter elements. Additionally the identification of the produced elements is performed following the α decay chain, in the case that the chain is finishing in a known element. Techniques used to perform these studies are known as generic correlations. In principle they are based on the correlation studies between the produced ER (recoil) and the emitted α particles (recoil-α correlations). Correlations between different α particles (α-α correlations) are also performed. The study is based on the analysis of the generic α decay chains, an example of which can be found in figure 2.9, starting from the ER succeeded by a series of α decays following the scheme:

$$ER_Z^A \xrightarrow{\alpha_1} D_{Z-2}^{A-4} \xrightarrow{\alpha_2} GD_{(Z-2)-2}^{(A-4)-4} \xrightarrow{\alpha_3} ...$$

Combination of different detectors (multi-detector system) is used for the purpose.

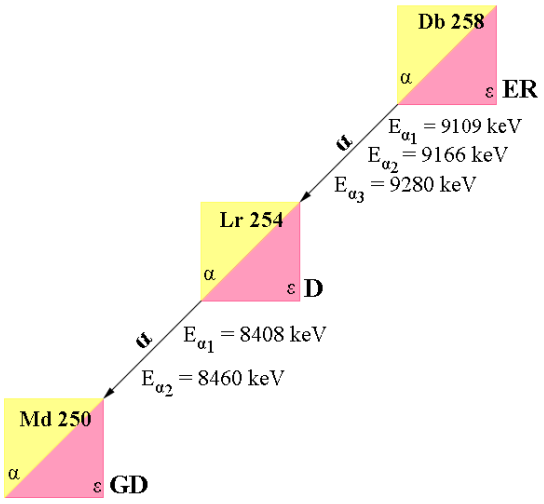

Figure 2.9: Example of the α decay chain of ^{258}Db.

A position sensitive segmented detector, usually a Double-sided Silicon Strip Detector (DSSD), is used to retrieve the position and the energy of the ER and the emitted α particles. The strip width usually used is of the order of mm. For example the DSSD used at GANIL has a strip width of less than 3 mm and 1 mm in X and Y respectively. The typical energy of the emitted α particle is in the range of 8-10 MeV, giving a range of few tens of μm in a silicon detector, where a 9 MeV α has a range of 58 μm. Therefore the correlation of an α particle of a specific energy with an ER in the same position of the silicon detector unambiguously identifies the implanted ion (figure 2.10).

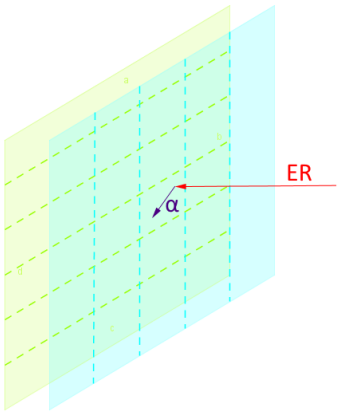

Figure 2.10: Schematic representation of an implantation in a DSSD followed with an emission of an α particle in the same pixel.

The implantation depth of the ER in a silicon detector is small due to its low energy (^{257}Db with an energy of 33 MeV has an implantation depth of 5.5 μm). As a result, 40-50 % of emitted α particles escape the implantation detector, leaving just a part of their energy in the DSSD. To counterbalance this loss, a series of silicon detectors usually surrounds (box/tunnel configuration) the implantation detector registering 60-70 % of escaped α particles.
Additional information on the structure of the ER and its daughter can be obtained from the other decay channels such as Spontaneous Fission (SF) and Conversion Electrons (CE) or γ and X-rays.
Probability of CE emission is high in heavy Z nuclei (chapter 1.3.3). When the α decay is immediately followed by internal conversion (emission of CE) in the daughter nuclei, the registered energy in the implantation detector can take any value between the true energy of the α decay and the sum of the true α particle energy and all of the energies of the other particles/photons emitted during the conversion and atomic rearrangement processes [33]. This fact has to be taken into account while analyzing the data.
Germanium detectors are used for γ and X-ray measurements. To be able to assign them to a specific isomer, time and energy gates are used in correlation with ER and α particles. For example, one way to identify the γ-ray transitions from the ER is to require that the γ-ray transition comes in time (time gate) before the α decay of a specific energy (energy gate).

2.4 Experimental setups

The last part of this chapter is dedicated to the description of the multi-detector systems used at GANIL and at GSI for the performed experiments. This chapter gives a technical description of the detector systems and corresponding electronics chains and acquisition systems. Calibration procedures and physics analysis of the obtained data are treated in chapters 4 and 5.

2.4.1 LISE: multi-detector system

The multi-detector system at LISE is made of two Time Of Flight (TOF) detectors, a DSSD, four Single-sided Silicon Strip Detectors (SSSD) and four germanium (Ge) clovers (figure 2.11). It was used for spectroscopic studies of ^{257}Db produced in a 2n cold fusion evaporation reaction of ^{50}Ti beam on a ^{209}Bi target (Chapter 2.2.1).
TOF detectors are generally used for position and time measurements. However, these measurements introduce angular straggling and energy loss due to the interaction between the ER and the TOF detectors. Thus these effects have to be minimized due to the low production of SHE. To meet these criteria, Secondary Electron Detection (SED) principle (detailed description of the principle can be found in Chapter 3.2) is usually applied.

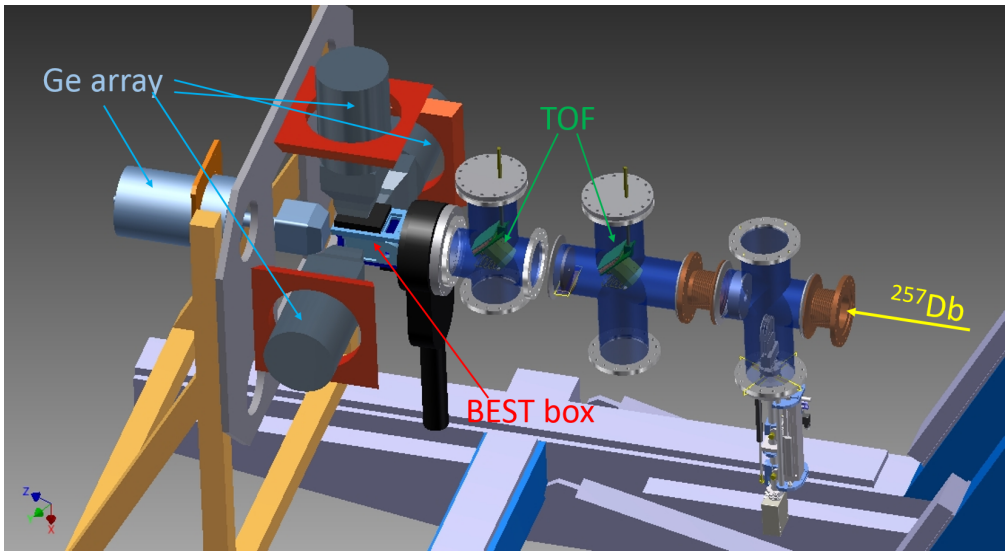

Figure 2.11: LISE-D6 final focal plane, with the detection setup for ^{257}Db experiment.

The TOF detectors "Galotte" [63] installed, at LISE, detect secondary electrons

emitted when heavy particles (ER, projectiles, etc...) pass a thin aluminized Mylar foil (0.5-1.1 μm). The foil is positioned with an angle of 45^o compared to the beam, but parallel to the Micro-Channel Plate detectors (MCP) positioned outside of the beam. An electric field accelerates these electrons from the foil to the MCP. In the performed experiment, only the time information was retrieved from the TOF detectors. During the calibration (^{170}Er+^{50}Ti) run (Chapter 4.1) two TOF detectors were used, enabling time measurements between the two TOF detectors and between each of the TOF detectors and the DSSD, giving in total 3 time information. For ^{257}Db run, it was decided to use just the second Galotte (the one closer to the DSSD) due to straggling loss induced by the first Galotte. Table 2.1 shows the percentage of events reaching the DSSD compared to the amount of events passing the galottes. The configuration with just one galotte closer to the DSSD shows the best performances. Consequently, this configuration was chosen for the ^{257}Db run.

Run	Galotte 1	Galotte	DSSD [%]
135	in	in	85
137	in	in	88
139		in	98
140		in	98
146	in		89
148	in		89

Table 2.1: The table shows the position of the TOF ("Galotte") detector with respect to the beam. The last column represents the percentage of events reaching the detector compared to the number of events passing the TOF detectors.

After passing the TOF detector, the ER is implanted in a DSSD (implantation detector). A detector with an active surface of 50x50 mm^2 was used. It had 16 horizontal strips (X) on the front side and 48 vertical strips (Y) on the back side that were plugged in GANIL designed pre-amplifiers with a gain of 30 mV/MeV. The 64 pre-amplified signals coming from the DSSD strips were sent to four 16 channel CAEN (N568B) spectroscopy amplifiers with three different output signals (OUT, XOUT and FOUT), as can be seen on figure 2.13. The OUT (amplification = 1) signals from the amplifiers were sent to two 32 channel GANIL ADCs, Analog to Digital Converter (XDC3214). This part of the electronics chain was used for ER energy measurements and was called Low Gain (LG) branch. The XOUT (amplification = 10) signals were sent to two 32 channel GANIL ADCs (XDC3214). The signals coming from these ADCs were corresponding to measurements connected to decay events and they were called High Gain (HG) branch. The FOUT (Fast OUT) of the amplifier was sent to four 16 channel low threshold discrim-

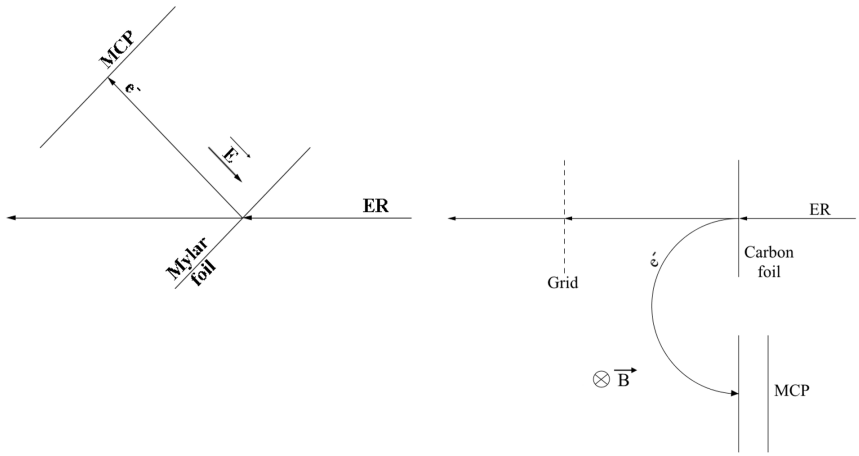

Figure 2.12: Left: Schematic representation of the TOF detector "Galotte" at LISE.
Right: Schematic representation of the TOF detector at SHIP.

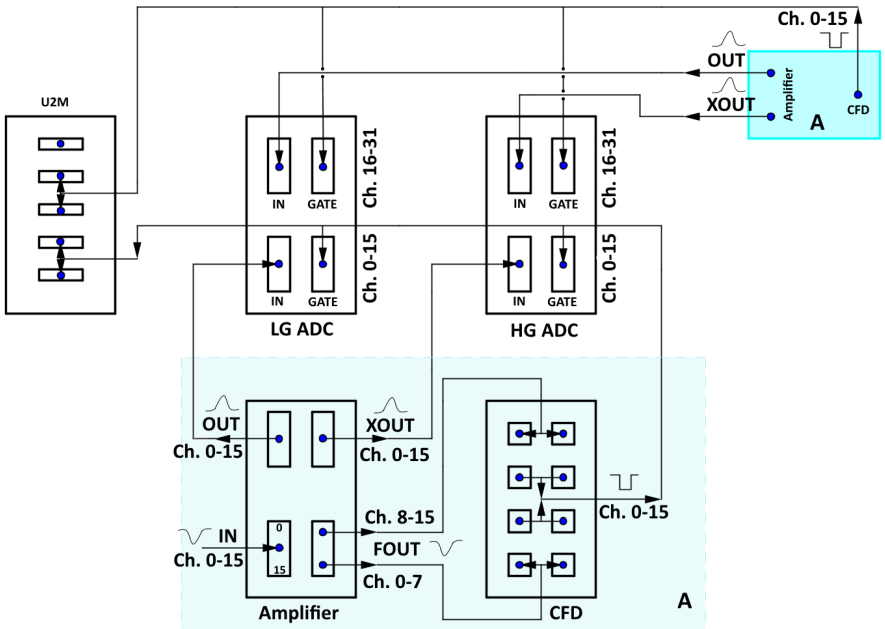

Figure 2.13: Schematic representation of the electronics chain for 32 channels of DSSD. The other 32 channels were connected in a same way.

inators CAEN (V814). Discriminators were used in an individual trigger mode. This means that they were sending a signal to the ADCs (both branches) for each channel which triggered with a signal higher than the preset threshold. These signals were further sent to a U2M module (figure 2.13). A U2M device is a scaler which enables visualization of all the present channels, and gives the number of counts for each of them [64]. Four Single-sided Silicon Strip Detectors (SSSSD)

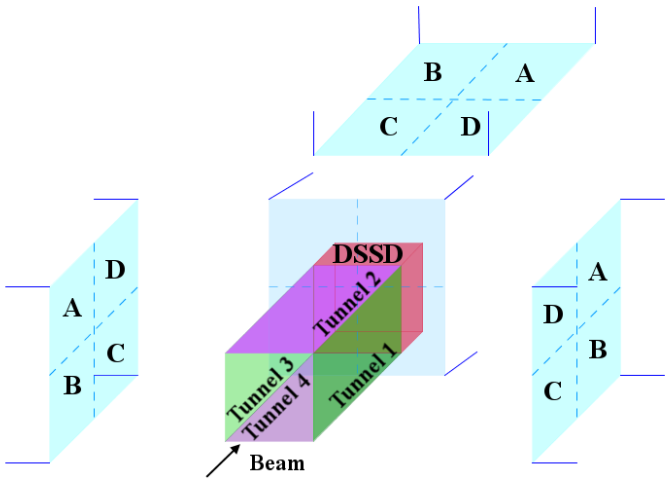

Figure 2.14: Schematic representation of the Tunnel detector surrounding the DSSD, and the germanium clovers (crystals are labeled) surrounding the silicon detectors.

in "Tunnel" configuration were surrounding the DSSD. The strips of the "Tunnel" detectors were set parallel to the beam axis. Each SSSSD had an active surface of 50x50 mm^2 divided in four strips and was mounted on a 60x120 mm^2 resin board manufactured by ISOLA. The front-face dead-layer thickness was <25 nm Si equivalent. The pre-amplifiers (designed by GANIL) are mounted on the reverse side of the support board. The 16 pre-amplified signals from the "Tunnel" detector were sent to one CAEN (N568B) 16 channel spectroscopy amplifier. The XOUT (amplification = 10) was sent to one GANIL ADC (XDC3214). The FOUT of the amplifier was sent to the 16 channel CAEN low threshold discriminator (V814). The individual triggers coming from the discriminator were sent to the corresponding ADC and finished in U2M shared with the germanium detectors (figure 2.15). All silicon detectors were cooled to -20^o C with liquid silicon. The silicon detectors were surrounded (figure 2.14) by four EXOGAM germanium (Ge) clovers with four crystals each [65,66]. The germanium detectors were not shielded, neither by passive nor by active shielding, from the background γ-ray radiation. The pre-amplified 16 channels from EXOGAM were sent to a 16 channel CAEN (N568B)

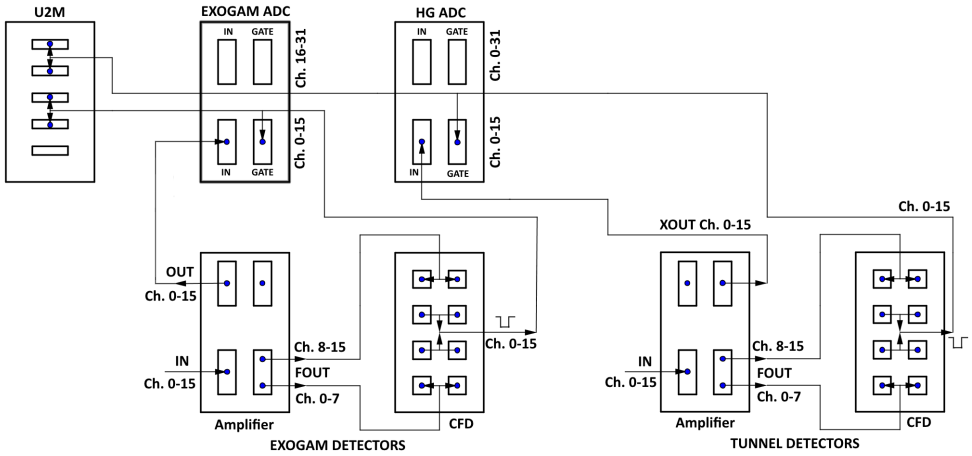

Figure 2.15: Schematic representation of the electronics chains for Tunnel and germanium detectors.

spectroscopy amplifier. Signals from the OUT (amplification = 1) of the amplifier were sent to GANIL ADC (XDC3214), while the FOUT was sent to 16 channel low threshold discriminator CAEN (V814). Individual triggers coming from the discriminator were sent to the corresponding ADC and finished in a U2M shared with the "Tunnel" detector (figure 2.15).
Time assignment to the events was done globally. For this purpose a CENTRUM module with a time unit of 10 ns was used [64]. CENTRUM assigns time stamp on request, meaning that whenever a detector gets triggered by an event it sends a request to the CENTRUM, and the CENTRUM sends back a time stamp for this event.

Acquisition system

Three separate acquisition systems were used for the ^{257}Db run, because the standard GANIL acquisition GRU/NARVAL [67, 68] at that time could not handle a multi-branch system. Consequently, the three acquisitions corresponded to three hardware set triggers. One acquisition was used for ER identification, another one for decay identification, and the last one for gamma-rays. The ER identification (LG branch) was achieved by making the coincidence between the TOF detector(s) and the DSSD in a time interval of 1-5 μs, depending on the run. The decay identification (HG branch) was done by making the anti-coincidence between the TOF detector(s) and the DSSD. These two acquisitions enabled global separation of the ER and decay products in the DSSD detector. The Tunnel detector was included only in the HG branch, since it is used for escaped decay products. The last acquisition was used for γ and X-rays (only germanium detectors). The ger-

manium detectors were running in triggerless mode, meaning that every event that was seen by the detectors was registered, provided it was not coming in the dead time of the system. This way the dead time of the γ detectors was reduced to a minimum. The time stamp of the events was obtained from the CENTRUM, as explained in the previous section. All three acquisitions were communicating with this module providing a global time stamp. Online analysis was done with Vigru [67], while offline analysis was made with a personally developed code in C/C^{++} (Chapter 4.2.2).

2.4.2 SHIP: multi-detector system

The multi-detector system at SHIP is made of two TOF detectors, one Position sensitive Silicon Strip Detector (PSSD), six SSSDs and one germanium clover (figure 2.16). The performed experiment was a spectroscopy study of ^{258}Db produced in a 1n cold fusion-evaporation reaction with ^{50}Ti beam on a ^{209}Bi target (Chapter 2.2.2).
The TOF detectors of SHIP detect secondary electrons emitted when heavy particles (ER, projectiles, etc...) pass a thin carbon foil (20-30 μg/cm^2) covered by a MgO layer (10-20 μg/cm^2) to enhance emissivity. The foil is placed perpendicular to the beam. The electrons are deflected by a magnetic field to a MCP positioned outside of the beam, parallel to the foil. Three TOF detectors are mounted in the

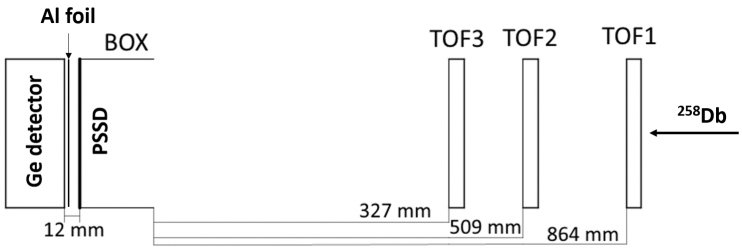

Figure 2.16: Schematic representation of the detection system for ^{258}Db experiment (TOF1 detector was not used).

beam line, however just two (TOF2 and TOF3) were used (figure 2.16). TOF1 was not used due to the loss of ER because of straggling, measured to 25%. Time difference is measured between the two TOF detectors, as well as between each of the TOF and PSSD and BOX detectors. Signals from the TOF detectors are vetoed by the stop detector and are registered only if there is a prompt coincidence with the PSSD. The ER were stopped in a PSSD of 35x80 mm^2, with X direction (80 mm) divided in 16 vertical strips covered with a resistive layer on the side

facing the beam. Charge collection on both ends of each strip enables Y position calculation (Chapter 5). Both ends (top and bottom) of each strip of the PSSD

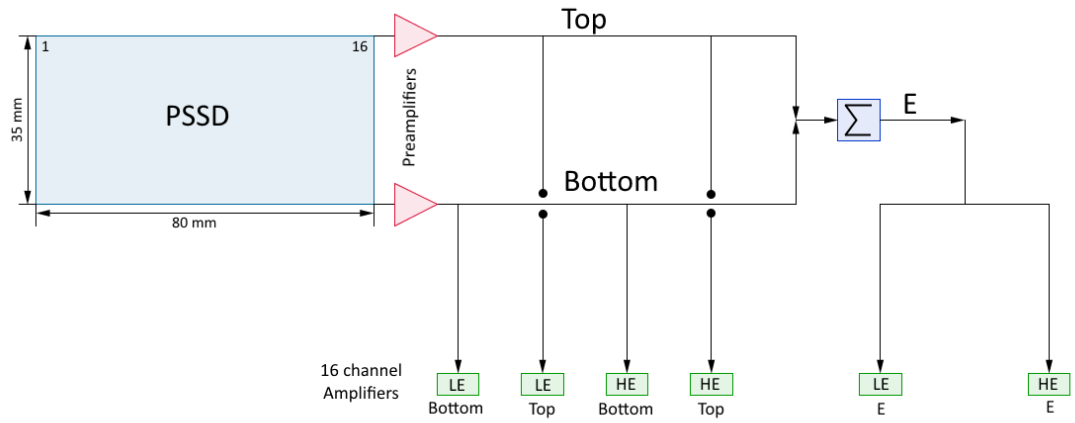

Figure 2.17: Schematic representation of the PSSD with the read out of energy and Y position.

are connected to charge sensitive pre-amplifiers. The total energy deposited in a strip is obtained by summing these signals (figure 2.17). The preamplified signals (16x3) from the PSSD (top, bottom and E) are sent to spectroscopy amplifiers. Each signal has two amplifications: high amplification corresponding to the Low Energy (LE) branch and low amplification corresponding to High Energy (HE) branch. The HE branch is used for ER and spontaneous fission identification and its amplification range extends up to 320 MeV. The LE branch is used for decay spectroscopy and its amplification range extends up to 16 MeV. In order to register events with charge split between two neighboring strips the signals from the amplifiers are split in odd (1,3,5...15) and even (2,4,6..16) channels corresponding to odd/even strips of the PSSD. To reduce the number of electronics modules required, the signals are further sent to multiplexers for the LE branch and mixers for the HE branch. Multiplexers are used for the LE (decay) branch to achieve better resolution. They are channel selective, and send a signal to the ADC only if the pulse height of this signal is above a certain threshold. On the other hand, mixers are used in HE (ER) branch and accept all the incoming signals. The output signal of the mixer is a sum of the signal from the channel which triggered and the noise from the other 15 channels of the mixer. The signals from the ADCs are further sent to ADC multiplexers (AMUX) boards (figure 2.18). AMUX boards are used to process the signals from the ADCs and do an event build up that is further sent to the computer [69]. The corresponding strip number for both LE and HE branches is read from the bit pattern modules fed by the energy sig-

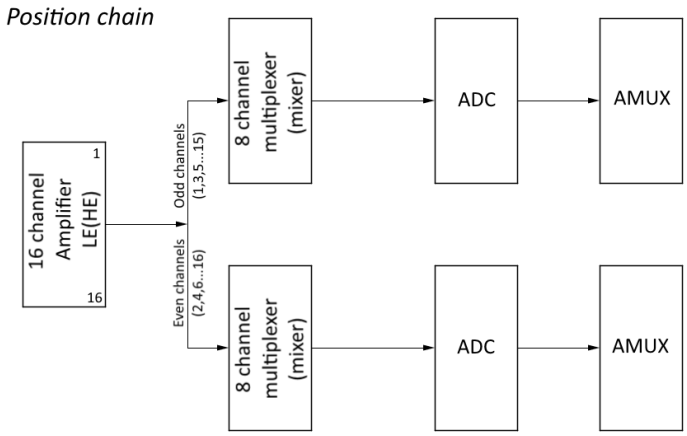

Figure 2.18: Schematic representation of the Y position readout (resistive layer) after the amplifiers.

nals (figure 2.19). The bit pattern module gives a signal coded in 16 bits. The output of this module will give the number of the strip which fired. To illustrate the working principle of the module, an example can be used: if the output of the module is 128 it means that the strip which fired is strip 8 as can be seen from the following:

$$128 = 0 \cdot 2^0 + 0 \cdot 2^1 + 0 \cdot 2^2 + 0 \cdot 2^3 + 0 \cdot 2^4 + 0 \cdot 2^5 + 0 \cdot 2^6 + 1 \cdot 2^7 + ... + 0 \cdot 2^{15}$$

where 2^0 corresponds to strip number 1, 2^1 to strip number 2, until strip number 16 (2^{15}).
The implantation detector is surrounded by six SSSDs (BOX) in backward configuration (figure 2.20). The 2 SSSDs labeld SSSD1 and SSSD2 have 6 channels each. The other four (SSSD3-6) have 4 channels each. All the pre-amplified signals from the BOX detector are sent to amplification modules. As for the PSSD two types of amplifications are applied on these signals: 10X (LE) and 1X (HE). All silicon detectors are cooled with ethanol to -20^o C. On the back side of the PSSD detector, a germanium clover with four crystals is positioned (figure 2.16). A thin (1.5 mm) Al window positioned at the back of the vacuum chamber behind the PSSD separates the high vacuum from the outside atmosphere. The clover is shielded by a passive shield made (from inside to outside) of 2x1 mm copper (Cu), 2x1 mm cadmium (Cd), 2x4 mm lead (Pb). The four channels are amplified and sent to the ADC. Short time differences (< 5 μs) between the γ-rays and the particles in the PSSD were measured by a TAC. "Time zero" of the TAC was set to channel 2000 to be able to register the γ-rays preceding the particles in the PSSD.

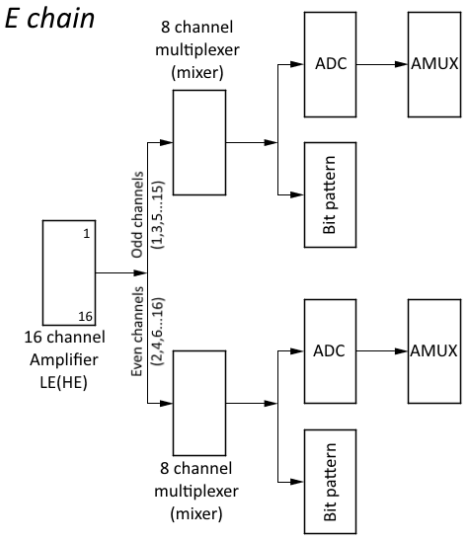

Figure 2.19: Schematic representation of the PSSD energy readout after the amplifiers.

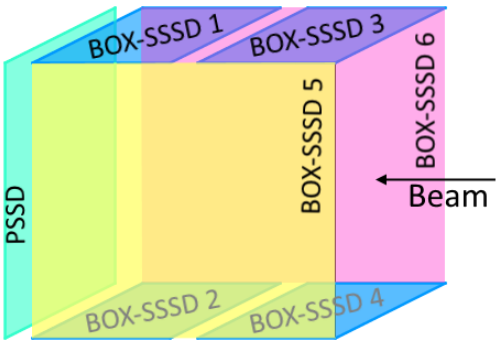

Figure 2.20: Geometry of the PSSD and BOX detectors for ^{258}Db experiment.

Acquisition system

The MBS (Multi-Branch System) software developed at GSI is used as an acquisition system [70]. The event read out is the following: an event registered in an ADC triggers the data acquisition and starts a coincidence time of 5 μs. After this coincidence time, the ADCs are inhibited for 15 μs. In this time no data input is accepted and the acquisition is in a dead time. This would be problematic if short half-lives of short lived isomers are studied. Online analysis of the data is done by a GSI developed code called GO4 [71]. The offline analysis was done by a personally developed code in C/C^{++} (Chapter 4.2.2).

Chapter 3

New instrumentation for SHE identification at GANIL/S^3 facility

The study of superheavy elements requires specific installations such as the milti-detector systems used at LISE 2.4.1 and SHIP 2.4.2 which were described previously in chapter 2. A short description of the multi-detector system which will be installed at S^3 2.2.3 for the same purpose is given in this chapter.
The multi-detector system SIRIUS (Spectroscopy and Identification of Rare Isotopes Using S^3) consists of two tracking detectors, a "Tunnel" detector, a DSSSD and an array of germanium detectors, as can be seen in figure 3.1. Similarities to the previously described setups at LISE and SHIP can be observed.

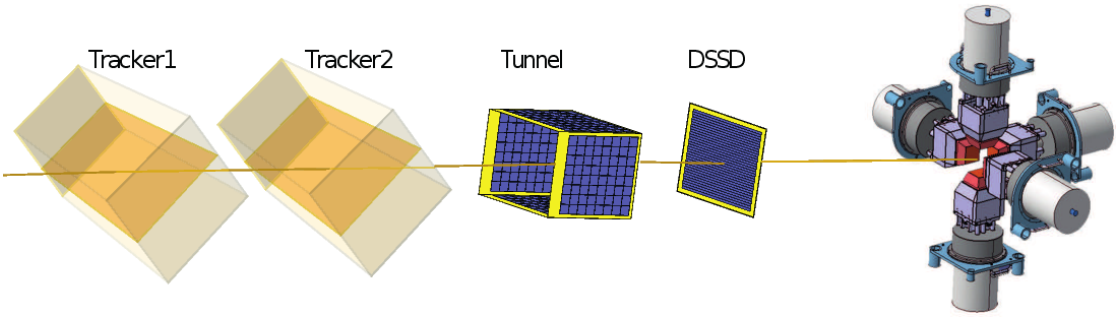

Figure 3.1: Schematic representation of the multi-detector system at S^3.

The combination of the silicon detectors and the germanium detectors positioned at the final focal plane of S^3 is used to perform lifetime and energy decay (α, β, fission, conversion electrons, etc...) measurements based on the recoil decay tagging method (4.2 and 5.2).

A highly segmented ($128x128$ strips) DSSSD is used for implantation purposes and detection of the decay particles. It is surrounded by a "Tunnel" of four silicon pad detectors used for detecting the charged particles (α, electrons and protons) which escaped from the implantation detector (DSSSD). Finally the complete system is surrounded by an array of germanium detectors used for delayed gamma decay spectroscopy. More details about these detectors and the requirements they need to fulfill can be found in [57, 72–74].

High precision tracker detectors are positioned upstream from the silicon box (figure 3.1). They are used for the identification of produced nuclei based on the total kinematic energy and velocity of the recoil. Consequently, precise time-of-flight and energy measurements, together with the S^3 spectrometer, are necessary to achieve a mass resolution better than 1/300. Additionally, the produced nuclei in the region of heavy and superheavy elements are characterized with low kinetic energy of the recoil. Therefore the interaction with the tracking detectors has to be minimal, limiting the angular and energy straggling [72]. The final goal is a large size (20x10cm^2) tracking detector with less than 1.5 mm FWHM spatial resolution and 300 ps FWHM time resolution.

The concept of S^3 tracking detectors is based on the secondary electron detection principle previously used for the tracking detectors of VAMOS at GANIL [75]. However due to the requirements stated earlier, it is necessary to develop a new tracking detector for S^3.
A part of this thesis was committed to the development of these tracking detectors to which the chapter 3 is dedicated. The progress in their development is also discussed.
The chapter is organized in the following way. The physics background is given in section 3.1. It is followed by the description of the SED principle 3.2 and the produced prototype detectors 3.3. The results obtained from the tests on the prototypes are discussed in 3.4. The summary and conclusions can be found in 3.5.

3.1 Gas detectors

Gaseous detectors are widely used since 1970's. The popularity of these detectors can be explained with their characteristics such as: covering large solid angles for almost all suitable geometrical configurations, good efficiency in measuring TOF and position, high particle rate capabilities with no radiation damage and finally, they are easy to repair.
The working principle of these detectors is based on the ionization of the gas inside the detector. When a charged particles passes through a gas medium, it creates electron-ion pairs. In general a gas detector is a chamber filled with gas with

an anode collecting the created electrons and a cathode collecting the ions. The operation of the gas detector depends on several factors such as: strength of the electric field, gas used, geometry of the chamber and detectors, etc.
This section gives a summary of different processes caused by the interaction of an ionizing particle with a gas medium. The behavior of the created electron-ion pairs in dependance of the electric field is discussed as well. The main references used for this section are [76], [77] and [78]. Additional references can be found in the text itself.

3.1.1 Ionization and recombination processes in gases

Energy loss of an incident charged particle in a gas causes two types of reactions: ionization and excitation. The type of the reaction depends on the amount of energy transferred from the incident particle to the atoms of the medium. The average differential energy loss is described by Bethe-Bloch formula in relativistic quantum mechanics framework:

$$\frac{dE}{dX} = -\frac{2\pi N z^2 e^4}{(4\pi\epsilon_0)^2\, mc^2}\frac{Z}{A}\frac{\rho}{\beta^2}\left[ln\frac{2mc^2\beta^2 E_M}{I^2(1-\beta^2)} - 2\beta^2\right] \tag{3.1}$$

- N is the Avogadro number (6.22 10^{-23} mol^{-1}),
- mc^2 is the mass of the electron (0.511 MeV)
- e is the charge of the electron (1.6 10^{-19} C),
- Z and A are the atomic number and mass (g/mol) of the medium respectively
- ρ (g/cm^3) and I are the density and ionization potential of the medium respectively
- z and $\beta = v/c$ are the charge and velocity of the projectile
- I is the average excitation energy of the medium, which can be expressed as $I \simeq I_0 Z$ ($I_0 \simeq 10eV$).

From here, one can calculate the maximum amount of energy (E_M) which can be transferred to an electron:

$$E_M = \frac{2mc^2\beta^2}{1-\beta^2} \tag{3.2}$$

Ionization process can occur if the energy which is transferred to an atom exceeds the ionization potential of the atom. In this case an electron-ion pair is formed. The ejected electrons are liberated with an energy which can assume any value up

to the maximum allowed value (E_M equation 3.2). Depending on the amount of energy, some electrons can further ionize the gas and trigger emission of secondary electrons. These "high" energy electrons are called δ electrons.
Excitation of the atom requires less energy than ionization. It is a process in which an electron from a lower electron shell of the atom gets transferred to a higher shell. Consequently, the energy transferred by the incident particle to the atom is equal to the energy difference between these two electron shells. This process does not create free charged particles and it does not contribute to the detection process. If an atom is excited to its metastable state it can transfer its energy to another atom causing ionization. However, ionization occurs only if the excitation energy of this atom is higher than the ionization potential of another atom. This is called penning effect.
For the detector to work properly, it is important that the created electron-ion pairs remain free long enough to be collected on the anode and cathode respectively. However, the created particles move through the gas and interact. In the absence of an electric field the attractive Coulomb force acts on the electron-ion pairs resulting in recombination. These pairs are then lost and do not participate in the detection anymore.
The second cause of the loss of electron-ion pairs comes from electron attachment where an electronegative ion captures a free electron. Consequently the presence of electronegative atoms and molecules in the detector reduces the efficiency.

3.1.2 Transport of charged particles in gases

The operation of the detector is dependent on the behavior of the created charged particles in the electric field. The spatial, time and energy resolution of the detector depend on variables such as drift speed, diffusion and amplification in the electric field.

Diffusion

In the absence of an electric field, the electron-ion pairs created by the incident charged particle diffuse outwards from their formation point. In this process, they interact with the surrounding gas and lose their energy, rapidly reaching a thermal equilibrium with the surrounding gas. These charged particles then have a Maxwellian energy distribution ($F(\epsilon)$):

$$F(\epsilon) = C\sqrt{\epsilon}\, exp\left(-\frac{\epsilon}{kT}\right) \tag{3.3}$$

here k is the Boltzmann constant ($1.38\ 10^{-23}$ $(m^2kg)/(Ks^2)$), T is the temperature in Kelvin (K), ϵ is the energy of the charged particle. Simple kinetic theory of gases

gives the average thermal energy $\epsilon_T = 3/2kT = 0.035\ eV$ in normal conditions. In this case, the charged particle diffusion from the point of creation takes a shape of a Gaussian distribution which increases with time:

$$\frac{dN}{N} = \frac{1}{\sqrt{4\pi Dt}}\, exp\left(-\frac{x^2}{4Dt}\right) dx \tag{3.4}$$

where dN/N is the charge density in dx at a distance x from the point of creation in time t. D is the diffusion coefficient and it enables resolution calculation in x, $\sigma_x = \sqrt{2Dt}$.

Electron drift

When an electric field is applied, the created charged particles move along the field lines in opposite directions. However, the characteristics of these motions for ions and electrons are different.
Due to their small mass, electrons are very sensitive to the applied electric field. The energy they gain from the acceleration in the field is much bigger compared to the thermal energy. Moreover, the energy lost in a collision with the surrounding atoms is fastly recovered by the acceleration in the field between two collisions. Consequently the drift velocity (v) of electrons depends on the electric field ($\overrightarrow{E}$) and can be written as:

$$v = \frac{e}{2m} E\tau \tag{3.5}$$

where e and m are the charge and mass of the electron, and τ is the time between two collisions of the electron. The collision cross sections strongly depends on the energy of the electron and consequently on the strength of the electric field ($\overrightarrow{E}$). The wavelength of the electrons approaches those of the atoms of the gas, causing complex quantum-mechanical processes (Ramsauer effect) responsible for the appearance of the minima and maxima in the collision cross sections. It is possible to calculate the energy distribution of electrons in an electric field starting from the classical theory of electron diffusion in the gas and using the Maxwell-Boltzmann transport equation [79]. Under the condition that just a small amount of electrons ionizes the atoms of the gas, the energy distribution can be written as:

$$F(\epsilon) = c\sqrt{\epsilon}\, exp\left(-\int \frac{3\Lambda(\epsilon)\epsilon d\epsilon}{[eE\lambda(\epsilon)]^2 + 3\epsilon kT\Lambda(\epsilon)}\right) \tag{3.6}$$

where

- ϵ is the energy of the electron,
- $\Lambda(\epsilon)$ is the energy lost in each collision

- $\lambda(\epsilon) = (N\sigma(\epsilon))^{-1}$ is the mean free path of the electron,
- $\sigma(\epsilon)$ is collision cross section
- N is the number of atoms per volume unit

If the elastic and inelastic cross sections are known, the velocity and diffusion coefficient of electrons are given by:

$$v(E) = -\frac{2eE}{3m}\int \epsilon\lambda(\epsilon)\frac{\partial[F(\epsilon)u^{-1}]}{\partial\epsilon}d\epsilon \tag{3.7}$$

$$D(E) = \int \frac{1}{3}u\lambda(\epsilon)F(\epsilon)d\epsilon \tag{3.8}$$

where $u = \sqrt{2\epsilon/m}$ (cm/μs) is the velocity of electrons with energy ϵ. These values are highly dependent of the used gas. Different experimental investigations of the gas influence on the drift of the electrons can be found in [80].

Ion drift

The ion mass is significantly bigger than the electrons one, consequently the energy they gain from the acceleration in the electric field is much smaller. Additionally the energy loss in the collisions is rather big and is just partly recovered by the acceleration in the field. As a result, the energy distribution of ions stays close to a Maxwellian distribution in a wide range of the electric field. The drift velocity (u) of the ions shows a linear proportionality to the reduced field (E/P) up to very high fields. Therefore it is convenient to define the mobility (μ^+) of the ion as:

$$\mu^+ = u\left(\frac{EP_0}{P}\right)^{-1} \tag{3.9}$$

where P is the pressure and P_0 is the standard pressure (1 bar). The ion mobility stays small and almost constant with the electric field.

3.1.3 Operational modes of gas detectors

The amount of ions collected on the cathode in dependance of the applied electric field defines different operational modes of the gas detectors (figure 3.2). Generally 5 different regions can be distinguished.

Region I (recombination): The applied electric field is very weak or non existent. The produced electron-ion pairs diffuse outward of their point of creation, interacting with the gas. This interaction causes energy loss and, as a result, the created pairs reach a thermal equilibrium with the gas and recombine before they

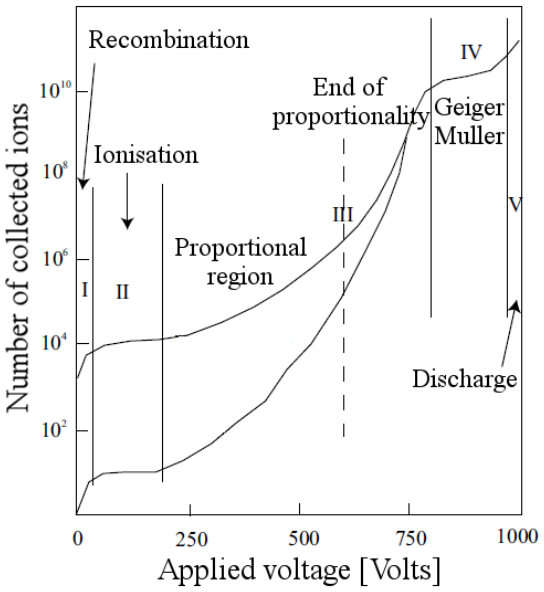

Figure 3.2: The different regions of operation of gas-filled detectors. Figure adopted from [77].

can be collected on the electrodes.

Region II (ionization): The applied electric field is higher than in previous case and prevents the electrons to reach a thermal equilibrium within the gas. The created charged particles are collected on the electrodes.

Region III (proportional): The strength of the electric field is increased compared to region II. Consequently the electrons produced in the ionization process gain enough energy (from the electric field) to cause further ionization of the gas through collision. The liberated electrons will then also ionize the gas and the process repeats itself. As a result, a ionization cascade is formed, called Townsend avalanche. The avalanche permits amplification of the input signal proportionally to the initial energy of the incident particle. The inverse of the mean free path of the electrons performing the ionization by collision is described by the first Townsend coefficient (α). Alpha is the number of electron-ion pairs produced per unit length of the drift. From here the number of particles (electrons) dn produced over a distance dx is:

$$dn = n\alpha dx \tag{3.10}$$

In a non-uniform field the total number of produced particles for a thickness d can be calculated as:

$$n = n_0 \, exp\left(\int_0^d \alpha(x)dx\right) \tag{3.11}$$

The first Townsend coefficient can be parametrized in dependance of the electric field in the following way [81]:

$$\frac{\alpha}{P} = A\, exp\left(\frac{BP}{E}\right) \tag{3.12}$$

where A and B are experimentally determined constants and P is the pressure. It has to be noted that this equation 3.12 is not valid for very strong electric fields. The number of charged particles collected on the electrodes is directly proportional to the initial energy deposited by the incident particle. This permits identification of the incident particle and measurement of its energy. With the further increase of the electric field the proportionality disappears.

Region IV *(Geiger − Müller)*: The strength of the electric field is increased even further and it reaches really high values. In this case the field is so strong that an avalanche can be created with a single electron-ion pair. The output signal is not anymore proportional to the energy of the incident particle.

Region V (discharge): Is the region of a constant discharge. The applied electric field is so high that it causes a series of avalanches over the length of the anode (continuous discharge).

3.1.4 Low pressure gas detectors

The configuration of the chambers and the gas fillings of the detectors, working at normal (atmospheric) pressures, were based on the physics behavior of charged particles in the gas described previously in this Chapter 3.1.
The detector is usually filled with a mixture of a noble gas and a quencher. The choice to use noble gas instead of complex molecules for the filling of the detector was based on the fact that lower voltages are needed to start an avalanche in the detector (figure 3.3). Additionally, noble gases are chemically inert, meaning that they do not cause electron attachment (chapter 3.1.1). However, the problem with noble gases is that they are not able to sustain high gains without entering the zone of permanent discharge. The cascade of avalanches is started by the emitted photons, either in deexcitation process or by the interaction of excited atom with the material of the cathode. To overcome this issue a quencher made of poly-atomic gas is added. The quencher is able to absorb the photons and prevent the discharge to occur.
When gas detectors started to be used for low energy nuclear physics, it was clear that some modification of these detectors were necessary. The detectors were, at first, placed in vacuum on the beam trajectory. This caused a large pressure difference between the interior and exterior of the detector, which the entrance

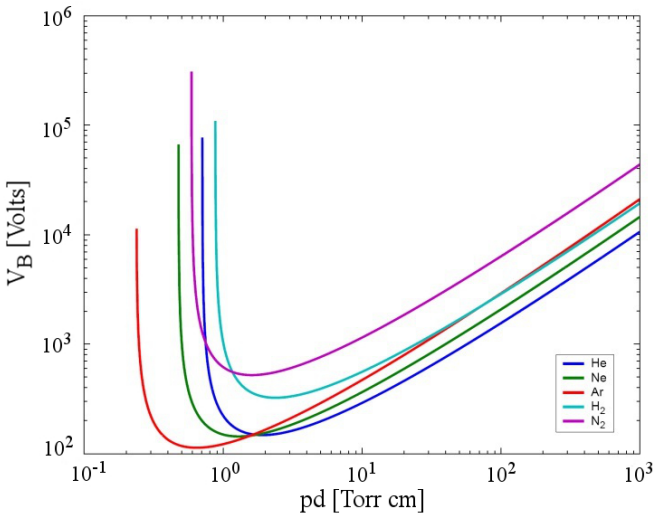

Figure 3.3: Paschens curve: breakdown voltage vs the product of pressure and gap length.

windows could not sustain. Consequently, the pressure inside the detector is reduced, leading to the reduced pressure difference between the inside and outside of the detector allowing to keep thin entrance windows. At lower pressures, the avalanche is triggered at lower electric fields and the amount of quencher (typically a few percent at normal pressure) is not sufficient to prevent the discharge. Therefore the gas filling is changed, and pure quencher gases are used such as isobutane or tetrafluoromethane.
However the window thickness reduction is not enough for very low energy nuclei (∼MeV/n). The straggling introduced by passing through the gas detector for these slow ions is too big. The solution is to remove completely the detector from the beam trajectory and leave just a small amount of material in beam to reduce the interaction with the heavy ions but to still be able to track them. This detection mechanism is known under the name of Secondary Electron Detection (SED) principle and it is in detail described in the next section 3.2.
Table 3.1 shows different detectors used for tracking of heavy ions. Their advantages and disadvantages are stated as well as their influence on the passing heavy ions of ^{100}Sn. The emissive foil detectors (SED) induce the minimal straggling, compared to the other detectors.

Detector /thickness	Advantages	Drawbacks	Thickness [mg/cm^2]	dE [MeV]	$\delta\theta$ [mrad]	δE [MeV/n]
Si 40μm	Spatial reso. Energy reso.	Fragile, thick Expensive	10	488	16	0.003
CATS 5μm - Mylar	Spatial reso. good S/N	Fragile gas	0.7	48	2.14	0.002
MWPPAC 2μm - Mylar	Spatial reso. thin	Fragile gas	0.25	18	1.27	0.001
SED 1.2μm - Mylar	Spatil reso. thin	EF sys. fragile, gas	0.17	12	1.04	0.0008
SED 0.7μm - Mylar	Spatil reso. thin	EF sys. fragile, gas	0.1	7.6	1.98	0.0005

Table 3.1: Different detectors used for tracking with their characteristics and impacts on the beam (^{100}Sn@5MeV/n for the first 4 detectors, and ^{100}Sn@2MeV/n for the last one).

3.2 Secondary electron detection principle

The secondary electron detector is made out of two parts. A thin foil (made of: carbon, Mylar, etc...) is placed on the trajectory of the beam. The particles (beam) passing through the foil cause emission of secondary electrons (e^-) from the foil, also called Emissive Foil (EF). These electrons are further guided to the tracking detector which is positioned outside of the beam trajectory (figure 3.4). This configuration reduces the energy loss and angular straggling of the particles to minimum.
In the specific detection system for S^3 SED, the electrons emitted from the EF are accelerated with an electric ($\overrightarrow{E}$) field and guided by a parallel magnetic ($\overrightarrow{B}$) field toward the detector.
The Lorentz force, $\overrightarrow{F_{tot}} = q\overrightarrow{E} + q(\overrightarrow{v} \times \overrightarrow{B})$, acting on the electron cloud makes the cloud move in a helicoidal trajectory toward the detector.
The electron velocity ($\overrightarrow{v}$) can be decomposed in a component parallel to the electric field ($\overrightarrow{v_\parallel}$) and a component perpendicular to the electric field ($\overrightarrow{v_\perp}$). Considering that the electric and magnetic fields acting on the electrons are parallel to each other, the perpendicular component $\overrightarrow{v_\perp}$ of the electron velocity is constant. This further means that in a non relativistic approach, electrons move in a helicoidal trajectory in the plane perpendicular to the electric and magnetic fields. The periodicity of the trajectory is expressed by the cyclotron frequency (ω) given by:

$$\omega = \frac{qB}{m} \tag{3.13}$$

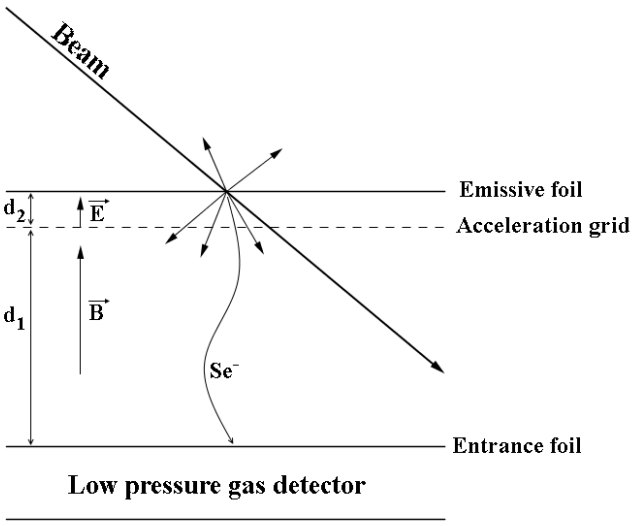

Figure 3.4: Schematic representation of SED.

where q and m are the charge and mass of the electron, while B is the magnetic field acting on the electron. The radius of the curvature (r) then corresponds to:

$$r = \frac{mv_{\perp}}{qB} \tag{3.14}$$

The initial energy of the electron can be written as:

$$E_0 = \frac{1}{2}m(v_{0\parallel}^2 + v_{0\perp}^2) \tag{3.15}$$

The typical initial energy of electrons is low (∼1 eV) compared to the acceleration energy (∼10 keV). Consequently the initial velocity can be neglected and the time the electrons need to reach the detector can be calculated by adjusting the equations from [63] to the specific case of SED:

$$t_d = \sqrt{\frac{md_1^2}{2qV}} + \sqrt{\frac{2md_2^2}{qV}} \tag{3.16}$$

The calculation takes into account that the electrons are accelerated between the EF and the acceleration grid (distance d_2), and just guided between the acceleration grid and the detector (distance d_1). m and q are the mass and charge of the electrons respectively and V is the polarization potential of the EF. It is then possible to calculate the deviation (ρ) from the exit point of the foil to the entrance point of the detector:

$$\rho = \sqrt{2}\frac{mv_{\perp}}{qB}\left(1 - cos\left(\frac{qB}{m}\left(\sqrt{\frac{md_1^2}{2qV}} + \sqrt{\frac{2md_2^2}{qV}}\right)\right)\right)^{1/2} \tag{3.17}$$

The smallest deviation in this case is achieved for:

$$\omega t_d = \frac{qB}{m}\left(\sqrt{\frac{md_1^2}{2qV}} + \sqrt{\frac{2md_2^2}{qV}}\right) = 2n\pi \tag{3.18}$$

The deviation is the smallest when n is an integer number, meaning that the electron needs to make n times an entire turn before reaching the detector. In figure 3.5 results of the calculation performed with equation 3.17 for different strengths of electric fields can be seen.

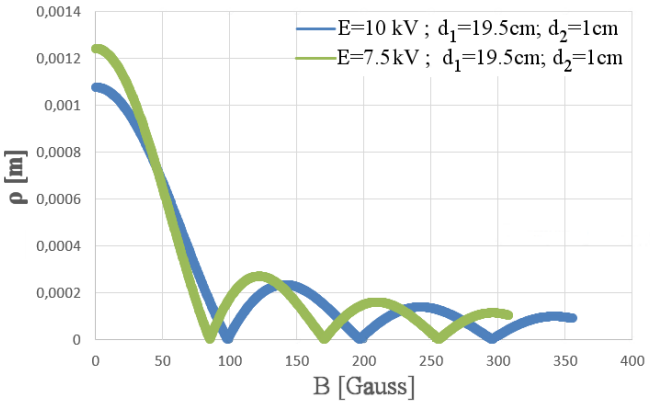

Figure 3.5: Results of a calculation performed using equation 3.17 for electric fields of 10 and 7.5 kV. SED for S^3 was tested between 50 and 110 Gauss (chapter 3.4.1).

3.3 Detector types

This section of the thesis is dedicated to the description of different prototype detectors developed for the purpose of TOF detector at S^3-SIRIUS. The prototype detectors are based on two well known and widely used detector types Multi wire proportional counters and MICROMEGAS. A general description of the working principle of these two types of detectors is given at the beginning of the section in parts 3.3.1 and 3.3.2. This is followed by a technical description of the five different prototypes (3.3.3) tested during the thesis.

3.3.1 Multi wire proportional counters

The first Multi Wire Proportional Counter (MWPC) was introduced by Charpak in 1968 [82]. The basic MWPC was made out of equally spaced anode wires placed between two cathode planes (figure 3.6). Each wire acts as independent counter.

The chamber is filled with gas at atmospheric pressure. Negative constant voltage is applied on the cathodes, while the anode is grounded. Except very close to the anode wires, the electric field lines are essentially parallel and the electric field is almost constant [78], see figure 3.6. If ionization of the gas occurs, the electrons drift following the lines of the electric field (figure 3.6) toward the anode wires. The high electric field in the region around the anode causes an avalanche multiplication of the electrons.
The analytic expression of the electric field in the configuration given above, where the anode is grounded and the cathodes are negatively polarized (V_0), can be expressed as [76]:

$$E(x,y) = \frac{CV_0}{2\varepsilon_0 s}\left(1 + tan^2\frac{\pi x}{s}tanh^2\frac{\pi y}{x}\right)^{\frac{1}{2}}\left(tan^2\frac{\pi x}{s}tanh^2\frac{\pi y}{s}\right)^{-\frac{1}{2}} \tag{3.19}$$

$$V(x,y) = \frac{CV_0}{4\pi\varepsilon_0}\left\{\frac{2\pi L}{s} - ln\left[4\left(sin^2\frac{\pi x}{s} + sinh^2\frac{\pi y}{s}\right)\right]\right\} \tag{3.20}$$

where C is the capacitance per unit length. The typical spatial resolution (localization) of these detectors depends on the spacing of the anode wires. Influence of different geometries, anode wire size and distance between the wires, are discussed in [76]. The time resolution depends on the drift velocity in the particular gas mixture, and it is rather big (several tens of ns) for normal pressure gas detectors [83]. However the normal pressure MWPC can not be used for in beam

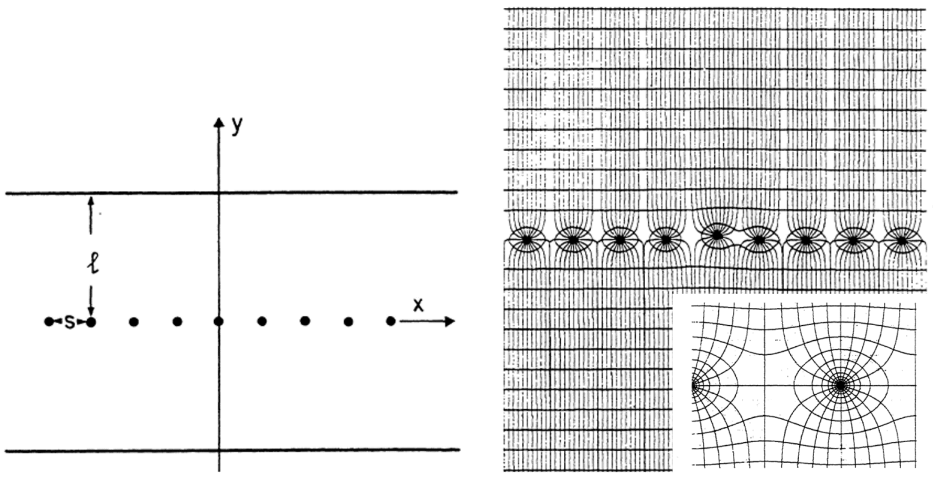

Figure 3.6: Left: Schematic representation of a MWPC configuration. The distance between the anode wires (s) and the anode and cathode (l) are indicated. Right: Electric field line configuration in the MWCP detector. Right down corner: Zoom in the region around the anode wires. Figures adopted from [76].

measurements. Moreover it has to be used in SED configuration as mentioned in section 3.2. The entrance window of the detector has to stay thin enough so the secondary electrons emitted from the EF can pass to the interior of the detector and ionize the gas. For example, electrons with an energy of 10 keV, loose 7 keV in a window made of 0.9 μm thick alyminizied Mylar foil (chapter 3.4). To be able to operate with such thin Mylar foils, the MWPC used in SED configuration operate at low pressures. In this case scenario, the reduced electric field strength in the constant field region increases dramatically (several hundreds of $\frac{V}{cm \cdot mbar}$) [83]. As a result, the avalanche starts already in the drift region.
Several MWPC with different mechanical and technical characteristics were produced and tested since 2008. Three different prototypes of MWPCs will be presented in this thesis.

3.3.2 Micro mesh gaseous structure

MICRO MEsh GAseous Structure (MICROMEGAS) detectors were designed in 1996 [84], aiming to overcome the limitations of the MWPC, such as limitations in the spatial resolution (minimal 0.2 mm) and in counting rates (maximal 10^4 particles/mm^2/s). The detector is made out of an anode and drift electrode

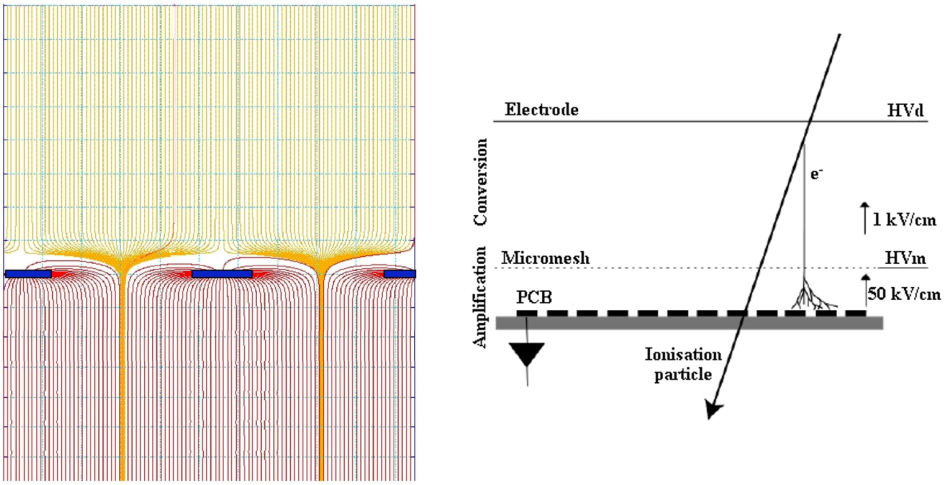

Figure 3.7: Left: Electric field line configuration in MICROMEGAS detector. Right: Schematic representation of the MICROMEGAS detector.

with a micromesh in between. The micromesh is positioned closer to the anode, and divides the space of the detector in two zones. The first zone is called conversion gap [84] and its size is given in mm. The second zone, amplification gap,

placed between the micromesh and the anode is much smaller and it can be as small as 100 μm. The correct set of voltages on the three electrodes allows a really high electric field in the amplification gap and a really low one in the conversion gap. The drift field is achieved by applying negative voltage on the micromesh and a slightly higher negative voltage on the drift electrode. The drift electrode can be replaced with a window made of thin aluminized Mylar foil for example.
Energy deposition of the incident particle in the conversion region ionizes the gas inside the gap. The created electrons drift towards the micromesh and create an avalanche in the amplification gap. They are then fastly collected on the anode. The created ions are accelerated in the opposite direction and are collected on the micromesh.
The operation of MICROMEGAS changes in low gas pressure configuration. At normal pressures the avalanche is made in the amplification gap. However due to the high reduced electric field (∼200 V/cm/mbar) at low pressures, the amplification starts in the drift gap almost at the entrance window. The mean free path (∼100 μm) of electrons is high at low pressures which means that the amplification gap commonly used (∼100 μm) is too small to achieve good amplification. In [85], two solutions to this issue are suggested. The first one is to keep the amplification gap small but do preamplification in the drift gap, and the second one is to increase the size of the amplification gap. MICROMEGAS have been tested in SED configuration with several amplification gaps in the S^3 study framework [86]. During this thesis one MICROMEGAS detector with an increased amplification gap (256 μm) was tested.

3.3.3 SED prototypes

A technical description of five different prototypes tested during this thesis is given in this section. Four prototypes are based on MWPC (miniSED1D 3.3.3, miniSED2D 3.3.3, miniSEDSP 3.3.3, rsSED 3.3.3) and one prototype is based on MICROMEGAS (micromegas prototype 3.3.3) detector.

MiniSED1D

The first detector which was tested is called miniSED1D. It is a low pressure MWPC which permits 2D position and time measurements. A schematic representation of the detector can be seen in figure 3.8. It has an active area of 70x70 mm^2. The thickness of the detector is 4.2 mm and it can be divided in two parts. A dead zone of 1 mm between the entrance window and the wire cathode, and the active zone of 3.2 mm between the two cathodes. The entrance window is made of 0.9 μm aluminized Mylar foil reinforced by a metal mesh of 83 % transparency. The role of the metal mesh is to reinforce the window and

prevent it from deforming due to the pressure difference between the interior and the exterior of the detector. This configuration of the entrance window is used for all prototypes (MWPC and MICROMEGAS) which will be described here. The horizontal (X) position is retrieved by a wire plane cathode positioned 1 mm from the entrance window and 1.6 mm from the wired anode, perpendicular to it. This cathode is made of 28 gold coated tungsten wires of 50 μm diameter soldered every 1 mm and linked by three. The vertical (Y) position information is retrieved from the second cathode. This cathode is a Printed Circuit Board (PCB) with 28 1D strips of 2.54 mm pitch separated by 100 μm. The anode is made out of 72 gold coated tungsten wires of 20 μm diameter. The space between two consecutive wires is 1 mm. The anode is placed in between the two cathodes at a distance of 1.6 mm from each of them. The pressure of the gas inside the detector can be regulated and varied from 4 to 10 mbar. This detector is smaller but it has the same configuration as the former VAMOS SED [75].

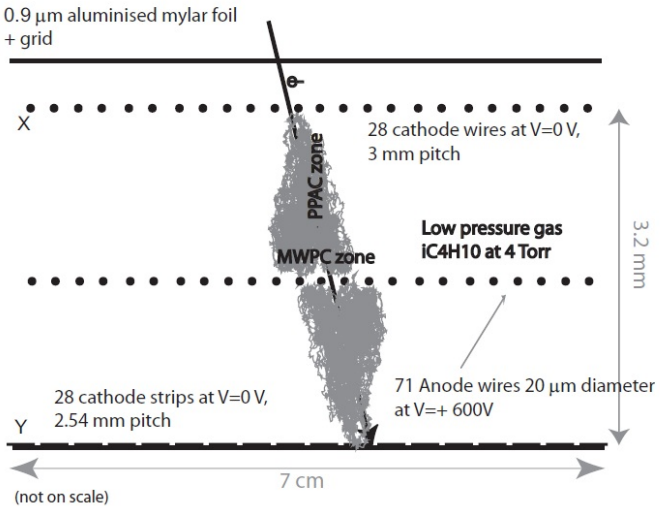

Figure 3.8: Schematic drawing of the miniSED1D prototype.

MiniSED2D

The second detector is called miniSED2D. It is again a MWPC working in low gas regime, permitting 2D position and time measurement. A schematic representation of the detector can be found in figure 3.9.
The active surface of the detector is 70x70 mm^2, with a thickness of 3.2 mm. The entrance window is made of a 0.9 μm thick, alyminized Mylar foil as described in previous section. A 2D PCB is used as a cathode and it retrieves both vertical (Y) and horizontal (X) positions. The cathode contains 28 X and 28 Y strips with a

pitch of 2.54 mm in both directions. The separation between two consecutive strips is 0.2 mm (figure 3.10). This type of cathode was further used for all other SED MWPC prototypes. The cathode is placed at 3.2 mm distance from the entrance window. The dead zone, present in the miniSED1D, is removed by the fact that the entrance window acts as a drift electrode for this prototype. The anode has a same configuration and position as for miniSED1D.

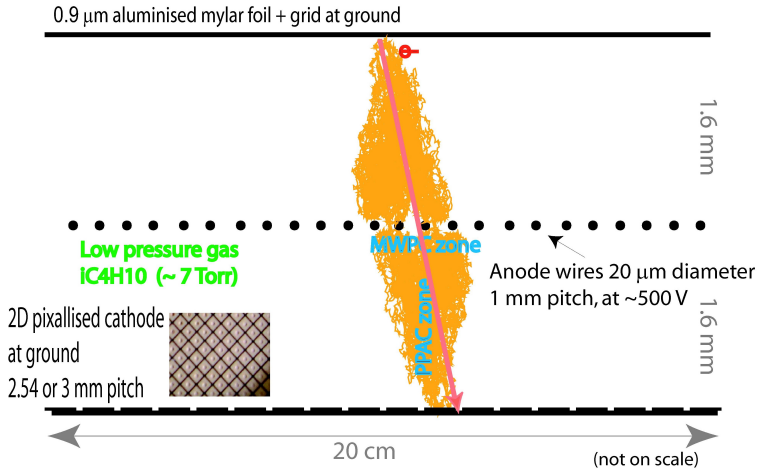

Figure 3.9: Schematic drawing of the miniSED2D prototype. The zoom of the 2D pixellated cathode can be seen in the lower left corner.

MiniSEDSP

MiniSEDSP is a MWPC working in low pressure gas regime, permitting 2D position and time measurement. The mechanical characteristics of this detector are the same as for the miniSED2D except for the size of the strip pitch of the cathode, which is in this case 1.54 mm. Otherwise, it has an active surface of 70x70 mm^2 and a thickness of 3.2 mm. The drift electrode is the entrance window made of alyminized Mylar foil. The wired anode is placed at the middle of the detector.

Real size SED

The Real Size (rsSED) prototype which was built is in principle a bigger version of the miniSED2D prototype. It has an active surface of 200x120 mm^2. The pixellated cathode is made of 67 X and 47 Y strips with 3 mm pitch in both directions. The separation between two consecutive strips is 0.2 mm. The wired anode is positioned at the middle of the detector. However it is split in two for capacitance reduction. The entrance window is additionally reinforced with a

strong back (figure 3.10) to insure gap thickness homogeneity. The transparency of the strong back is 92.5%.

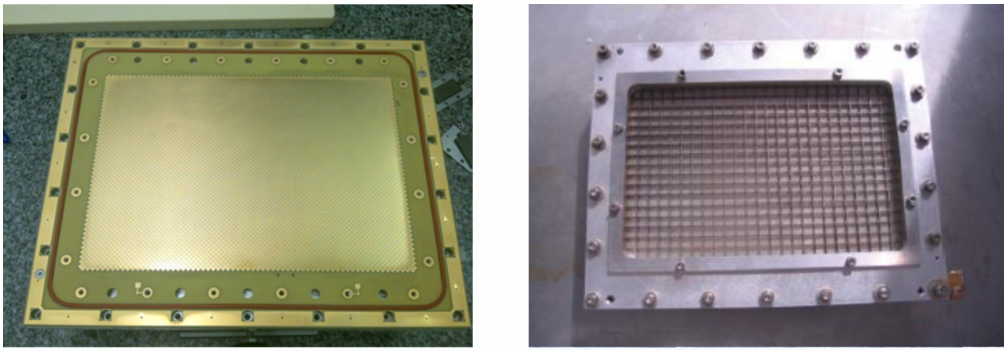

Figure 3.10: Left: Picture of the 2D PCB used as a cathode in miniSED2D and rsSED. Right: Picture of the entrance window with the strong back used for rsSED.

MICROMEGAS prototype

The MICROMEGAS detector has an active area of 70x70 mm^2 with a thickness of 2.4 mm (figure 3.11). The entrance window as described in 3.3.1 is used as a drift electrode. The drift gap is 2.2 mm thick, while the amplification gap has a thickness of ∼256 μm. Spatial information is retrieved with a 2D PCB made out of 28 X and 28 Y strips with 2.54 mm pitch in both directions. The cathode has the same construction as the cathode for miniSED2D and rsSED. The detector is produced in a bulk process [87] unlike the first MICROMEGAS prototype described in [86]. For the first prototype, the 30 μm thick micromesh grid was positioned on top of the pillars separating it from the cathode. For this prototype, the anode and the micromesh grid are produced in one piece in the bulk process.

3.4 Measurement of the detector performances

SED detectors are used as TOF detectors, meaning that they are tracking the passing beam, retrieving the time and the interaction position of the beam in the detector. Consequently they need to have good spatial and time resolution.
Up to now, the detector tests were done in a laboratory in a vacuum chamber with a californium (^{252}Cf) source. Low pressure gas detectors are made to work under vacuum. Additionally the beam line of S^3 where the detector will be positioned will be at 10^{-7} mbar. Thus all tests were performed in vacuum with a pressure between 10^{-5} and 10^{-6} mbar. The ^{252}Cf source was chosen to perform these tests because it emits Fission Fragments (FF). There are two reasons for using FF

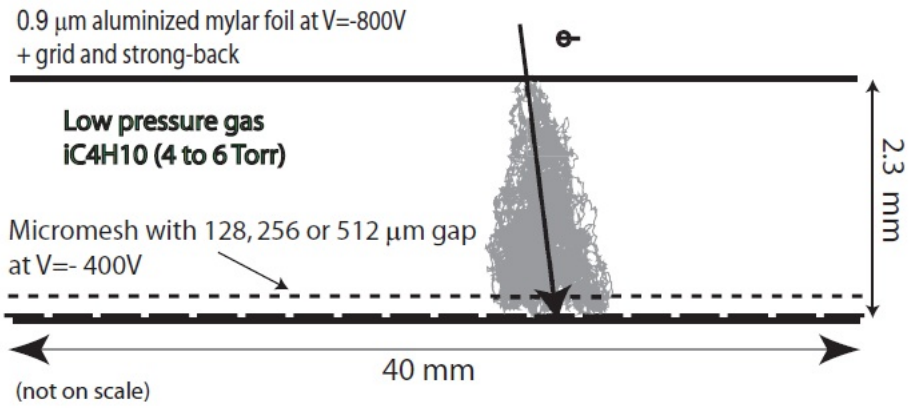

Figure 3.11: Schematic representation of a MICROMEGAS prototype.

source for the tests. First off all the detector will be used at S^3 for SHE study, this means that the particles which need to be tracked will be medium and heavy mass nuclei. On the other hand the source is strong enough to cause emission of a significant amount of secondary electrons from the EF which enables better and faster characterization of the prototypes. The prototypes were tested and are triggering on the α particles as well. In beam tests are expected in the future.
The results of different tests performed on previously described detector prototypes are given and discussed in the following sections.

3.4.1 Spatial resolution measurements

Experimental setup

A collimated ^{252}Cf source is placed in front of the EF as close as possible. It is mounted on a remote controlled 1D motor. The motor can be moved in horizontal but not in vertical direction. The EF is made out of 0.9 μm thick alyminized Mylar foil. It is inclined by 45^o compared to the source and polarized to -10 kV. An acceleration grid is positioned parallel to the EF at a distance of 10 mm. The grid is grounded and made out of gold-coated tungsten wires of 50 μm diameter separated by 1.5 mm. This configuration accelerates the secondary electrons emitted from the EF up to 10 keV. Two magnetic coils positioned as indicated in the figure 3.12 produce a magnetic field parallel to the electric field. The magnetic field focalizes and guides the electron cloud to the SED. The optimal configuration of the fields was studied and will be described later in this chapter. The SED is positioned parallel to the EF at a distance of 200 mm in forward (upstream) direction in

order to prevent the FF to reach the detector. The detector is filled with pure isobutane (iC_4H_{10}) at a pressure of 7 mbar. Different gases and pressures were tested and will be discussed later in the chapter. The signal from the cathode of the detector is read by an AFTER (ASIC For TPC Electronic Readout) card. This electronics was previously developed for T2K (Tokai-to-Kamioka) experiment [88]. The AFTER card is equipped with one preamplifier and one shaping amplifier per channel. The signals are sampled at a rate of 100 MHz and registered in a 12 bit ADC on trigger request. Parallel to the source in forward direction, a small silicon (Si) detector is placed. The Si detector is used as a trigger in coincidence with the SED and registers the FF coming from the source.

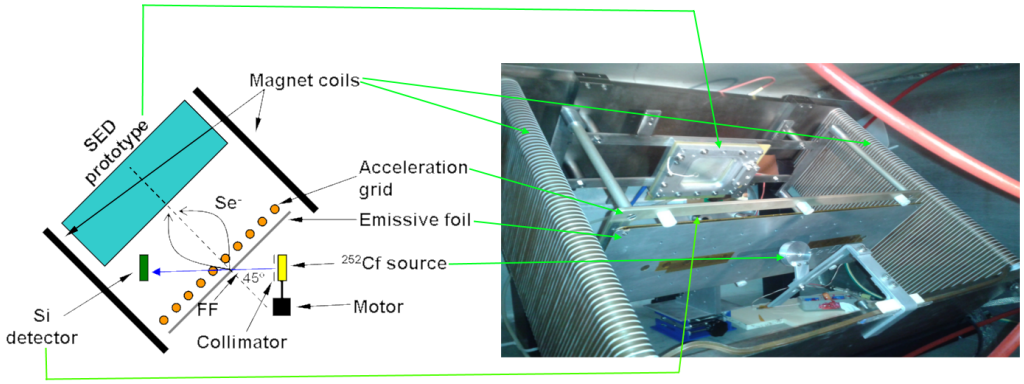

Figure 3.12: Left: Schematic representation of the off line experimental setup for the spatial resolution measurements. Right: Picture of the setup. The tests were being made with a collimator on the EF and without the motor at that moment. Acceleration grid+SED parallel to EF, acceleration grid-EF = 10 mm, SED-EF = 200 mm, Si+Source 45^0 compared to EF, Source+collimator-EF < 1 mm, Si-EF = 10 cm, two magnetic coils = 50 cm.

The spatial resolution of the detector can be calculated in several ways. Generally the centroid finding algorithms can be separated in two classes [89]:

- The algorithms which calculate the geometrical center of gravity of the measured charges of a predetermined number of strips. In this case the position (X_n) is given by:

$$X_n = \frac{\Sigma_{i=1}^{n} x_i Q_i}{\Sigma_{i=1}^{n} Q_i} \tag{3.21}$$

  where the x_i is the position of the center of the i^{th} strip, and Q_i is the charge of the i^{th} strip.

- The algorithms which approximate the observed charge distribution with analytical functions which parameters are the position of the centroid, the width and the height of the distribution. Frequently used functions are Gaussians, Lorenzians or squared secant hyperbolics (*Sechs*).

The spatial resolution for SED detectors (this case) is calculated using a charge centroid reconstruction method.
The projection of the source through the collimator system on the EF is an ellipse with parameter $\boldsymbol{a}$ in horizontal (X) direction and parameter $b = \sqrt{2}a$ in vertical (Y) direction. The function used to fit the charge distribution in order to retrieve the spatial resolution in X and Y direction is a convolution of a Gaussian:

$$g(x;\mu,\sigma) = \frac{A}{\sqrt{2\pi}\sigma} e^{-\frac{(x-\mu)^2}{2\sigma^2}} \tag{3.22}$$

and an ellipse:

$$\frac{x^2}{a^2} + \frac{y^2}{b^2} = 1 \tag{3.23}$$

which gives for X direction:

$$X(y;A,a,\sigma,\mu) = \frac{Aa}{\sqrt{2\pi}\sigma} \int_{y-\sqrt{2}a-\mu}^{y+\sqrt{2}a+\mu} \sqrt{1 - \frac{(t-y+\mu)^2}{2a^2}} e^{\frac{t^2}{2\sigma^2}} dt \tag{3.24}$$

and for Y direction:

$$Y(x;A,a,\sigma,\mu) = \frac{Aa}{\sqrt{\pi}\sigma} \int_{x-a-\mu}^{x+a-\mu} \sqrt{1 - \frac{(t-x+\mu)^2}{a^2}} e^{\frac{t^2}{2\sigma^2}} dt \tag{3.25}$$

where A is the amplitude of the signal, a is the radius of the collimator, σ is the resolution of the detector and μ is the center of the hole of the collimator. In order to solve the integration numerically and retrieve the spatial resolution of the detector, Simpson's 3/8 rule [90] was used:

$$\begin{aligned} \int_k^l f(x)dx &\approx \frac{3h}{8}\left[f(k) + 3f\left(\frac{2k+l}{3}\right) + 3f\left(\frac{k+2l}{3}\right) + f(l)\right] \\ &= \frac{l-k}{8}\left[f(k) + 3f\left(\frac{2k+l}{3}\right) + 3f\left(\frac{k+2l}{3}\right) + f(l)\right] \end{aligned} \tag{3.26}$$

Figure 3.13 shows, on the left (right), the plot of the numerically solved equations 3.24 (3.25). These functions (with proper parameters) were used to fit the experimental data and retrieve the spatial resolution of the detector.

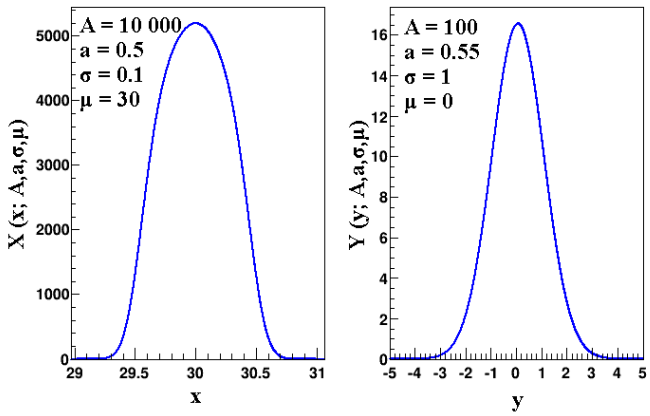

Figure 3.13: Left (Right): Plot of the functions in X (Y) direction used to retrieve the spatial resolution of the SED detectors. The functions are plotted with different input parameters indicated in the figures.

Optimization of the fields

The prototype detector miniSED1D was used to determine the optimal configuration of the electric and magnetic fields. The detector was filled with pure isobutane (iC_4H_{10}) at 6.5 mbar, and polarized to 500 V (sparking limit of the detector). It was placed in vacuum at 10^{-6} mbar. The influence of the magnetic field ($\overrightarrow{B}$) on the spatial resolution of the miniSED1D detector can be seen in figure 3.14. These results were compared with the ones obtained with miniSED2D (pink dot), MICROMEGAS (green inverted triangles) and with the calculation (blue triangles). The calculation was performed using the equation 3.17, where the accelerating voltage was set to 10 kV and the distance between the EF and Se^-D is 200 mm (10 mm (d_2) + 190 mm (d_1)), corresponding to our set up.
A significant degradation of the spatial resolution can be observed in the absence of the magnetic field (figure 3.14). Such a result is not surprising since the electron cloud is wider in the absence of the magnetic field. Moreover, as can be seen in equation 3.17, the deviation between the emission point on the EF and the entrance point in the detector is proportional to the perpendicular component of the velocity ($v_\perp$). In the X, Y referential frame, $v_\perp$ in bigger in Y than in X since the secondary electron initial velocities are enhanced in the direction of the incoming ions. Consequently, the resolution of the detector is more degraded and the effect is more pronounced in the Y direction.
Figure 3.14 indicates that for a voltage of 10 kV on the EF, the optimal magnetic field is placed in between 80 and 110 Gauss (corresponds to 50 and 70 A on the coils). The influence of the electric field on the resolution was tested for these

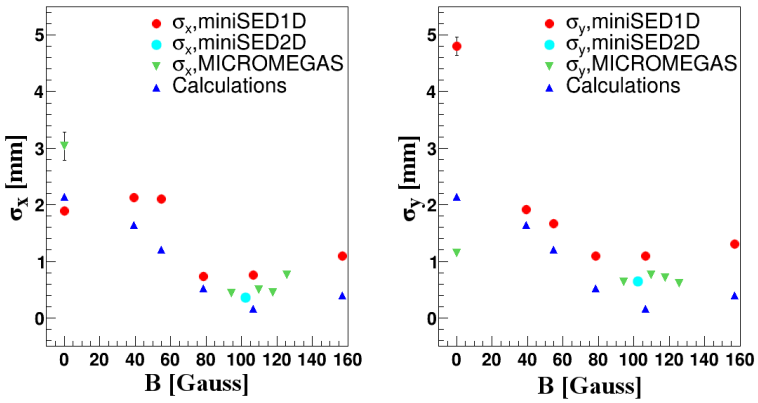

Figure 3.14: Left (Right): Spatial resolution in X (Y) direction versus the magnetic field ($\vec{B}$). The red (light blue) dots present the results for miniSED1D (miniSED2D) prototype, the green inverted triangles are results obtained with the MICROMEGAS detector and the blue triangles are the result of a calculation performed according to the equation 3.17. The applied electric field is 10 kV for the measurements and the calculation. Error bars are smaller than the size of the symbol.

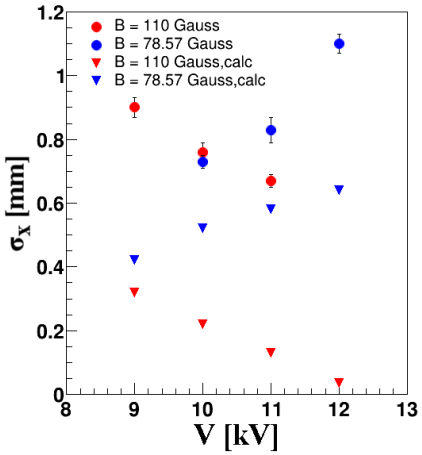

Figure 3.15: Spatial resolution in X direction versus the accelerating voltage (V). The measurements were performed for two different settings of the magnetic field 80 Gauss (blue dots) and for 110 Gauss (red dots). The red (blue) triangles present calculations performed using equation 3.17 for a magnetic field of 110 (80) Gauss.

values of the magnetic field. However the strength of the electric field which can be applied on the EF depends on the mechanical resistance of the foil, meaning that if the field is too high, the foil will break. The results of the test can be seen in figure 3.15. Both measurements follow the trend observed in the results obtained by the calculation performed using the equation 3.17. An improvement in the resolution can be noted for a magnetic field of 110 Gauss by increasing the polarization on the EF. However a completely opposite behavior is observed for the lower magnetic field of ∼79 Gauss. It has to be mentioned that the calculation performed using the equation 3.17 does not give the spatial resolution of the detector but the deviation between the exit point of the EF and the entrance point in the detector. The wider the distribution of the electron cloud on the detector is, the worst is the spatial resolution. Consequently the results of the calculation and the measured resolution can not give the same values, but the general behavior can be compared between the calculation and the measurements. By taking a closer look at figure 3.15, it can be noted that the general trend for the two is the same, while the values show a difference. Finally a configuration with 110 Gauss (70 A) magnetic field and a voltage of 10 kV was applied for further measurements.

Surface homogeneity studies

A series of measurements on 4 prototype detectors (miniSED2D, rsSED, miniSEDSP and MICROMEGAS) were conducted to study the homogeneity of the spatial resolution over the surface of these detectors. This was achieved by moving the source with a step of 200 μm over an interval of 1.5, 2.5 or 3 mm, which is the distance corresponding to the pitch of the pad plane. The test was done in one direction (X) since the motor used is moving just in horizontal plane. Figure 3.16 shows the behavior of the spatial resolution over the surface of a detector for a distance corresponding to the pitch of a specific detector. It can be noted that all 4 prototypes, miniSEDSP (green dots), MICROMEGAS (pink inverted triangles), miniSED2D (red dots) and rsSED (blue triangles) show oscillation of the spatial resolution over the distance. The figures on the right show the movement of the centroid in dependance of the source position. It allows to follow the impact position of the electron cloud in the SED. The spatial resolution is calculated by the centroid method using the 9 central strips around the one which collected the maximum charge (the mean multiplicity is around 15 for a 3 mm pitch). The calculation depends on the charge resolution of the strips from which the centroid is reconstructed. If the electron cloud hits the middle of one strip, charge deposited in the strip will be maximal giving a good charge resolution and consequently a good spatial resolution. However if the electron cloud hits the inter-strip, space in between two strips, the charge is split between the two neighboring strips, degrading the charge and the spatial resolution of the detector. The difference between

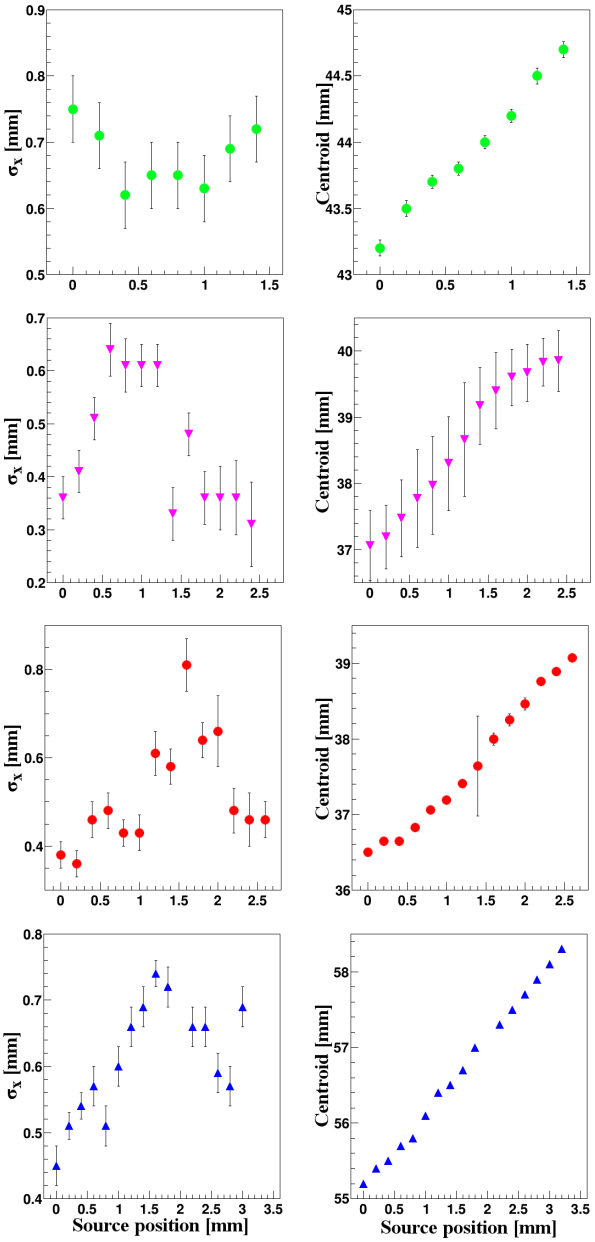

Figure 3.16: Left (Right): Dependence of the horizontal spatial resolution (centroid) from the position of the source for (from top to bottom) miniSEDSP, MICROMEGAS, miniSED2D and rsSED respectively.

the two extreme values of the resolution can be quite big, resulting in up to twice bigger value for the inter-strip position.
However, to a certain extent, the spatial resolution does not depend on the size of the strip pitch. For example the resolution of the small pitch detector (miniSEDSP) is the same as the resolution of the 3 mm pitch detector. The reason is similar to the one explaining the oscillation of the resolution depending on the strip/inter-strip position. The size of the strip influences the amount of charge collected, so the smaller the strip is, the less charge is collected, and the charge resolution is more degraded. Consequently, the size of the strip pitch is limited on both ends, limiting the number of electronics channels as well. Figure 3.17 shows the behav-

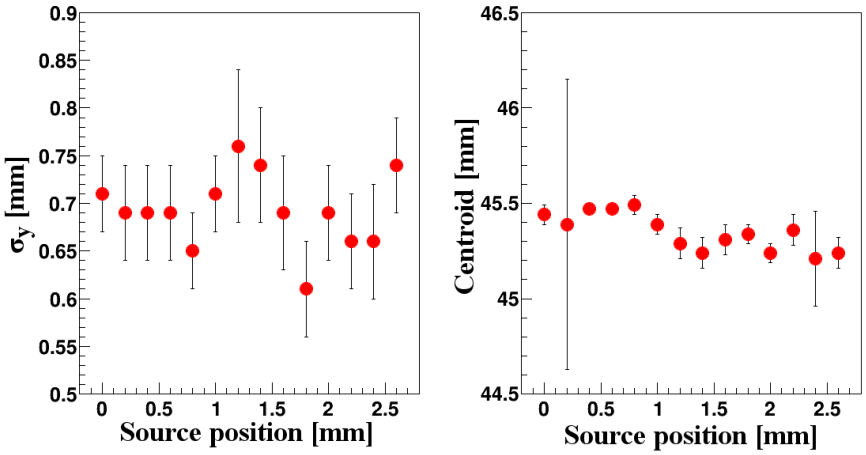

Figure 3.17: Left (Right): Dependance of the vertical spatial resolution (centroid) from the position of the source for miniSED2D prototype.

ior of the spatial resolution in Y direction for the miniSED2D. Since the vertical position is not variable, it was expected that the resolution in Y stays stable. This behavior can be seen for all 4 prototypes. Additionally the position of the centroid, right figure, does not change, which confirms the stability of the resolution. However it is not clear if the position in which the vertical resolution was measured belongs to strip or inter-strip location. As a consequence, one needs to be careful when comparing the resolution of different detectors in the X direction.

3.4.2 Time resolution measurements

Experimental setup

Currently the experimental setup for the spatial and time resolution measurements of the SED prototypes is slightly different. However, the final setup will be the same, and time and spatial resolution could be measured at the same time.

Time resolution of these detectors is very important (chapter 2.4). Generally, a ^{252}Cf source is used for the off line measurements. The source is placed with an angle of 45^o compared to a square EF (70x70 mm^2) polarized to -10 kV. The foil is a 0.9 μm thick aluminized Mylar foil. On each of its side, of it a grounded extraction (acceleration) grid is placed. As in previous setup, the electric field ($\overrightarrow{E}$) formed between the EF and the grid serves for extraction of the secondary electrons from the EF and their acceleration towards the detector. A SED prototype is mounted parallel to the foil in forward direction. The time signal from the anode is read out by a fast amplifier. The amplifier has a rise time <2 ns and a gain of 200. A plastic scintillator, with very good time resolution (below 30 ps σ), is placed in backward direction parallel to the EF. A silicon detector, used as a trigger, is mounted in forward direction parallel to the source (section 3.4.1). The silicon detector in coincidence with the SED is set to trigger the acquisition with FF coming from the source [86]. A MATACQ card [91] was employed to register the signals from each

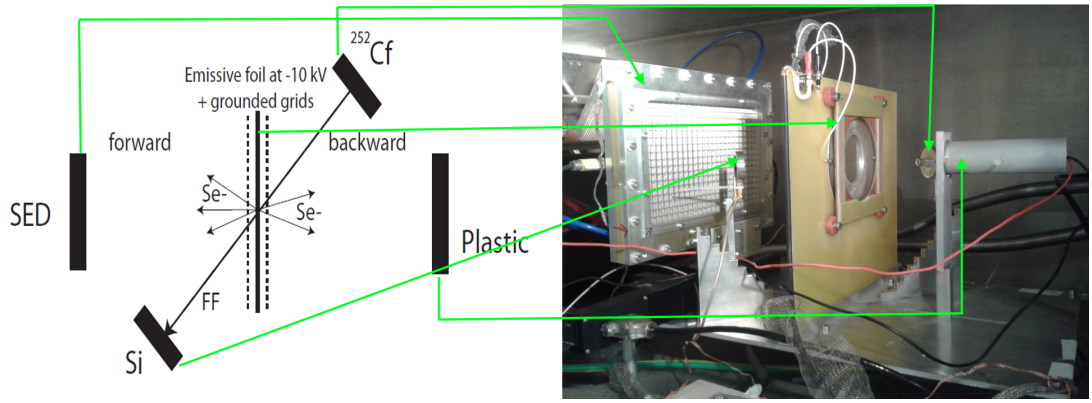

Figure 3.18: Left: Schematic representation of the off line experimental setup for time resolution measurements. Right: Picture of the setup. The detector visible is the rsSED prototype. SED+EF+Plastics parallel to EF. SED-EF=20 cm, Plastic-EF=10 cm, Cf (Si)-EF=10 cm under 45^0.

detector. An offline software CFD (Constant Fraction Discriminator) was applied to get the start time of the detectors. Since the time resolution of the plastic scintillator is a couple of tens of ps, the width of the time difference distribution between the scintillator and the SED gives mainly the time resolution of the SED prototype.
Several studies were conducted to test the time response of the prototypes. They will be described in the following paragraphs.

Optimization of the gas type and pressure

Tetrafluoromethane (CF_4) and isobutane (iC_4H_{10}) were used to investigate the response of rsSED time resolution as a function of pressure. These gases were chosen for their high quenching power, low ionization energy (23 eV) for iC_4H_{10} and high drift electron velocity in the case of CF_4. The voltage of the detector was adjusted at the sparking limit for each pressure. Figure 3.19 shows the behavior of the amplitude and the rise time of the detector for different pressures. It can be seen that the amplitude response was increasing with the pressure while the rise time was nearly constant, except for 3 mbar in iC_4H_{10}. The behavior of the time resolution with respect to the pressure and the amplitude can be seen in figure 3.20. It can be noted that the resolution shows the same trend in both gases. This was to be expected considering that the amplitude has an almost linear dependance on the pressure. The time resolution displays a minimum at the pressure of 9 mbar in iC_4H_{10}. This was not tested for CF_4 due to the fact that higher pressures are needed and the entrance window of the detector could not sustain this. Additionally it is clear that the time resolution is better in pure iC_4H_{10} compared to pure CF_4.

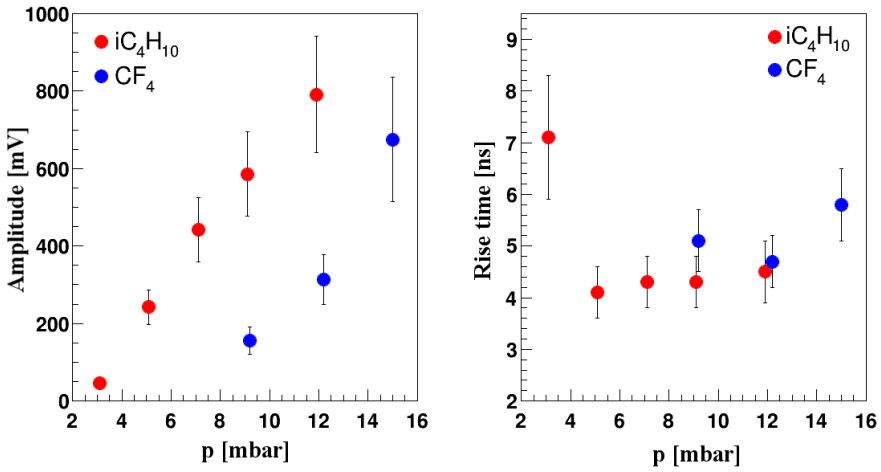

Figure 3.19: Left (Right): Dependance of the amplitude (rise time) on the pressure in the detector. Red dots are results obtained using iC_4H_{10}, while blue dots present the results obtained in CF_4.

The same amplitude response for both gases can be reached by increasing the pressure values for CF_4 compared to the ones in iC_4H_{10}. The bad time resolution at low pressure of 3 mbar can be explained with a low signal to noise ration ($\sim$20). In order to study the influence of the noise (sigma of the baseline $\sim$1 mV) on the time resolution , the ratio of the noise to the derivative of the signal (at 30%) has

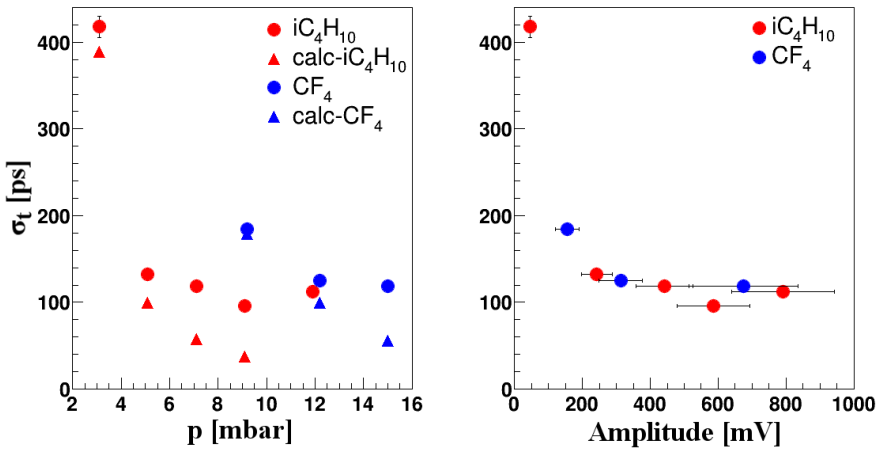

Figure 3.20: Left (Right): Time resolution dependance on the pressure (amplitude). The red dots present results obtained using iC_4H_{10}, while the blue dots are results obtained in CF_4. The triangles red and blue present the calculation for iC_4H_{10} and CF_4 respectively.

been calculated and plotted in the form of triangles in figure 3.20. It was observed that these values decrease while improving the SNR from ∼20 at 3 mbar to ∼220 at 12 mbar. The best achievable time resolution in this configuration of noise and detector response is given by the calculated values presented in figure 3.20. The measured values are bigger due to various factors: internal process of ionization, drift and amplification in gaseous detector, time resolution of the plastic photomultiplier, the EF system and the electronics.
All following time resolution measurements were done with pure iC_4H_{10} at pressure of 7 mbar. The detector is polarized at the sparking limit.

Surface homogeneity studies for rsSED prototype

The time information is retrieved from the anode. Recalling section 3.3, the anode of the rsSED is separated in two due to capacitance issues. Consequently a study was performed to investigate the influence of the two anodes on the time resolution of the detector depending on the position. The rsSED was mounted on the motor, which was moved with a step of 100 μm over a surface of 100 mm around the middle of the anode. The surface of the detector which was studied was covering the region from the middle of one anode over the middle of the detector (place where the two anodes meet) to the middle of the other anode, this distance corresponds to 100 mm. The impact of the interaction between the two anodes on the time resolution as well as on the amplitude of the signal can be seen in figure 3.21. It is clear that the time resolution is degrading around the middle of the detector,

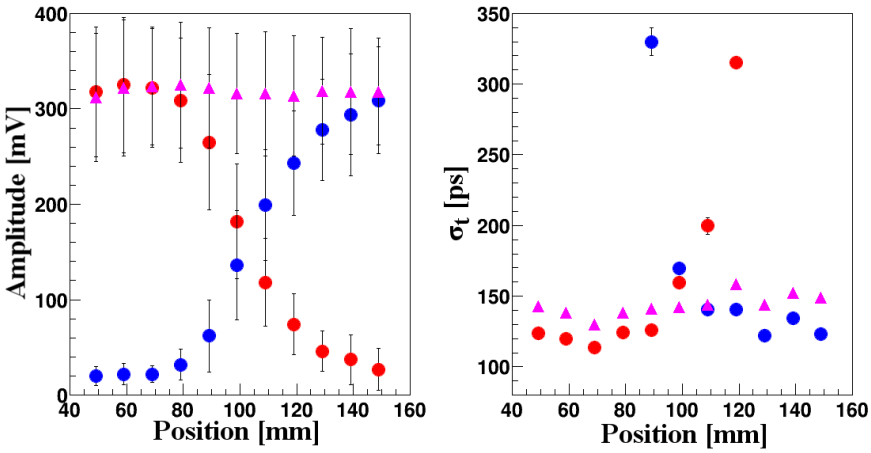

Figure 3.21: Left (Right): Oscillation of the amplitude (time resolution) over the surface of the detector. Red dots present the signal from anode 1, blue dots signal from anode 2, and pink triangles the reconstructed signal.

at the cut between the two anodes. The amplitude of the signal is also degrading at this position, which is in agreement with previously observed behavior of the detector. To overcome the resolution degradation, a simple reconstruction is done in the analysis program using:

$$Amp_t = Amp_1 + Amp_2 \tag{3.27}$$

where Amp_t is the reconstructed amplitude of the signal, Amp_1 and Amp_2 are the amplitudes of the signal for the respective anodes at a specific position. The reconstructed signal amplitude was used in the analysis program to obtain the value of the time resolution.
The results of the reconstruction are shown in figure 3.21 as pink triangles. The time resolution calculated in this way shows a homogeneous behavior over the surface of the detector. However it is a bit degraded compared to the resolution obtained at the middle of each of the anodes when the reconstruction is not used. Additionally a series of tests was conducted to see if the time resolution of the detector is stable at the edges (end) of the anodes.
Figure 3.22 shows the behavior of the time resolution over the complete surface of the real size detector in dependance on the anode. It can be noted that the time resolution suffers degradation at the edges of the anodes, which can be seen at the end of the detector (0 mm and 200 mm) as well as in the middle, where the resolution is additionally influenced by the interference between the two anodes. However this effect can be overcome with the time reconstruction as described previously in this section. On the other hand a different solution has to be found

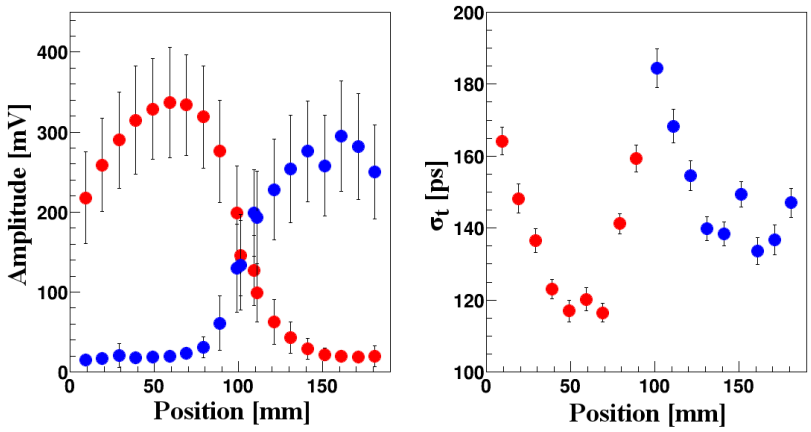

Figure 3.22: Left (Right): Oscillation of the amplitude (time resolution) over the surface of the detector. Red dots present data gathered from anode 1 and blue dots data gathered with anode 2.

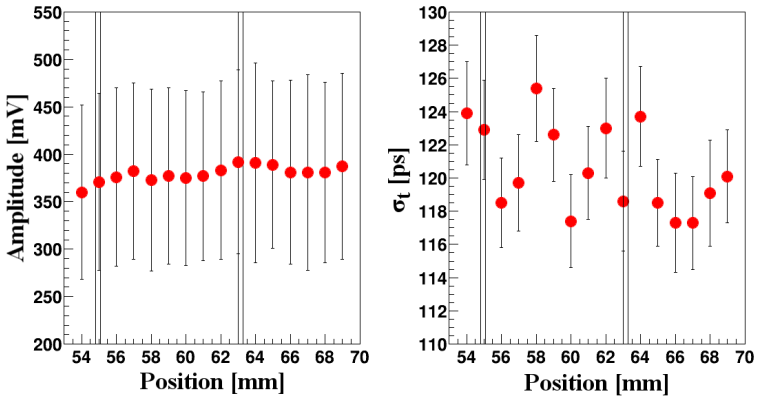

Figure 3.23: Left (Right): Behavior of the amplitude (time resolution) over 6 mm of the detector surface. The widths and the position of the strong back is indicated in the figures as two vertical solid lines.

for the edges of the detector.
Finally, the influence of the strong back on the time resolution has been investigated. The results of the study indicate that the strong back does not influence the time resolution of the rsSED prototype (figure 3.23).

3.4.3 Counting rate capabilities: in-beam measurements

The study of the dependance of the time resolution on the counting rate was performed at GANIL in an in-beam measurement using CIME (Cyclotron pour Ions de Moyenne Energie). Even though I have not participated in this measurement, the obtained results are important and will be discussed briefly in this section. The status of the in-beam measurements was obtained from [92–94].
The time resolution was tested for 4 different prototypes: miniSED1D, two 2D wire chambers and a 1D MICROMEGAS detector with a small amplification gap (128 μm). All 4 prototypes have shown good properties with a minimal time reso-

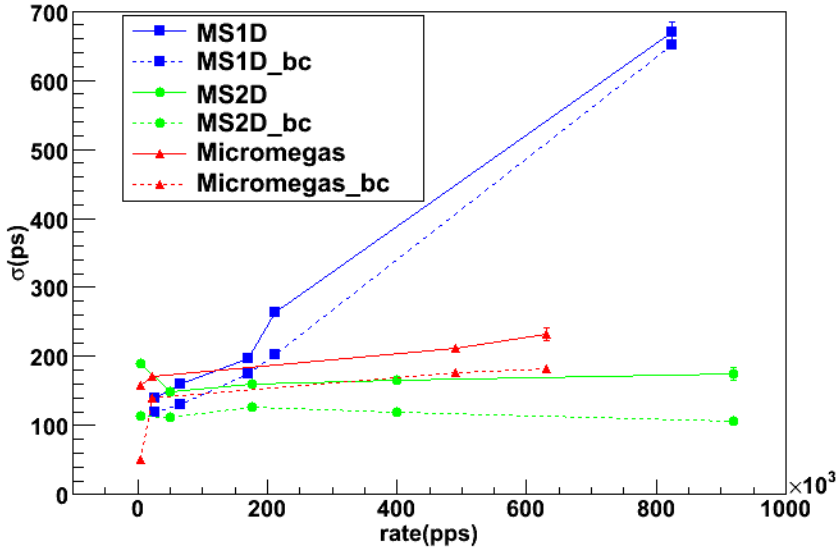

Figure 3.24: Time resolution (σ) obtained for each detector versus the counting rate with and without beam correction (bc) [93].

lution of 120 (10) ps for the wire chambers and 140 (15) ps for the MICROMEGAS. However, the performances are not equivalent from one detector to another at high counting rates.
A beam correction was performed estimating the influence of the shape of the beam and the 45^0 angle of the EF on the time resolution of the detector [95]. The time resolution, with and without the beam correction, in dependance of the

counting rate, is plotted in figure 3.24.
The miniSED1D prototype (blue) shows a significant degradation in the resolution with high counting rates (figure 3.24). The high counting rate imposes the decrease of the voltage in the detector which further degrades the time resolution. The cause of the time resolution degradation is probably the dead layer at the entrance of this detector (section 3.3.3).
The time resolution of the miniSED2D and MICROMEGAS prototypes was slightly degraded as can be seen in figure 3.24). Nevertheless they presented good performances with a stable sparking voltage and counting rates up to $5{\cdot}10^5$ pps.
It was concluded that the most adequate solution would be to improve the performances of the 2D wire chambers. The real size SED (rsSED) prototype tested in this work is a 2D wire chamber.

3.5 Conclusions and perspectives

A new tracking detector based on SED principle is developed at GANIL to be installed at the final focal plane of S^3, SPIRAL2 facility. This detector has to fulfill the standards set by S^3 and the physics community which will use it. The detector should have minimal interaction with the fusion-evaporation products which are tracked. Additionally it should have a spatial resolution below 1 mm FWHM and a time resolution of 150 ps FWHM. Finally, the size of the detector has to cover the large (200x120 mm^2) final focal plane of S^3.
Several detector prototypes, including one prototype of the full size, were produced since 2008 and tested. This work covers tests on five different prototypes. The optimal configuration of the combination of the electric and magnetic fields (section 3.4.1) including the gas type and pressure (section 3.4.2) inside the detector were determined. The configuration was set to a voltage of 10 kV applied on the emissive foil with a magnetic field of 110 Gauss (70 A). The detector is filled with pure isobutane (iC_4H_{10}) at a pressure of 7 mbar.
The homogeneity of the spatial (section 3.4.1.) and time resolution (section 3.4.2.) and the influence of the strong back (section 3.4.2.) were studied for each detector prototype in the horizontal direction [93]. All tested prototypes show an oscillation of the spatial resolution values depending on the position inside the detector. It was shown (section 3.4.1) that the best resolution was obtained when the electron cloud hits the middle of a strip, while the worst one is obtained when the cloud hits the inter-strip position. The difference between the two can be up to two times higher resolution in the inter-strip position (table 3.2). The spatial resolution of different prototypes can not be really compared for the moment due to the fact that the exact position in the vertical plane was not known. Comparison of the spatial resolution of the miniSEDSP with the rest of the prototypes confirmed that

	Spatial resolution		Time resolution	
Prototype	σ_{x_s} [mm]	$\sigma_{x_{is}}$ [mm]	$\sigma_{t_{min}}$ [ps]	$\sigma_{t_{max}}$ [ps]
miniSED2D	0.36 (0.03)	0.81 (0.06)	NM	NM
miniSEDSP	0.63 (0.05)	0.75 (0.05)	NM	NM
rsSED	0.45 (0.03)	0.74 (0.03)	130 (3)	159 (4)
MICROMEGAS	0.36 (0.04)	0.64 (0.05)	NM	NM

Table 3.2: Summarized results for the spatial and time characterization of different detector prototypes. σ_{x_s} gives the spatial resolution in the strip position, while $\sigma_{x_{is}}$ in the inter-strip position. Minimal and maximal values of time resolution are given for the reconstructed amplitude (see text). The "NM" means that the resolution was not measured.

a granularity of 3 mm pitch is small enough to reach a good spatial resolution and that it does not need to be decreased.
An additional investigation (not discussed in the manuscript) was performed to study the influence of the strong back on the spatial resolution. It was observed that it influences the spatial resolution, thus it is necessary to change the mechanical characteristics of the strong back [92].
The time resolution surface homogeneity studies were performed on the real size SED prototype (section 3.4.2). Due to capacitance issues caused by the increased size of the prototype detector, it was necessary to split the anode of the detector in two. Consequently, the existence of two anodes affects the time resolution of the detector (section 3.4.2). A significant degradation of the time resolution can be observed at the middle of the detector where the two anodes meet. Additionally a smaller effect of resolution degradation can be found at the edges of each of the anodes. This results in a time resolution oscillation depending on the position in the detector (figure 3.22). The difference between the extreme values can be up to several hundred ps at the middle and $\sim$ 100 ps at the edges. A simple method was used for the reconstruction of the amplitude of the signal and consequently, the time resolution in the middle of the detector could be improved. In this case the minimal values of the resolution are a bit higher (20-30 ps) than the minimal non-reconstructed values, but the resolution at the middle of detector is significantly improved (table 3.2).
Finally a study was made to check the influence of the strong back on the time resolution of the real size detector prototype. As can be seen from figure 3.23 there is no real influence from the strong back on the time resolution.
Emissive foils of different thickness and types (materials) are currently being tested, with the goal of additionally reducing the straggling of passing heavy ions. The results of the tests were not discussed in the manuscript [92].

3.5. Conclusions and perspectives

The performed tests indicate that additional work in the development of the SED detector needs to be performed so that the detector meets the required standards. The first task to be addressed is the determination of the position in vertical plane on the detectors. In this case a full assessment of the spatial resolution over the surface can be made, and a solution to minimize the oscillations could be found. The second task would be to find other deposit for the emissive foil to enhance the number of secondary electrons. The signal amplitude could be increased and it would improve the time resolution even in the middle and edges.
Finally I would like to state that additional work needs to be done to optimize the final detector, but the current prototypes are not far from reaching the requirements. In general the spatial resolution of all prototypes is close to specifications, oscillating between 0.9 mm FWHM and 1.5 mm FWHM for strip and 1.5 mm FWHM and 1.8 mm FWHM for inter-strip positions. A time resolution of 116 (3) ps was achieved for real size SED prototype which again is not far from the required resolution.

Chapter 4

Spectroscopy studies of ^{257}Db

It is well known that the $N = 152$ deformed shell gap gives extra stability to the isotopes in the region. Its influence was previously studied on elements like $^{256}_{104}\mathrm{Rf}_{152}$ [10] and $^{255}_{103}\mathrm{Lr}_{152}$ [8]. These investigations confirmed the existence of K-isomers in the region providing many insights into the nature of nuclear excitations and the limits of stability. Additionally, in recent publications the size [6] and the strength [7] of this shell gap were determined. It is of further interest to investigate the behavior and evolution of the $N = 152$ deformed shell gap in the region of heavier isotopes. To this purpose the isotopes of $^{257}_{105}\mathrm{Db}_{152}$ (chapter 4) and $^{258}_{105}\mathrm{Db}_{153}$ (chapter 5) were produced and studied in this work.

The ^{257}Db was previously studied through different production means [96–99]. However only a limited amount of information was gathered on its level and decay schemes, indicating a presence of at least one isomeric state. The daughter nuclei ^{253}Lr and ^{249}Md were also previously investigated.
This study aims to determine the isomeric states in ^{257}Db and its daughter isotopes ^{253}Lr and ^{249}Md.
The results obtained on the structure of ^{257}Db isotope are presented in this chapter 4.2. They are preceded by the description of the calibration procedure of the multi-detector system used in the measurements 4.1.

4.1 LISE: Calibration of the multi-detector system

Before the obtained results of the experiments can be analyzed, the complete detection system needs to be calibrated. There are two reasons for the calibration:

- To have data which have a physical meaning, for example an energy in keV or MeV units, it is necessary to calibrate the detectors to convert their output

from channels to desired units.

- When an experiment is analyzed the data from all electronics channels are summed. It is thus necessary to align the energy scales of these channels. This is achieved by calibrating the detection system.

Two types for calibrations of the detector systems are used:

- The calibration with an external α or γ radioactive source is usually done for a first alignment of the detector strips.
- The in-beam calibrations using a reaction with high cross section producing an isotope with similar characteristics as the isotope which is to be studied is done as a second step for precise calibration accounting the effect of the dead layer of the detector surface.

Calibration with an external source

For the energy calibration of germanium detectors, external γ and X-ray sources, such as ^{152}Eu and ^{133}Ba, are used.
The germanium detectors used in the two analyzed experiments 4.1.3 and 5.1.3 were calibrated with these two γ and X-ray sources.
For the energy calibration of the silicon detectors a three line α source (mixture of plutonium ^{239}Pu ($E_{\alpha_1} = 5105$, $E_{\alpha_2} = 5143$ and $E_{\alpha_3} = 5156$ keV), americium ^{241}Am ($E_{\alpha_1} = 5388$, $E_{\alpha_2} = 5443$ and $E_{\alpha_3} = 5486$ keV) and curium ^{244}Cm ($E_{\alpha_1} = 5763$ and $E_{\alpha_2} = 5805$ keV)) can be used. This type of calibration permits good alignment of different electronics channels and a first hand energy calibration. The LG branch (recoil events) of the DSSD 4.1.1 and the "Tunnel" detector 4.1.2 from ^{257}Db experiment were calibrated in this way.
However this type of calibration has a drawback. When an external α source is used, the α particle arrives from the outside of the detector, loosing a part of its energy in the dead layer. This leads to an overestimation of the energy of the α particles emitted inside the detector, which can be several hundreds of keV for an α particle of 8 MeV. Thus, this type of calibration is not used for the α spectroscopy branch of the DSSD.

In-beam calibration procedure

The decay of the implanted recoil nucleus occurs inside of the detector resulting in no energy loss in the dead layer of the DSSD if the α particle has not escaped the detector.
This type of calibration was used for the HG branch (decay events) in ^{257}Db

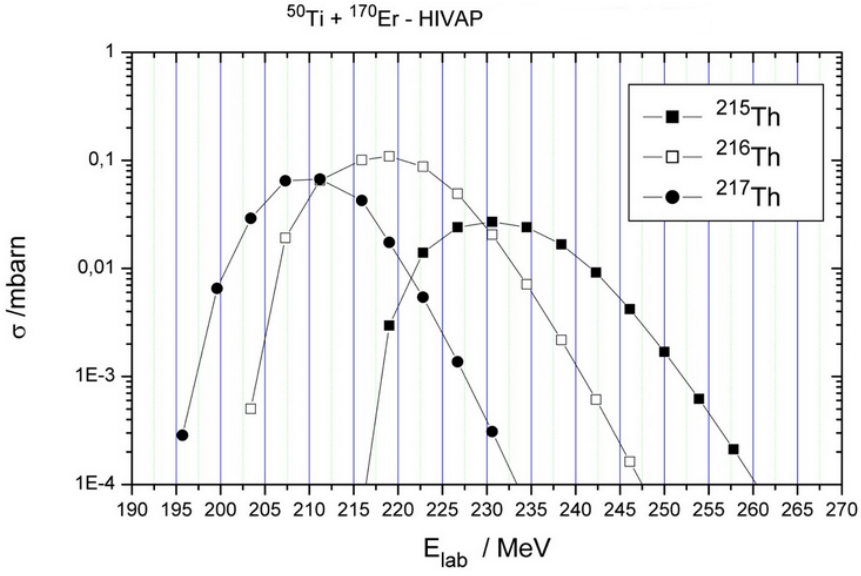

Figure 4.1: Production cross section for different isotopes of Th calculated with HIVAP code.

experiment 4.1.1 and for PSSD 5.1.1 and BOX 5.1.2 detector calibration in ^{258}Db experiment.

The in-beam calibration run used for ^{257}Db experiment was producing ^{216,217}Th through ^{170}Er(^{50}Ti,3(4)n)^{217,216}Th reaction, with the cross section (figure 4.1) of the order of 0.07 to 0.1 mbarn. The beam energy (215-220 MeV) was chosen to produce ^{216}Th as a main channel. A total of 1920 α decays of ^{216}Th were registered, during a measurement of 296 min, in the DSSD for a beam intensity around 73 pnA. The measured transmission of LISE for this run was 0.4 % (chapter 2.2.1).
Calibrations of different detectors are described in the following text.

4.1.1 DSSD calibration

Section 2.4.1 gives a detailed description of the read out of the detectors in this experiment. The DSSD has 16 horizontal strips (X) on the front side (facing the beam) and 48 vertical (Y) strips on the back side. DSSD provides the energy and position information of the implanted (ER) and emitted (α) particles. Energy calibration of the DSSD is performed separately for the ER (LG branch) and for α particles (HG branch). The energy of the implanted particles is several tens to hundred MeV, so the energy range of the LG branch is set to be up to 200 MeV. The energy of emitted α particles is few MeV's so the energy range of the HG branch goes up to 20 MeV.

Alpha energy calibration (HG branch)

Internal α energy calibration of each strip of the DSSD is performed to align the strips of the detector and convert the output signal from channels to energy units (keV). This calibration is performed using the in-beam thorium calibration run. For each strip separately the most intense decays are identified and their mean position is retrieved from the non calibrated α spectra. Alpha transitions of ^{216g,217}Th, ^{212}Ra and ^{208}Rn were used for calibration purposes (figure 4.2). Even

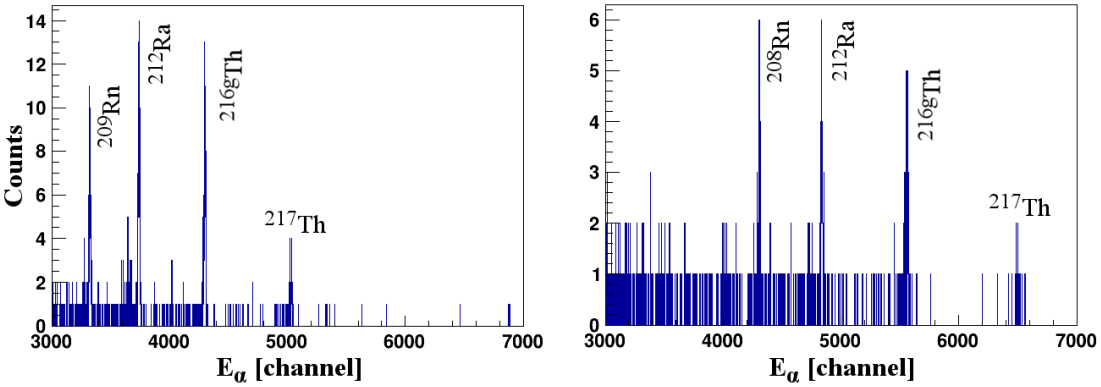

Figure 4.2: Left (Right): Non calibrated α spectra in strip nb.8 (nb. 24) on the front (back) side of the DSSD. The α transitions indicated in the figure were used for energy calibration of the HG branch. The list of all visible and identified α decays can be found in table 4.1.

though the intensity of the ^{217}Th α line is low the energy of this decay is the closest to the expected α energies of ^{257}Db and its daughters. Consequently inclusion of this decay permits better linearity of the calibration at higher energies.
Results of the linear calibration can be found in figures 4.3 and 4.4 for front (X) and back (Y) side of the detector respectively, and in table 4.1. Figure 4.3 on the right shows the calibrated α energy spectra in dependance of the strip number. It can be noted that two strips, nb. 10 and 11, on the front side (X) of the detector were not working.
The front (X) side detector resolution is found in the range between 32 and 40 keV FWHM with a 3.5 % error bar for an energy range of 6.05 to 9.30 MeV.
The back (Y) side detector resolution is found in the range between 38 and 48 KeV FWHM with a 3.5 % error bar for the same energy range. The back side strips of the detector display a bit worse resolution compared to the front side strips.

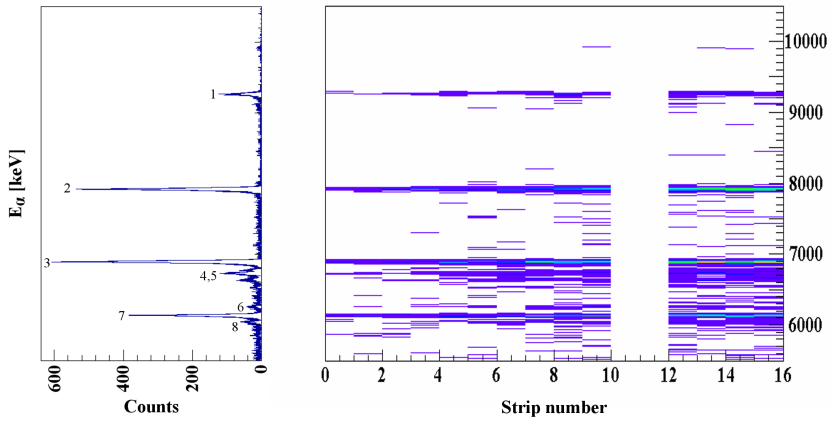

Figure 4.3: Left: Total calibrated α energy spectra summed over all horizontal (X) 14 working strips of the DSSD. Right: Calibrated α energy spectra in dependence of horizontal strip number. Indicated transitions can be found in table 4.1.

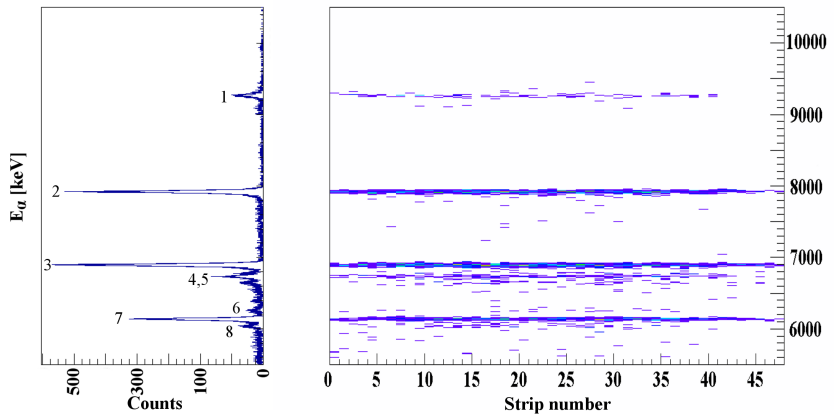

Figure 4.4: Left: Total calibrated α energy spectra summed over all vertical (Y) 48 strips of the DSSD. Right: Calibrated α energy spectra in dependence of vertical strip number. Indicated transitions can be found in table 4.1.

Peak	Element	E_α (X/Y) [keV]	FWHM (X/Y) [keV]	$E_{\alpha_{lit.}}$ [keV]
1	^{217}Th*	9264 / 9265	40 / 48	9261.0
2	^{216g}Th*	7923 / 7921	33 / 40	7923.0
3	^{212}Ra*	6898 / 6897	32 / 45	6898.0
4	^{213}Fr	6777 / 6777	39 / 45	6775.0
5	^{213}Ra	6733 / 6730	39 / 45	6733.0
6	^{212}Fr	6262 / 6265	39 / 38	6261.9
7	^{208}Rn*	6142 / 6138	33 / 38	6140.1
8	^{209}Rn	6049 / 6046	33 / 38	6039.0

Table 4.1: Identified α transitions with energy and FWHM are presented, the decays are indicated in figures 4.3 and 4.4. The peaks used for calibration are marked with a star (*). The value of the α particle energy in the literature is indicated as a reference.

ER energy calibration (LG branch)

The three line α source run for the calibration of the LG branch was performed after the experiment. It is important to note that the strip nb.9 on the front (X)

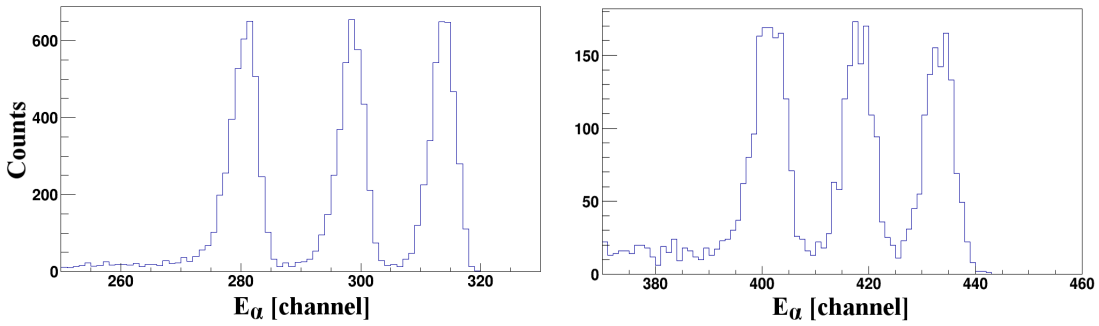

Figure 4.5: Left (Right): Non calibrated three line α source spectra in strip nb.8 (nb.24) on the front (back) side of the DSSD. The three α transitions were used for the energy calibration of the LG branch (ER).

side stopped working during the experiment.
The mean of the three α transitions is retrieved from the non calibrated α spectra (figure 4.5). Results of the linear calibration can be seen in figures 4.6 and 4.7 for the front (X) and back (Y) side of the detector respectively, and in table 4.2.

The resolution of the detector, of both sides, in the LG branch was found to be between 92 and 126 keV FWHM with 1% error bars in an energy spread of 5.1 to

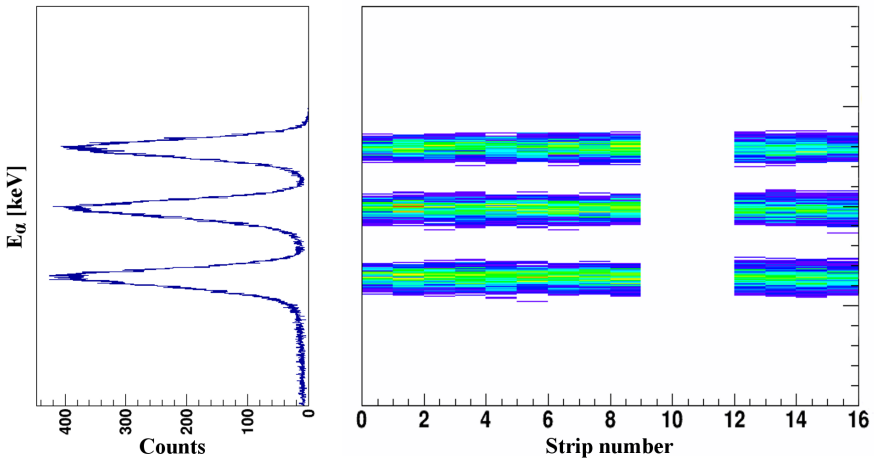

Figure 4.6: Left: Total calibrated three α line energy spectra summed over all horizontal (X) 13 working strips of the DSSD. Right: Calibrated α energy spectra in dependence of horizontal strip number.

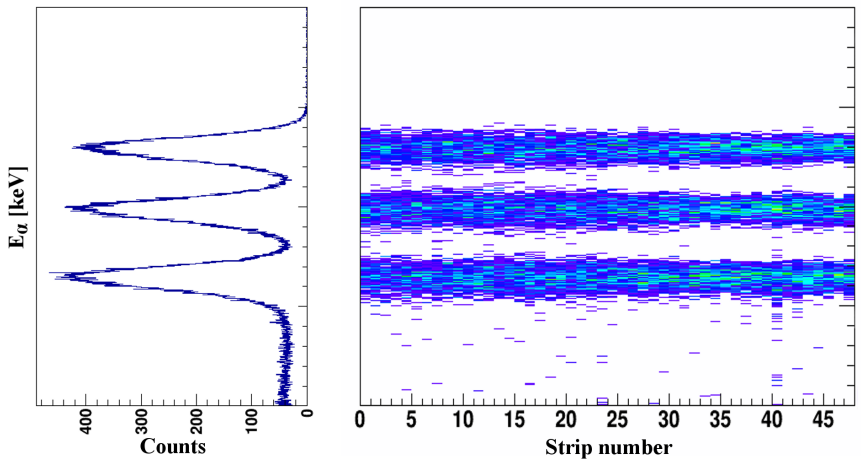

Figure 4.7: Left: Total calibrated three α line energy spectra summed over all vertical (Y) 48 strips of the DSSD. Right: Calibrated α energy spectra in dependence of vertical strip number.

Element	E_α (X/Y) [keV]	FWHM (X/Y) [keV]	Lit. E_α [keV]
^{239}Pu	5149 / 5152	95 / 114	5156
^{241}Am	5494 / 5495	92 / 111	5486
^{244}Cm	5791 / 5793	102 / 126	5805

Table 4.2: Energies of the three α decays obtained after the calibration and summing of the spectra from all working strips of the DSSD (LG branch) are presented. The values of the FWHM are given as well as the literature values for the corresponding transitions.

5.8 MeV. The difference in the resolution between the LG (calibration performed after the experiment) and HG (calibration performed during the experiment) branch comes due to the degradation of the detector performances during the experiment. Since the energies registered in this branch are above few tens of MeV this resolution is not a problem.
The LG branch is used only for recoil identification, and estimation of the ER (recoil) position in the ETOF (energy versus time of flight) matrix. It is therefore sufficient to calibrate the LG branch just with an external three line α source.

4.1.2 Tunnel detector calibration

The Tunnel detector is a combination of four SSSD's from the GABRIELA collaboration. They are set in a Tunnel configuration around the DSSD as it is explained in section 2.4.1 (figure 2.14). Tunnel is used for escaped α particles and electrons.

These detectors were damaged due to the leak in the cooling system for silicon detectors during the experiment. Out of 16 strips (4 strips per detector), 7 strips are still functional, 4 and 3 strips of detector 1 and 3 respectively (figure 2.14).
A calibration with three line α source (same as for the LG branch calibration in section 4.1.1) was performed on the remaining working strips after the experiment. Results of the linear calibration can be seen in figure 4.9 and in table 4.3, and in table 4.3.
The resolution of the "Tunnel" detector is 64 keV FWHM.

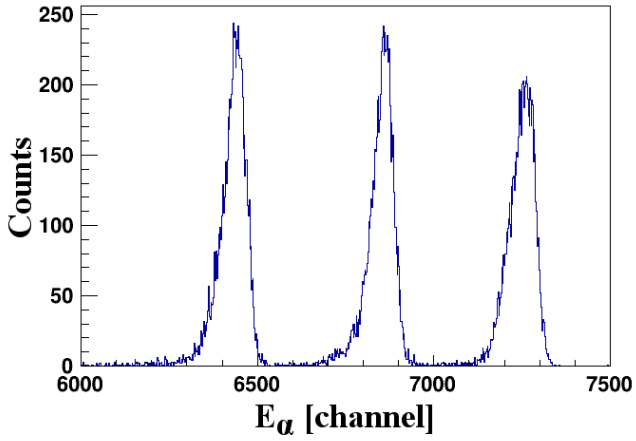

Figure 4.8: Tunnel detector non calibrated α spectra collected in strip nb.14 on the left.

Element	E_α [keV]	FWHM [keV]	Lit. E_α [keV]
^{239}Pu	5153	64	5157
^{241}Am	5486	62	5486
^{244}Cm	5803	64	5805

Table 4.3: Energies of the 3 α lines obtained after the calibration and summing of the spectra from all 7 working strips of the Tunnel detector are presented. The values of the FWHM are given as well as the literature values for the corresponding peaks.

4.1.3 Calibration of the germanium clovers

In the experiment 4 germanium clovers from EXOGAM collaboration were used. Their position and description can be found in section 2.4.1. The calibration of the clovers was performed using a ^{152}Eu source. For the calibration purposes the source was positioned in the middle between the clovers, each crystal of each clover is calibrated separately.
The centroid of the each identified γ-ray transition from the raw spectrum was retrieved (figure 4.10). The non-linearity of the amplifiers used caused slightly different amplifications in the low and high energy part of the spectra. As a consequence the calibration was split in two parts at channel 3000 corresponding to 600 keV. The results of the quadratic calibration can be found in figure 4.12 and table 4.4. The resolution of the germanium detector is 2.4 keV FWHM with 0.3% error bars at 1112 keV energy.

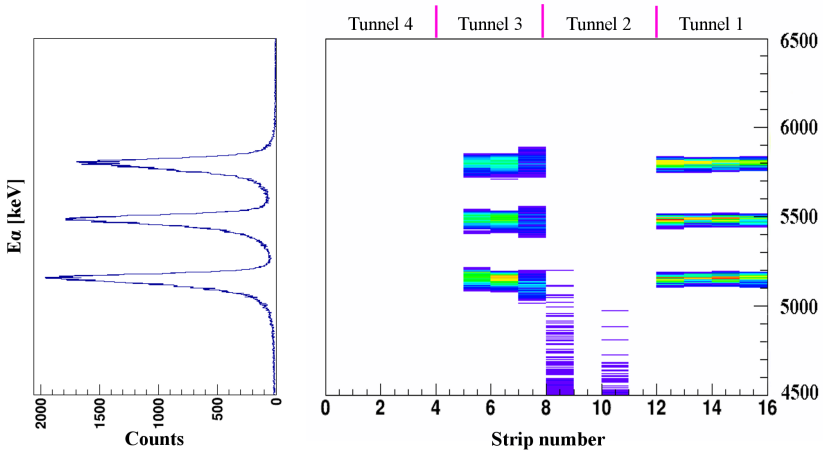

Figure 4.9: Calibrated α energy spectra of the Tunnel detectors. Left: the sum of the α energy over all 7 working strips. Right: α energy in dependence of the strip number. Different SSSD's are indicated on the top of the figure, their position can be seen in figure 2.14.

E_γ [keV]	FWHM [keV]	Lit. E_γ [keV]
121.5	1.9	121.8
245.1	1.9	244.7
343.8	2.1	344.3
367.0	2.8	367.7
411.0	2.1	411.2
444.2	2.1	444.1
778.8	2.4	779.0
867.3	2.4	867.4
963.9	2.4	964.1
1085.7	2.4	1085.8
1112.0	2.4	1112.1
1407.9	2.8	1408.1

Table 4.4: Energies of the ^{152}Eu γ-rays obtained after the calibration and summing of the spectra from all 16 crystals of the 4 clovers are presented. The values of the FWHM are given as well as the literature values for the corresponding peaks.

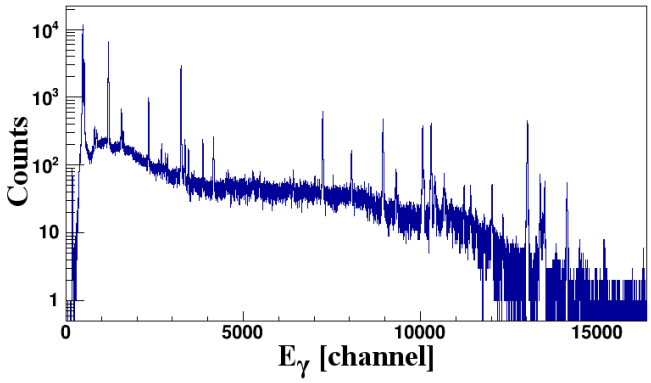

Figure 4.10: Raw γ spectrum of ^{152}Eu gathered in clover nb.1 (back side of the DSSD), crystal B (figure 2.14).

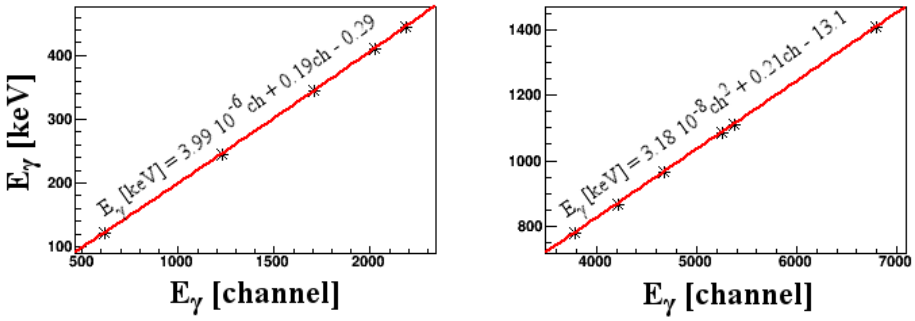

Figure 4.11: Example of the two separate fits for crystal D of germanium clover nb.1. Spectra is separated at channel 3000.

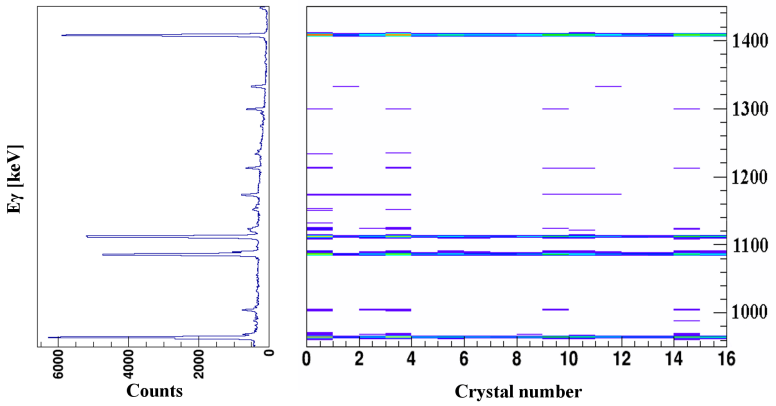

Figure 4.12: Left: Calibrated γ spectra summed over all 16 crystals of germanium. Right: Calibrated γ energy spectra in dependance of the crystal number. Zoom on both figures is made between 950 and 1450 keV for better visibility.

4.2 Spectroscopy of ^{257}Db

^{257}Db was previously studied several times in direct reactions, and as a decay product of ^{261}Bh at SHIP by Heßberger [96–99] and Streicher [100], and at Lawrence Berkeley National Laboratory using the Berkeley gas filled separator by Gates [101]. Summarized results can be found in table 4.5, while the proposed level scheme can be found on the bottom right of figure 4.14. A schematic representation of ^{257}Db α decay chain is given in 4.14. The motivation for the performed experiment was given at the beginning of this chapter.

Isotope	E_α [keV]	$T_{\alpha_{1/2}}$ [s]
^{257}Db	8874 (20)	2.3±0.2
	8956 (20)	$1.5^{+0.9}_{-0.4}$
	9063 (20)	
	9168 (20)	$0.36^{+0.22}_{-0.09}$
^{253}Lr	8710 (20)	$1.2^{+0.7}_{-0.4}$
	8777 (20)	$0.7^{+0.5}_{-0.2}$
^{249}Md	8026 (10)	23±3
^{245}Es	7730(10)	66±6

Table 4.5: Summarized spectroscopic data of former experiments performed on ^{257}Db and its α products [96–99]. The information for ^{245}Es are adopted from [102].

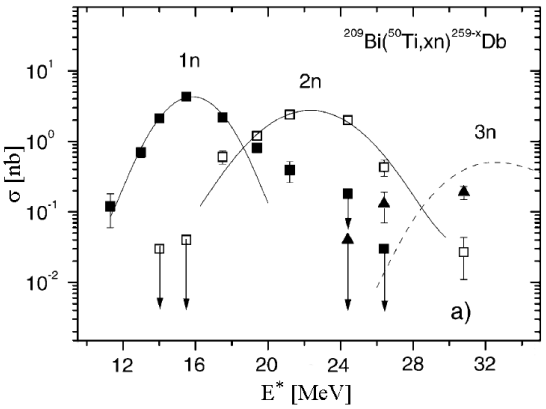

Figure 4.13: Experimental excitation function for ^{50}Ti + ^{209}Bi. The measured excitation functions for 1n channel (^{258}Db) is presented as full squares, 2n channel (^{257}Db) as open squares and 3n channel (^{256}Db) as full triangles [97], the lines are placed to guide the eye. The error bars present statistical errors only. Figure adopted from [97].

4.2. Spectroscopy of ^{257}Db

In this study ^{257}Db was directly produced trough the 2n channel of fusion-evaporation reaction using ^{50}Ti beam on ^{209}Bi target. The measured excitation function [97] is shown in figure 4.13. The spectroscopic studies of ^{257}Db and its daughters were performed using generic correlations.

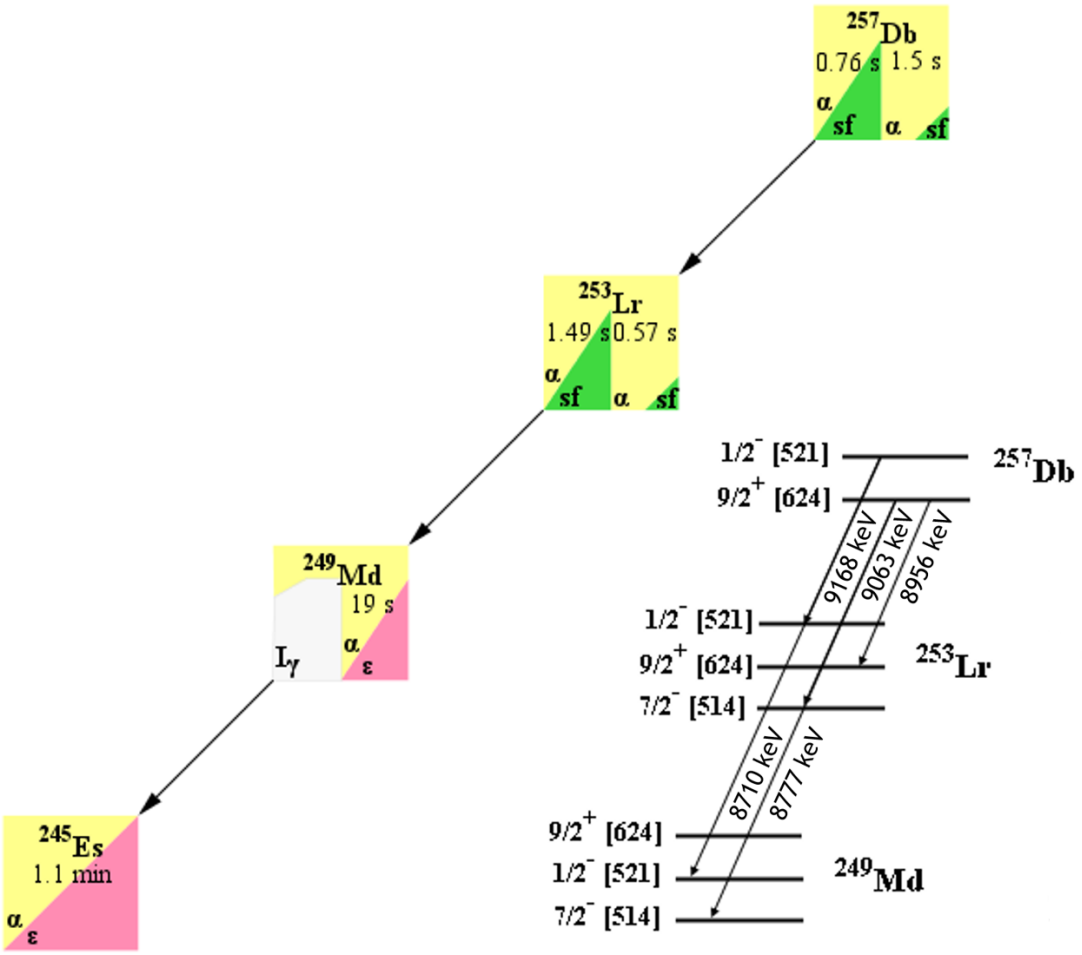

Figure 4.14: Schematic representation of ^{257}Db decay chain. Level scheme proposed by Heßberger and collaborators in [97].

4.2.1 Correlation gates

The structure of the ^{257}Db and its daughters was probed with the generic correlation method. To apply this method it is necessary to choose proper energy, time and position gates.

Position gates require that the correlated recoil and α or two α particles are found in the same position in the DSSD. For this analysis one pixel of a DSSD is chosen as a position gate for the correlation purposes. This gate was tested on the calibration run of thorium, where the multiplicity (number of strips hit in coincidence) of events was checked. A multiplicity grater than 1 can be caused by inter strip events, cross talk, etc... It was determined that 6 % of events have multiplicity bigger than 1 for the strips on the front side of the detector (X), and 1.3 % for the strips on the back side of the detector (Y), as can be seen in figure 4.15. It is thus justified to require multiplicity equal to 1 (1 pixel of the DSSD) for the correlation purposes.

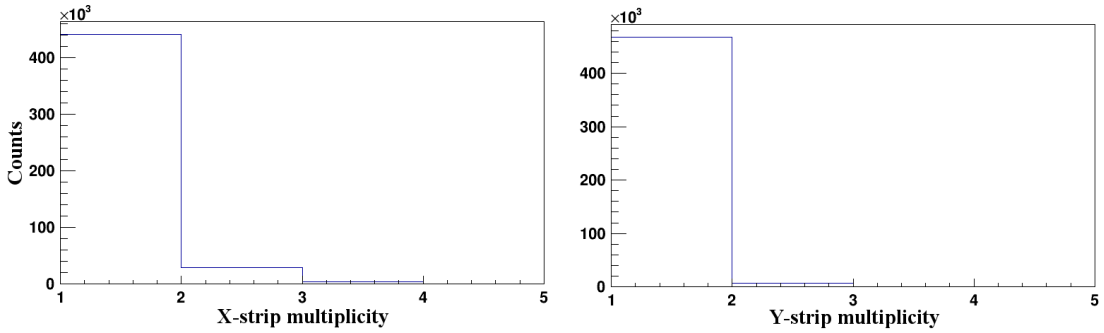

Figure 4.15: Left (Right): Multiplicity on the front (back) side of the DSSD. Figures obtained from ^{216}Th calibration run.

Time windows are chosen depending on the investigated half life of the nuclei. For example, in order to determine the half lives and the energies of the α decays of ^{257}Db, recoil-α correlations are performed in a time window of 12 or 7 s. These values correspond to 5 and 3 times of the previously measured half life (table 4.5) of ^{257}Db. The results obtained using these two time windows should be comparable inside the error bars.
The applied time correlation windows are indicated throughout the text.

Energy gates are used for a couple of reasons:

- Different energy gates are set on the α particles and/or γ-rays to probe the fine structure of the nucleus. They permit study of the mutual dependence

of several α decays coming from different isotopes, as well as correlations between α and γ-ray emission. These gates are indicated throughout the text.

- The amount of random correlations between the events in LG branch (section 2.4.1), which are not the ER, and the α particles is reduced by choosing the proper energy gates in the LG branch. To be precise, selection of the correct ER is not based purely on its energy, but rather on the combination of energy and time of flight information. Additionally, the position gate, previously described, has to be respected.

The selection of ER is performed using the measured recoil energy and the time of flight. As the kinetic energy depends on the mass and the velocity ($E = mv^2/2 = ms^2/(2t^2)$) it is possible to identify different mass regions in the ETOF matrix. In order to properly select a region of the ETOF matrix in which the ER should be situated an approaching previously studied reaction is used.
The position of the ^{257}Db nuclei in the ETOF matrix is obtained from the position of the ER correlated to short lived (26 ms) ^{216}Th α decay (figure 4.16). The amount of random correlations is small (or negligible) due to the short half life of ^{216}Th.

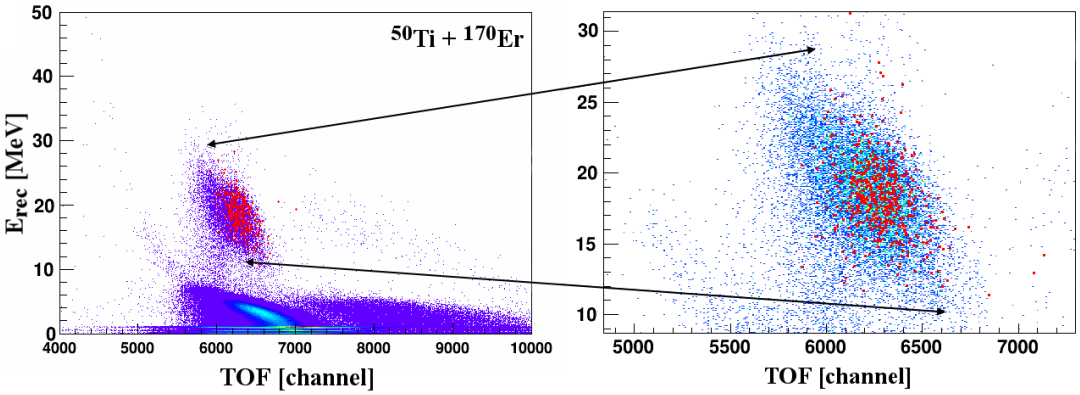

Figure 4.16: The ETOF matrix for ^{170}Er(^{50}Ti,4n)^{216}Th reaction. The red dots represent the ER of ^{216}Th correlated to the α decay in a time window of 78 ms. The TOF detector used is the same as the one used during ^{257}Db runs. Figure on the right shows the zoom of the region in which the ER of ^{216}Th (red dots) are positioned.

The position of the ^{257}Db ER, correlated to an α decay in a time window of 12 s, can be seen in figure 4.17. The energy and time of flight gate for the ^{257}Db nuclei was deduced from the ETOF matrix 4.16 of ^{216}Th data. The large amount

of transfer products can be seen in the spectra of ^{257}Db mixing with the ^{257}Db nuclei 4.17.

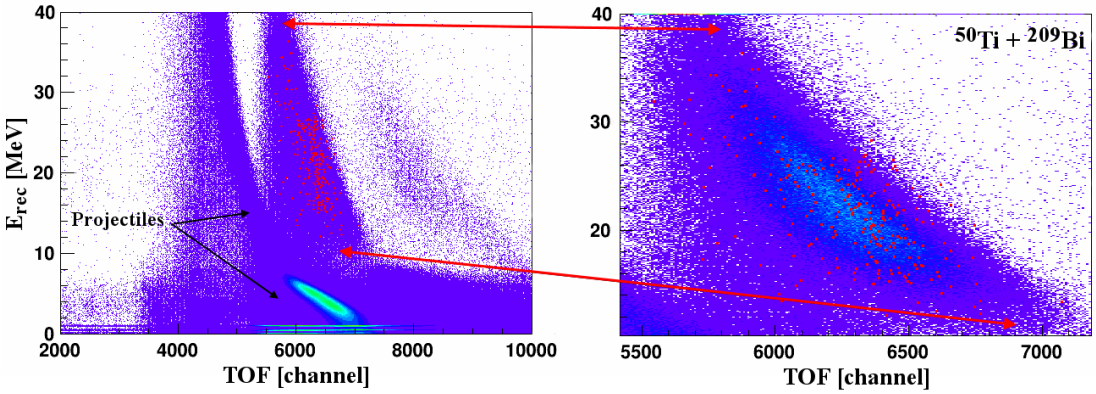

Figure 4.17: The ETOF matrix for ^{209}Bi(^{50}Ti,2n)^{257}Db reaction. The red dots represent the ER of ^{257}Db correlated to the α decay in a time window of 12 s. Figure on the right shows the zoom of the region in which the ER of ^{257}Db (red dots) are positioned.

4.2.2 Decay of ^{216}Th: test of the off-line analysis code

The off-line analysis code was tested on the thorium calibration run. Some of the obtained results are shown in the following text.
This code was further used to analyze the data from the ^{257}Db experiment (4.2.3), and was adjusted for the analysis of the data from the ^{258}Db experiment (5.2).

Structure of ^{216}Th: recoil-α correlations

The structure of the targeted nucleus (^{216,217}Th in this case) is studied with the recoil decay tagging method. The same procedure is later used for ^{257}Db (4.2.3) and ^{258}Db (5.2).

The total α spectra obtained during the calibration run in the DSSD can be found in figures 4.3 and 4.4.
The α decays of ^{216g}Th (7926 (14) keV) and ^{217}Th (9268 (14) keV) can be identified in figure 4.18 on the left hand side. Additionally the decays of ^{216}Ac and ^{216m}Th can be seen.
The half life of the ^{216g}Th α decay was determined to be 25±2 ms, using the exponential function (figure 4.18 on the right hand side). However, another method [103] can be used to retrieve a half life of a decay and is described in the following text.

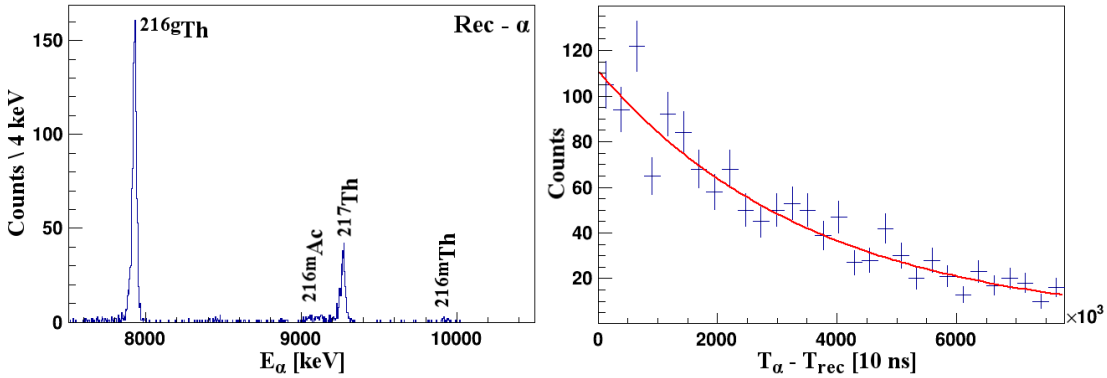

Figure 4.18: Left: Alpha decays correlated to ER in a time window of 78 ms ($3xT_{1/2}$ of ^{216g}Th). Identified α transitions are indicated. Right: Decay time of ^{216g}Th obtained for an energy range 7.9 MeV to 8.0 MeV and a time window of 78 ms.

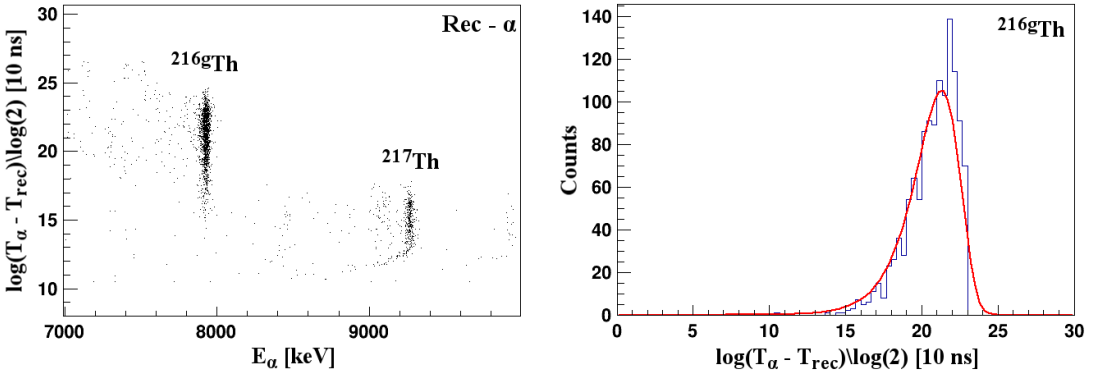

Figure 4.19: Left: Logarithmic representation of the time difference in dependance of the energy of the α decay. Alpha transitions are indicated in the figure. Right: Projection of the time difference on the Y-axis from the figure on the left in an energy range 7.9 MeV to 8.0 MeV (^{216g}Th). The fit of the function gives the half life of ^{216g}Th according to method used in [103].

The relation between the time difference ($dT = T_\alpha - T_{rec}$) and the corresponding energy is shown on the left hand side of figure 4.19. On the right hand side, the projection of a selected α decay on the time axis is presented. It is now possible, using the method described in [103], to obtain the half life of this decay from the the following functions:

$$f(A, t_1, t_2, C) = \frac{A}{t_1}\, exp\,(x\, log(2))\; exp\left(\frac{-1}{t_1\, exp(x\, log(2))}\right)\; exp\left(\frac{-1}{t_2\, exp(x\, log(2))}\right) + \frac{C}{t_2}\, exp\,(x\, log(2))\; exp\left(\frac{-1}{t_2\, exp(x\, log(2))}\right) \tag{4.1}$$

or by:

$$f(A, t_1) = \frac{A}{t_1}\, exp\,(x\, log(2))\; exp\left(\frac{-1}{t_1\, exp(x\, log(2))}\right) \tag{4.2}$$

where t_1 is the half life of the decay, t_2 "half life" of random events, A and C are counts of the decay and random events respectively.
Half lives of 26±1 ms for ^{216g}Th and 367±20 μs for ^{217}Th were obtained using this method, and are in agreement with previously reported values. It can be noted that the two methods are equivalent.

A decay scheme of an isotope is determined from the observations of γ-ray transitions correlated to other γ-rays or decay particles.
Two γ-ray transitions of 674 keV and 1270 keV were found preceding the α decay of ^{217}Th in a time window (T_γ-T_{recoil}) of 5 μs. These two transitions were previously reported as a dexcitation of the $15/2^+$ to $9/2^+$ state (ground state of ^{217}Th) and $17/2^-$ to $15/2^+$ state respectively [104].
Three γ-ray transitions (previously reported [105]) of 200 keV (6^+->4^+), 126 keV (4^+->3^-) and 209 keV (3^-->2^+) were found preceding the α decay of ^{216g}Th in a time window of 50 μs.

Considering that the code reproduces well the values of the energies and half lives of well known thorium decays, it is possible to use the code for the further analysis of dubnium.

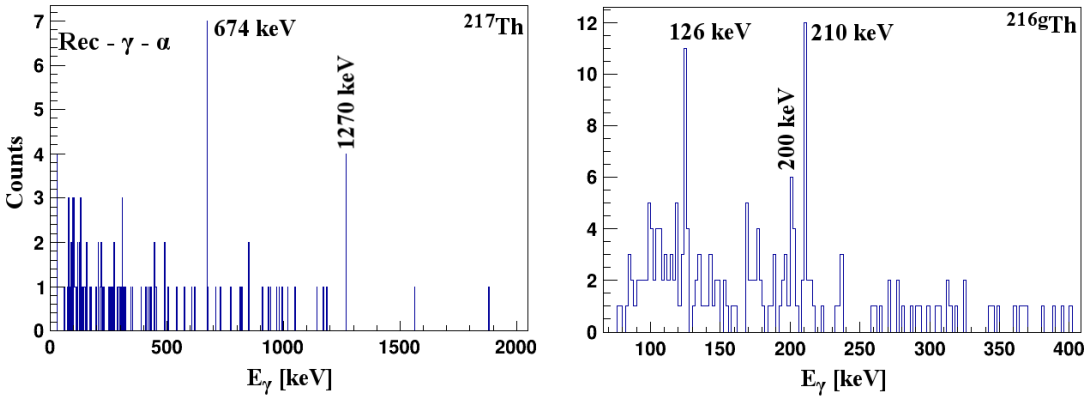

Figure 4.20: Left (Right): Gamma-rays found in coincidence with ^{217}Th (^{216}Th) α decay from the recoil-γ-α correlations in a time window (T_γ-T_{recoil}) of 5 μs (50 μs).

Structure of daughter nuclei: α-α correlations

The structure of the daughter isotopes (^{212,213}Ra and ^{208,209}Rn in this case) is probed through the α-α and recoil-α-α correlations. Additional information are gathered from the γ and X-ray coincidences.
Consecutive α decays with a time difference up to 65 s (5x$T_{1/2}$ of ^{212}Ra) can be seen in figure 4.21. The number of random correlations depends on the length of the time window.
The following connections are observed in the figure 4.21:

- ^{216m}Th -> ^{212}Ra
- ^{217}Th -> ^{213}Ra
- ^{216g}Th -> ^{212}Ra
- ^{216g}Th -> ^{208}Rn
- ^{212}Ra -> ^{208}Rn

as well as the random correlations which are the consequence of the length of the time window. Therefore, well adjusted energy and time gates are necessary to do detailed spectroscopic studies.
On the left hand side of figure 4.22 the α decay of ^{212}Ra following the decay of ^{216g}Th (7.9 to 8 MeV) in a time window of 39 s (3x$T_{1/2}$ of ^{212}Ra) is shown. A similar coincidence search was applied on all decays studied in this work. The results from the studies performed on ^{216,217}Th can be found in table 4.6.

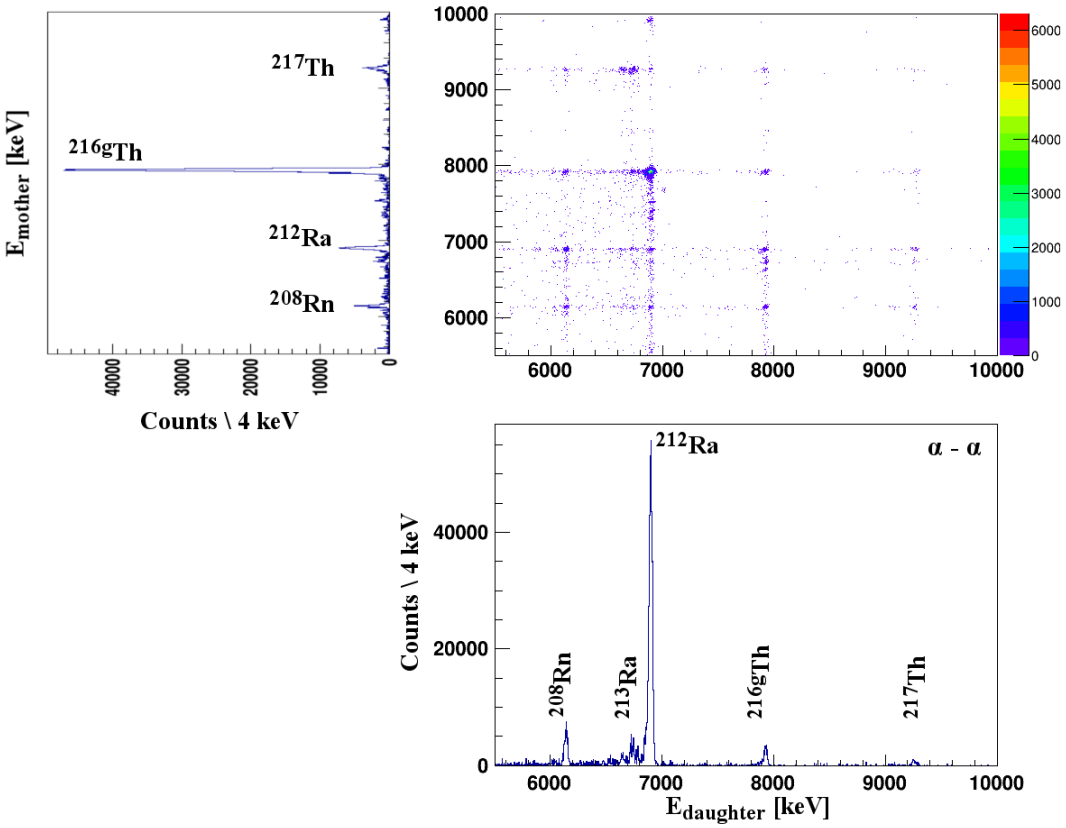

Figure 4.21: The figures were obtained from α-α correlations performed in a time window of 65 s. Identified α transitions are indicated.
Top left: Energy of the α decays of the mother nucleus. Top right: Energy of the α decay of the mother nucleus in dependance on the α energy of the daughter nucleus. Bottom right: Energy of the α decay of the daughter nucleus.

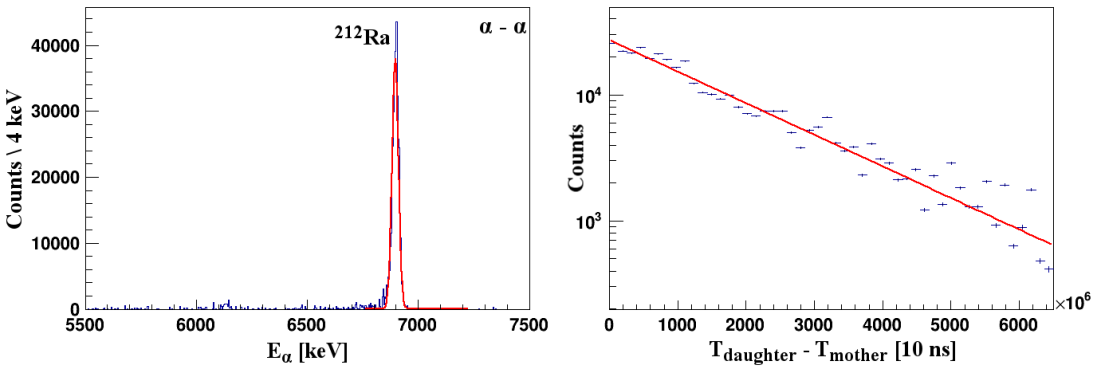

Figure 4.22: Left: Alpha decay of ^{212}Ra correlated to an α decay of ^{216g}Th in a time window of 39 s. Right: determination of the half life of the α decay of ^{212}Ra.

The obtained results confirm that the developed code can be used for the analysis of the dubnium runs.

	This work		Litt. values	
Isotope	E_α [keV]	$T_{1/2}$ [s]	E_α [keV]	$T_{1/2}$
^{212}Ra	6898 (14)	12±0.5	6899 (17)	13±2 [s]
^{213}Ra	6646 (19) 6731 (19)		6625 (3) 6733 (3)	164±4 [s]
^{208}Rn	6140 (13)		6140 (17)	24.4±1.4 [min]
^{209}Rn	6045 (10)		6039 (3)	28.8±0.9 [min]

Table 4.6: Results of α-α correlations for the decay chain of ^{216,217}Th compared to the previously reported values [8, 102, 104].

4.2.3 Decay of ^{257}Db: structure study

The structure of ^{257}Db isotope and its daughters was studied via recoil decay tagging, as previously mentioned. The main analysis was conducted using the α decay of produced isotopes and it was complemented with the correlated γ and X-ray transitions.
The energy distribution of the collected α decays in the DSSD in the range 8 MeV to 10 MeV in anticoincidence with TOF signal can be seen in figure 4.23. The figure on the top shows the α decays collected in the vertical strips on the back side of the detector, while figure on the bottom shows the α decay signals in the horizontal strips on the front side of the detector. It is clear that the separate α decays of ^{257}Db (8.8 to 9.2 MeV) and daughter isotopes (7.6 to 8.8 MeV) cannot be

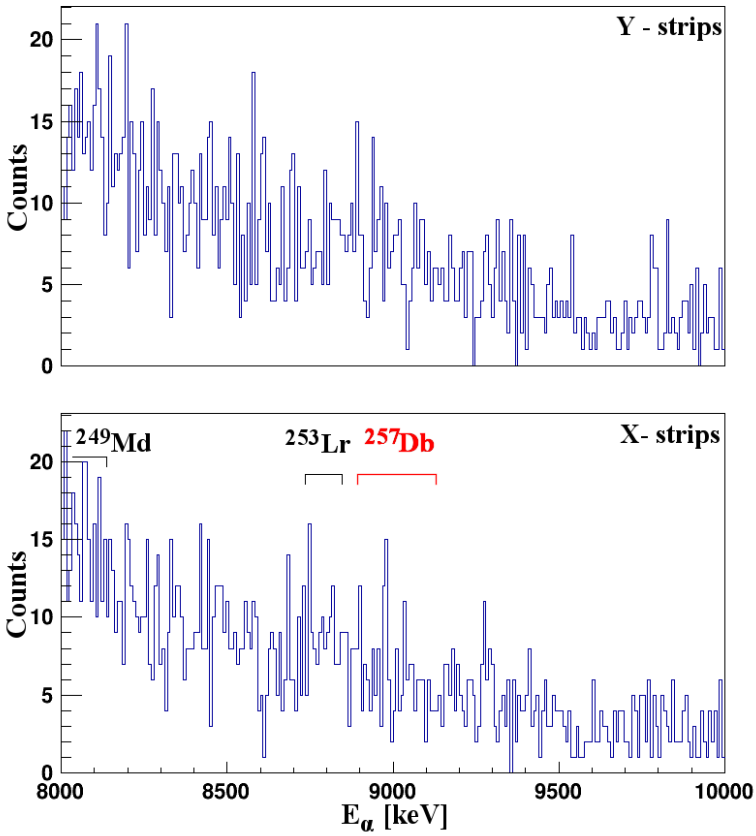

Figure 4.23: Top (Bottom): Total α spectrum collected in anticoincidence with TOF signal on the back (front) side of the DSSD.

identified in this spectra. This is a consequence of the energy of the implanted ER not being lowered by any degrader. Therefore the identification of the α decays can be done only from the recoil-α and α-α correlated spectra. The spectra from the front and back side of the detector are equivalent as can be seen in figure 4.23. The spectra shown later in the text are the ones gathered on the front side, if not indicated differently.

Structure of ^{257}Db

The results of the recoil-α correlations, performed in a time window of 12 s ($5xT_{1/2}$) or 7 s ($3xT_{1/2}$, table 4.5), used to probe the structure of the ^{257}Db isotope, are discussed in the following text.

The energy distribution of the α events correlated to an ER can be seen in figure 4.24, on the left hand side. It can be noted that the amount of events, in the energy regions in which the α decays are expected, is significantly higher compared to the rest of the energy range. Consequently, it can be concluded (to some extent) that the observed α decays belong to ^{257}Db and its daughters.
Two Gaussian shaped α lines in the energy range 8.70 MeV to 8.85 MeV (^{253}Lr) can be identified in the figure 4.24, on the right hand side. These decay lines belong to ^{253}Lr and are a consequence of recoil-α correlations to the second generation α decays due to the fact that the first generation α particles (^{257}Db) have escaped the detector. A value of 56 keV FWHM with 20 % error bar is obtained from the fit of the two ^{253}Lr α peaks, this value corresponds to the resolution of the detector (40-50 keV FWHM at the energy of 9260 keV).

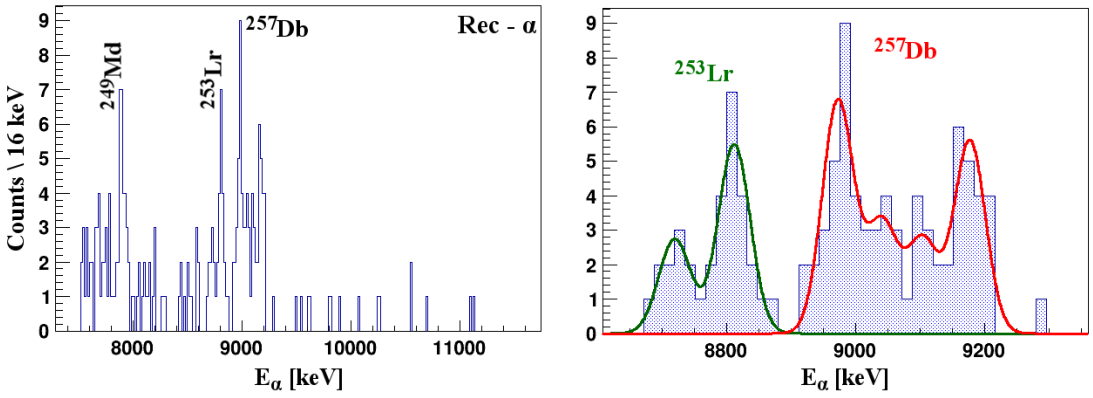

Figure 4.24: Left: Spectrum of the α transitions correlated to ER events in a time window of 12 s. Right: Zoom on the energy region containing ^{257}Db and ^{253}Lr α transitions. The fits for determination of the decay energy are indicated.

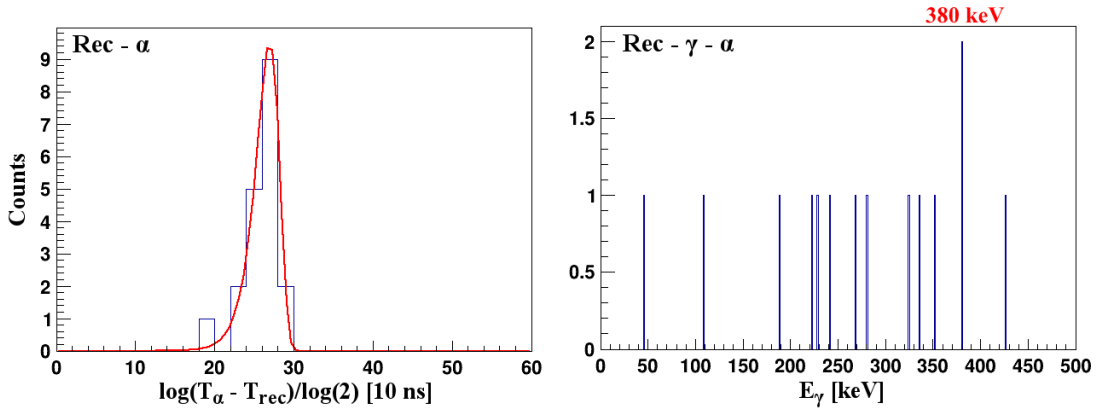

Figure 4.25: Left: Half life estimation from the recoil-α correlations in the energy range 8.9 to 9.0 MeV (^{257}Db α decay of 8973 (24) keV) with a time window of 12 s. Right: Gamma-ray energies found in the recoil-γ-α correlations where the α decay energies are in the range 8.9 to 9.3 MeV (^{257}Db), with a time window of 12 s between the ER and the α decay.

Four α decays with energies of 8973 (24), 9041 (24), 9104 (24) and 9177 (24) keV are obtained when the previously determined constraint of 56 keV FWHM is applied on the decays in the energy range of 8.9 to 9.3 MeV (^{257}Db). However, from the shape of the decay curves it is possible to identify only two α decays with energies 8973 (24) and 9177 (24) keV. Comparison of the rest of this decay energy range with the background indicates that the observed events cannot be attributed to the background. Therefore these events could be a consequence of an additional α decay, and/or arise from the summing of the two previously identified α decays with conversion electrons. Nonetheless, the origin of these events cannot be determined without more statistics.
A half life of 2.2±0.6 s was determined for the ^{257}Db α decay with an energy of 8973 (24) keV, the obtained value is in agreement with previously published one (table 4.5). For the α decay with energy of 9177 (24) keV a half life of 0.8±0.3 s, in agreement with previously reported ones [100, 101], was obtained (figure 4.25).
Gamma-ray transitions are used to probe the fine structure of investigated isotopes. The α decay lines of ^{257}Db (8.9 to 9.3 MeV) were found in coincidence with two γ-ray transitions of 380 keV in a time window of 1 ms (figure 4.25 on the right hand side). Unfortunately it was not possible to correlate this γ-ray transition to a specific α decay. From the recoil-γ-α correlations it was found that each α decay of ^{257}Db, 8973 keV and 9177 keV, is preceded by one γ-ray transition with an energy of 380 keV. Previously, it was determined that the two α decays of ^{257}Db are characterized with two different half lives indicating that they are emitted from

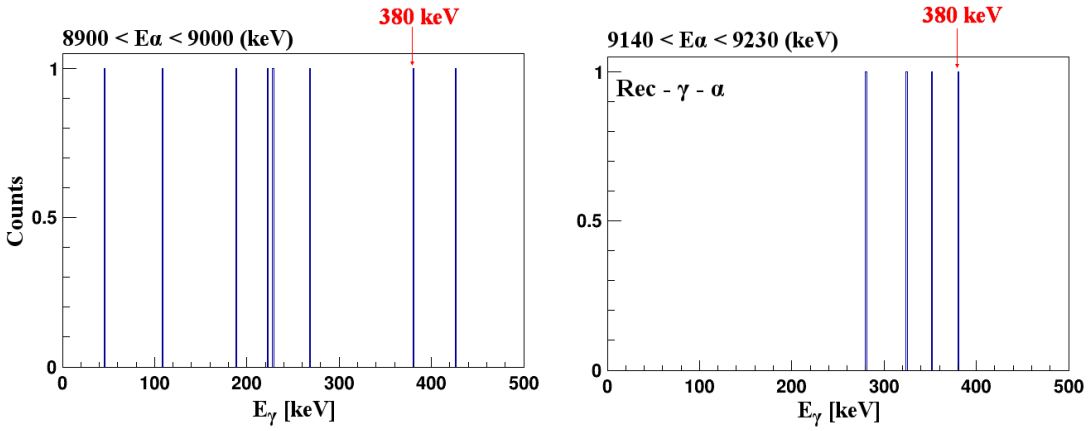

Figure 4.26: Left (Right): Gamma-rays found in coincidence with ^{257}Db α decay in an energy range 8.9 to 9.0 MeV (9.14 to 9.23 MeV). The γ-ray transition with an energy of 380 keV is indicated. These figures should be compared to figure 4.25 on the right.

two different states in ^{257}Db. If it is consider that there is two levels in ^{257}Db these correlations would indicate that both levels are populated by two excited states positioned 380 keV above them, this scenario is very unlikely. A bit more probable scenario would be that the two α decays are emitted from the same state which is populated by a state 380 keV above it. Considering the statistics involved, it is not possible to draw reliable conclusions on the account of the γ-rays.

Structure of the (grand) daughter nuclei

The structure of the daughter (^{253}Lr) and grand daughter (^{249}Md) isotopes is obtained from the α-α, recoil-α-α and correlations to γ and X-rays.
A general overview of the α-α correlations is given in figure 4.27. The results are obtained in a time window of 69 s (3x$T_{1/2}$ of ^{249}Md, table 4.5). It has to be taken into account that increasing the time window increases the numbers of random correlations.
Figure 4.27 b) shows the correlations between mother and daughter α transitions. Figures a) and c) show the energy distribution of the mother and daughter α decays respectively. It is possible to identify the following correlations between four generations of α transitions:

- ^{257}Db -> ^{253}Lr
- ^{257}Db -> ^{249}Md
- ^{253}Lr -> ^{249}Md

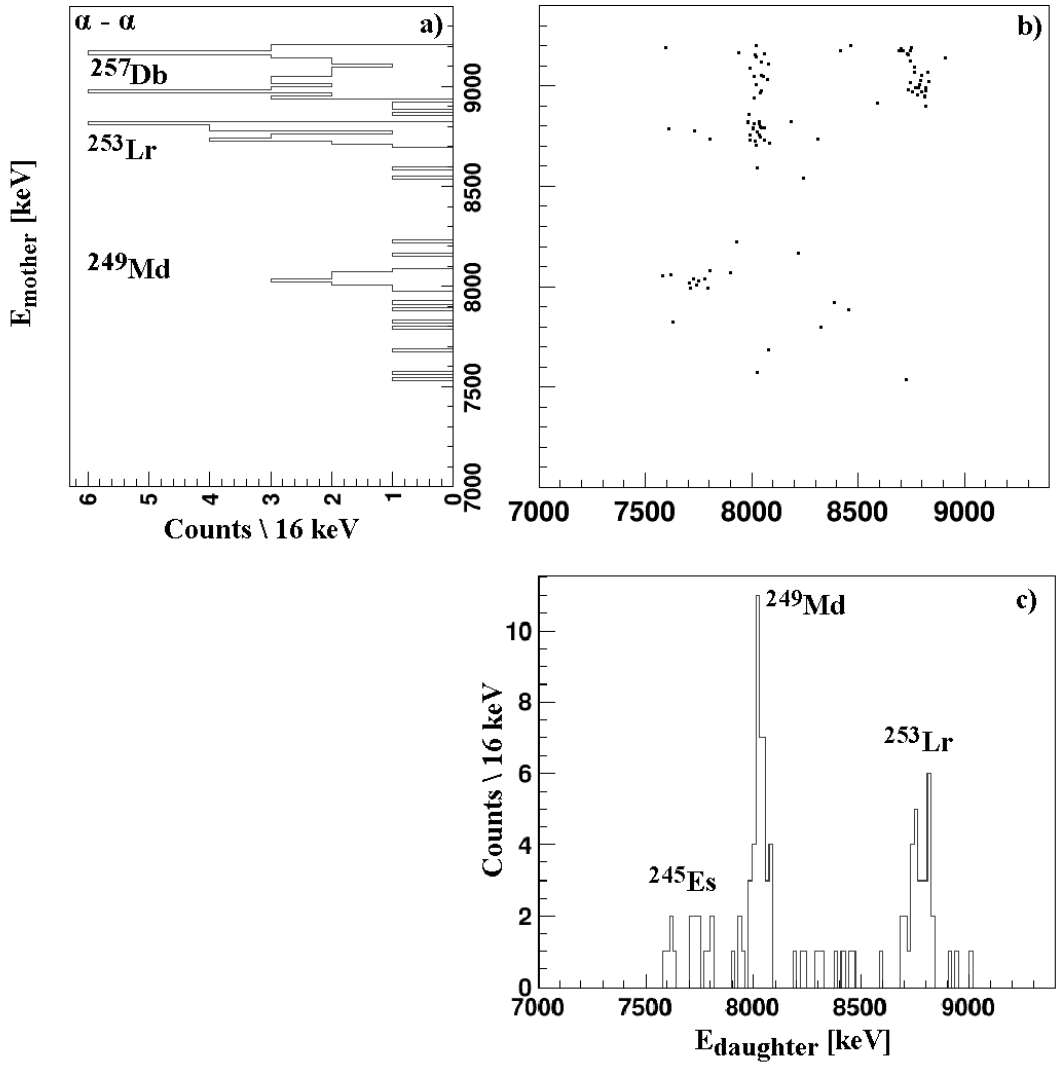

Figure 4.27: The figures were obtained from α-α correlations performed in a time window of 69 s. Identified α transitions are indicated.
a) shows the α energy of the mother nucleus. It is the projection of figure b) on the Y-axis. b) shows the α energy of the mother nucleus in dependance on the α energy of the daughter nucleus. c) shows the α energy of the daughter nucleus. It is the projection of figure b) on the X-axis.

- ^{249}Md -> ^{245}Es
- ^{253}Lr -> ^{245}Es

A detailed analysis of each of these correlations is performed using adjusted time and energy windows and is discussed in the following sections.

^{253}Lr and ^{249}Md

The structure of ^{253}Lr is probed within a time window of 6 s which corresponds to 5x$T_{1/2}$ of ^{253}Lr, see table 4.5.

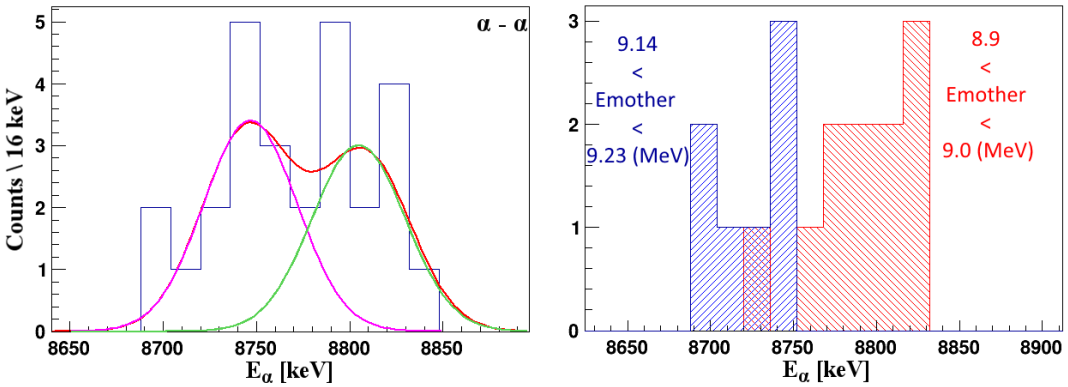

Figure 4.28: Left: ^{253}Lr α decays correlated to ^{257}Db α transitions. Right: ^{253}Lr α decay correlated to 8973 keV (9177 keV) ^{257}Db α transitions presented in red (blue) spectrum.

A total of 31 α decay events of ^{253}Lr was found in coincidence with ^{257}Db α decays (figure 4.28, on the left hand side). Previously obtained value of 56 keV for the widths of the peak was used to retrieve the energies of the ^{253}Lr α decays (figure 4.24).The two obtained values of 8745 (24) and 8808 (24) keV are in agreement with the ones obtained from the recoil-α correlations, as well as with the previously reported ones (table 4.5).
Coincidences between different α decays of ^{257}Db and ^{253}Lr can be found in figure 4.28, on the right hand side. Thirteen events (red spectra) correlate the 8973 (24) keV ^{257}Db with the 8808 (24) keV α decay of ^{253}Lr. Seven events (blue) correlate the 9177 (24) keV ^{257}Db with the 8745 (24) keV α decay of ^{253}Lr. These coincidences confirm the previously observed and reported correlations in [97].
A half life of 2.0±0.5 s was obtained for the ^{253}Lr α decay with an energy of 8745 (24) keV and 1.0±0.3 s for the 8808 (24) keV decay. These values are slightly

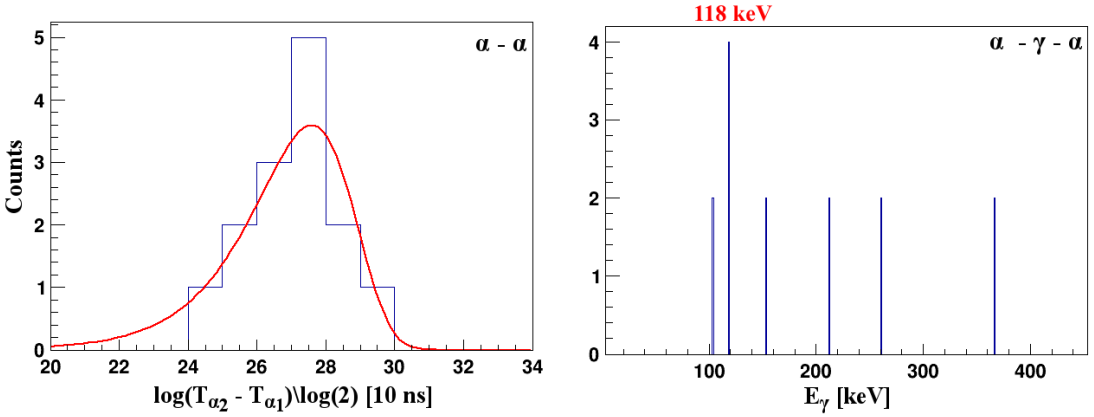

Figure 4.29: Left: Estimation of the ^{253}Lr half life in an energy range 8.70 to 8.87 keV (8745 keV α decay)in a time window of 6 s. Right: Gamma-rays in coincidence with the α decay of ^{257}Db correlated to α decays of ^{253}Lr.

higher than the previously reported ones, but are in agreement inside the error bars.

Four γ-ray transitions with an energy of 118 keV could be attributed to ^{253}Lr, these transitions were obtained from the α-γ-α correlations over the complete range of α decays of the two isotopes in a time window os 1 ms (figure 4.28, on the right hand side). Separate coincidences performed by gating either on the 8973 keV or 9177 keV decay of ^{257}Db reveled two γ-ray transitions following each of the two α decays. Unfortunately, it is not possible to draw reliable conclusions based on this type of results, as was discussed previously in section 4.2.3.

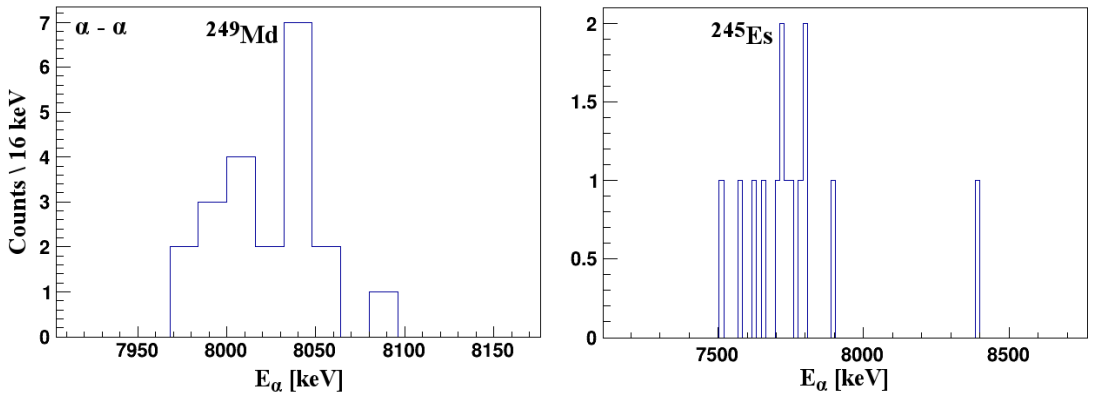

Figure 4.30: Left (Right): Alpha decay of ^{249}Md (^{245}Es) correlated to the α tarnsitions of ^{253}Lr (^{249}Md).

Correlations to the third generation α particles reveled 20 α decays of ^{249}Md in an energy range 7.95 to 8.10 MeV (table 4.5) following the decay of ^{253}Lr (figure 4.30, on the left hand side). A half life of 27±6 s (in agreement with previously published results) was obtained from this decay.
From the correlation to the fourth generation α particles (time window of 115 s) 7 α decays of ^{245}Es were observed following the ^{249}Md decay (figure 4.30, on the right hand side). The reported half life of ^{245}Es is 1 min, consequently a time window of 115 s is not enough to perform proper correlations, however it was limited by random correlations.

4.2.4 Conclusion

The motivation of the performed experiment was to investigate the fine structure of ^{257}Db and its daughter isotopes in order to determine the energies of their populated levels.
The ^{257}Db was produced through the 2n channel of fusion-evaporation reaction at GANIL. The experiment suffered through a lot of technical difficulties, and only one third of the dedicated beam time was used for the production of ^{257}Db for the spectroscopy studies. Additionally, the measured transmission for the thorium run was 0.4%. Such a low value additionally decreases the amount of gathered events. Consequently, this influenced the amount of gathered events of ^{257}Db. Nevertheless, conclusions could be draw on the structure of these isotopes.
Energies and half lives of ^{257}Db, its daughter ^{253}Lr and grand daughter ^{249}Md were determined. Additionally, correlations with ^{245}Es were observed. The results are summarized in table 4.7.

Isotope	E_α [keV]	$T_{\alpha_{1/2}}$ [s]
^{257}Db	8973 (24)	2.2±0.6
	9177 (24)	0.8±0.3
^{253}Lr	8745 (24)	2.0±0.5
	8808 (24)	1.0±0.3
^{249}Md	7950 - 8100	27±6
^{245}Es	7700 - 7800	

Table 4.7: Energies and half lives of the α transitions observed in this work for the identified isotopes.

Moreover, a clear separation, in agreement with previously reported results [97], in the coincidences between ^{257}Db and ^{253}Lr α decays was observed. The 8973 keV ^{257}Db α decay is followed by the 8808 keV α of ^{253}Lr, while the 8745 keV α decay of ^{253}Lr follows the 9177 keV decay of ^{257}Db (section 4.2.3).

Few γ-ray transitions were found in coincidence with the observed α decays. However, the statistics was not sufficient to clearly identify the correlations between them. Consequently no conclusion was drawn on the populated levels of ^{257}Db and its daughters and no level scheme is presented.

Chapter 5

Spectroscopy studies of ^{258}Db

The goal of the performed experiment is to investigate the deformed $N = 152$ shell gap behavior and its influence on the formation of the K-isomers in the region, as it was discussed in chapter 4.
This chapter is dedicated to the analysis and discussion on the results of the spectroscopic studies performed on $^{258}Db_{153}$ isotope. The calibration procedure (section 5.1) for the detector system at SHIP is described at the beginning of the chapter. It is followed by a discussion (section 5.2) on the obtained results (section 5.2.3).

5.1 SHIP: Calibration of multi-detector system

General calibration procedures and reasons for performing them were previously discussed in section 4.1.
The primary calibration of the silicon detectors for ^{258}Db experiment was performed with a three α line source (mixture of ^{239}Pu, ^{241}Am and ^{244}Cm). The in-beam calibration of the setup (section 4.1) was performed using ^{50}Ti beam and an ^{170}Er target to produce ^{215}Th. The excitation function of this reaction is shown in figure 5.1
The ^{152}Eu and ^{133}Ba sources were used for the calibration of the germanium clover. The energy range between 120 to 1410 keV is covered by the γ-ray activity of the ^{152}Eu source. The low energy range between 30 and 390 keV is covered by γ and X-ray activity of the ^{133}Ba source. The combination of these two sources provides a good calibration of the germanium clover in the energy range of 30 to 1410 keV.

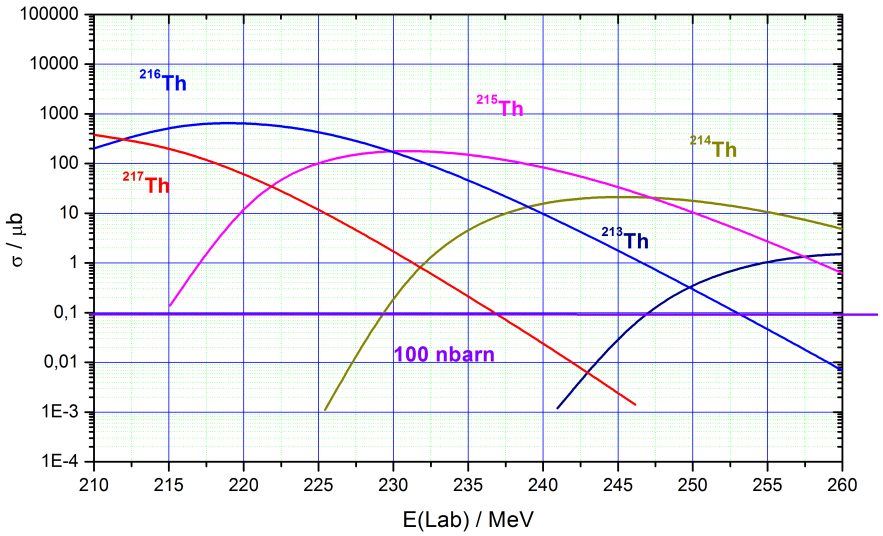

Figure 5.1: Production cross section in µbarn for different isotopes of Th calculated with HIVAP code.

5.1.1 PSSD calibration

The PSSD, described in section 2.4.2, is used for the implantation of ER and their α decay. Several different calibrations of this detector are performed and discussed in the following sections.

"Ballistic" calibration

The total height of the signal of the particle in the PSSD is the sum of the preamplified signals collected on the top (x) and bottom (35mm - x) of the detector (section 2.4.2). Consequently the height of the signal of an α particle of a specific energy depends on the position inside the strip. A systematical shift of the signal height over the surface of the strip can be observed when the signal height ($E_c h$) is plotted (figure 5.2) as a function of its position in the strip (Q_{ytop}/E_α). The shift is corrected with a so called "ballistic" calibration.
A well separated α peak (^{215}Ac, see figure 5.2) and a mean value ("correction value") to which the signal height over the strip surface will be restored are chosen. The mean value depends on the characteristics of the signal height in a given strip (table 5.1). The difference between the mean of the α decay in channels and the correction value is plotted versus the ratio between the charge collected on the top (bottom) of the strip and the signal height of the α particle collected in the

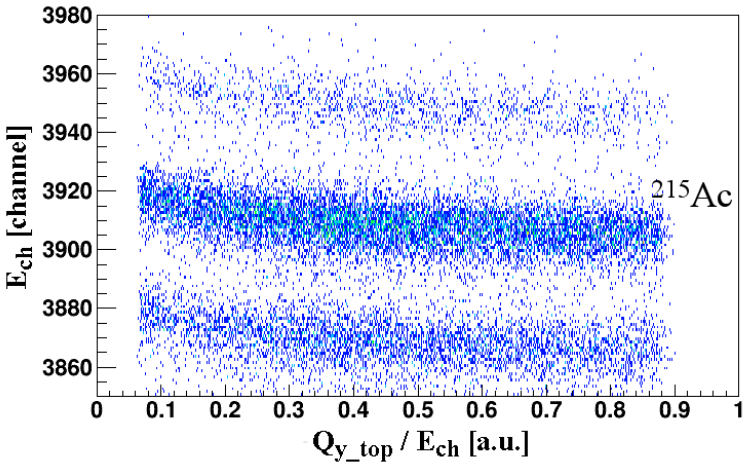

Figure 5.2: Distribution of the signal height of α particles as a function of position in strip nb.2. Zoom is made for better visibility in the region of ^{215}Ac, two additional peaks can be seen. The ratio between the charge collected on top of the strip (Q_{y_top}) and the signal height of the α particle ($E_ch = Q_{y\_top} + Q_{y\_bott}$) is shown on the X-axis, while the Y-axis shows the signal height of the α collected in this strip.

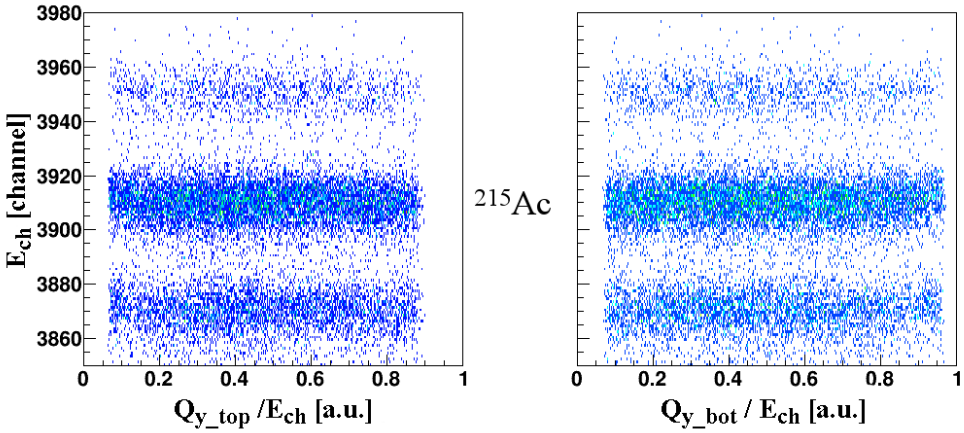

Figure 5.3: Distribution of the signal height of an α particle, corrected with "ballistic" calibration, over the surface of strip nb.2. The zoom is made for better visibility in the region of ^{215}Ac. The X-axis of the figure on the left (right) displays the ratio between the charge collected on the top (bottom) of the strip and the signal height of the α particle collected in the strip. The Y-axis contains the signal height of the α collected in this strip and corrected with "ballistic" calibration.

strip. The value of the shift (e_{shift}) is obtained from the following equation:

$$e_{shift} = a\, Q^2_{y\_top(bottom)} + b\, Q_{y\_top(bottom)} + c \tag{5.1}$$

where $Q_{y\_top(bottom)}$ is the charge collected on the top (bottom) of the strip and a, b and c are the parameters obtained from the fit. Finally, the signal height is corrected by the obtained shift value ($E = E_{ch} - e_{shift}$), reducing the dependance of the signal height on the position in the strip. A corrected distribution of the signal height over the surface of the strip can be seen in figure 5.3. The obtained results can be seen in table 5.1. This procedure provides a better energy resolution by reducing the width of the α peak in each strip of the detector.

Strip	$E_{ch_{raw}}$ (Δ) [chan.]	Res. to: [chan.]	$E_{ch_{top}}$ (Δ) [chan.]	$E_{ch_{bot}}$ (Δ) [chan.]
1	3914 (40)	3915	3915.6 (25)	3915.6 (25)
2	3909 (40)	3910	3910.2 (15)	3910.1 (15)
3	3910 (30)	3915	3914.5 (20)	3914.5 (20)
4	3914 (35)	3915	3915.2 (20)	3915.2 (25)
5	3919 (30)	3920	3920.0 (20)	3920.2 (15)
6	3919 (30)	3920	3920.0 (15)	3920.0 (20)
7	3913 (40)	3915	3915.1 (15)	3915.0 (20)
8	3918 (30)	3915	3915.9 (15)	3916.0 (15)
9	3925 (30)	3920	3920.4 (15)	3920.5 (20)
10	3914 (30)	3920	3919.7 (20)	3919.7 (20)
11	3921 (40)	3920	3920.3 (20)	3920.2 (20)
12	3912 (30)	3915	3914.7 (15)	3914.8 (15)
13	3910 (30)	3915	3914.4 (15)	3914.4 (15)
14	3911 (30)	3915	3914.4 (20)	3914.5 (15)
15	3913 (40)	3915	3914.9 (20)	3914.9 (20)

Table 5.1: The table presents the impact of the "ballistic" calibration on the α spectra. The "$E_{\alpha_{raw}}$" is the position of the mean of the ^{215}Ac peak before the calibration. "Res. to:" refers to which channel the mean value is supposed to be restored. The last two columns present the results of the calibration when the top (bottom) charge collection is used to perform the calibration. Δ represents the maximal widths of the α peak of ^{215}Ac over the surface of a strip.

In-beam α calibration

The signal heights of the α particles have been aligned over the surface of each strip using the "ballistic" calibration (section 5.1.1). In addition an α energy calibration is performed to align the strips of the detector and convert the output

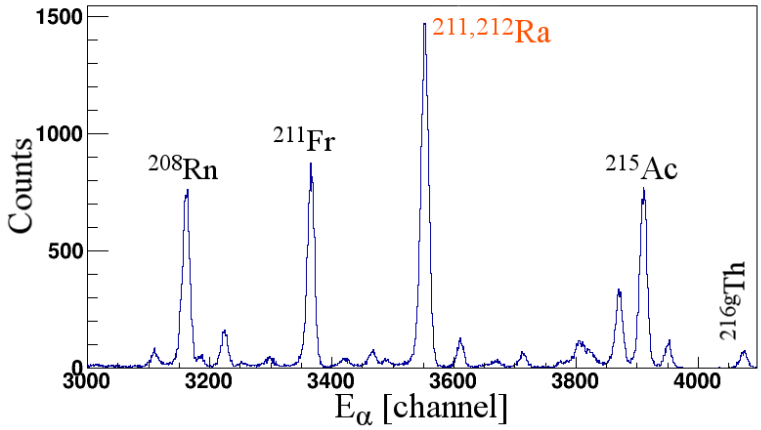

Figure 5.4: Non calibrated α spectra in strip nb.2 corrected by "ballistic" calibration. Indicated α decays were used for energy calibration, the doublet transition of $^{211,212}Ra$ was not used. Identification of the rest of the α decays can be found in table 5.2.

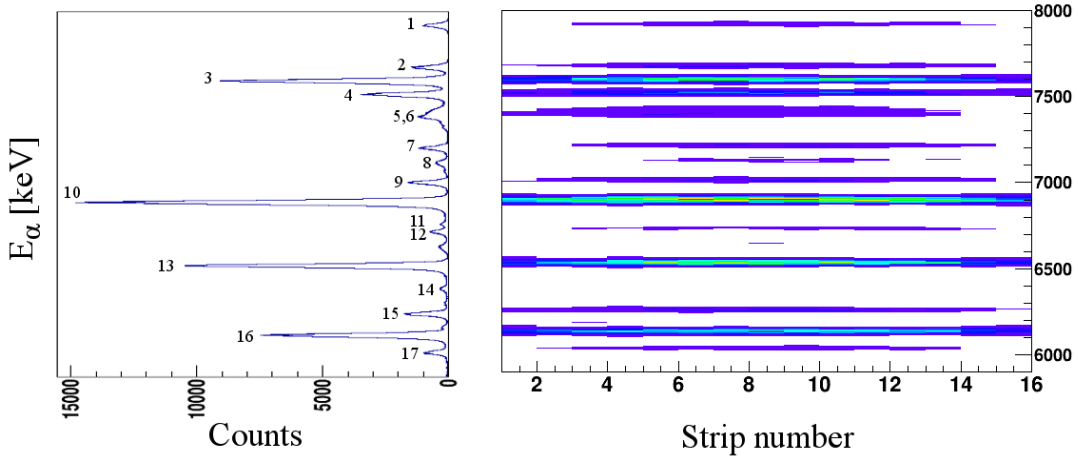

Figure 5.5: Left: Total calibrated α energy spectra summed over all 15 strips of the PSSD. Right: Calibrated α energy spectra with respect to the strip number of the PSSD. Indicated α transitions can be found in table 5.2.

from channels to energy units (keV).
For each strip separately the most intense α decay lines (figure 5.4) are identified and the mean value of their position is retrieved from the non calibrated α spectra. Alpha decays of ^{208}Rn, ^{211}Fr, ^{215}Ac and ^{216g}Th are used for the calibration purpose. The decay of ^{211,212}Ra is not used due to the fact that it is a doublet (6909 (4) and 6899 (17) keV respectively), and there were enough individual α decays for a proper calibration. The α emission of ^{216g}Th has a low intensity, however its energy is the closest to the expected α energies of ^{258}Db and its daughters. Consequently it is beneficial to use this transition to improve the accuracy of the calibration in this energy range.

Peak	Element	E_α [keV]	FWHM [keV]	Lit. E_α [keV]
1	^{216g}Th*	7921	26	7923
2	^{214}Th	7680	25	7678
3	^{215}Ac*	7602	25	7600
4	^{215}Th	7524	25	7523
5	^{215}Th	7397	31	7392
6	^{214}Ac	7216	26	7215
7	^{214}Ra	7130	26	7135
8	^{214}Ac	7089	26	7080
9	^{210}Ra	7017	26	7016
10	^{211,212}Ra	6903	28	^{211}Ra-6907 ^{212}Ra-6898
11	^{213}Fr	6777	24	6775
12	^{213}Ra	6734	24	6731
13	^{211}Fr*	6539	24	6537
14	^{206}Rn	6262	24	6259
15	^{212}Fr	6187	26	6183
16	^{207,208}Rn*	6139	26	^{207}Rn-6131 ^{208}Rn-6140
17	^{209}Rn	6039	24	6039
18	^{207}At	5757	24	5758

Table 5.2: Identified α lines with energy and FWHM are presented, the transitions are indicated in figure 5.5. The peaks used for calibration are marked with a star (*). The value of the α particle energy in the literature is indicated as reference.

The results of the linear calibration can be found in figure 5.5. The summed α spectrum of all working strips (15 strips) of the PSSD is plotted in the figure on the left hand side. The figure on the right hand side shows the energy distribution as a function of the strip number. The obtained energies and the FWHM of identified

transitions (indicated in figure 5.5) can be found in table 5.2.
A total energy resolution of 26 keV FWHM was obtained from this calibration.

Position calibrations

The position information (section 2.3) is required to perform correlations between the ER registered in the HE branch and the α particles registered in LE branch. Consequently it is necessary to have a precise position calibration of the PSSD. A region of overlap between the energy range of the low (LE) and high (HE) energy branch has to be identified. In this case the selected energy range lies between 6000-8000 keV which corresponds to channels 3000 to 4000 in LE and channels 140 to 200 in the HE branch respectively. Alpha decays which trigger both energy branches (LE and HE) at the same time are identified in anticoincidence with the TOF signals, in the selected energy range of the PSSD or in the pause of the beam. The dependance of the charge collected on top (bottom) of the strip in HE branch with respect to the charge collected on the top (bottom) of the strip in LE branch is plotted in a two dimensional plot. The parameters obtained from the linear fit of this plot are used to calculate the correction of the position in the HE branch. Results of the calibration (black spectra) can be seen in figure 5.6.

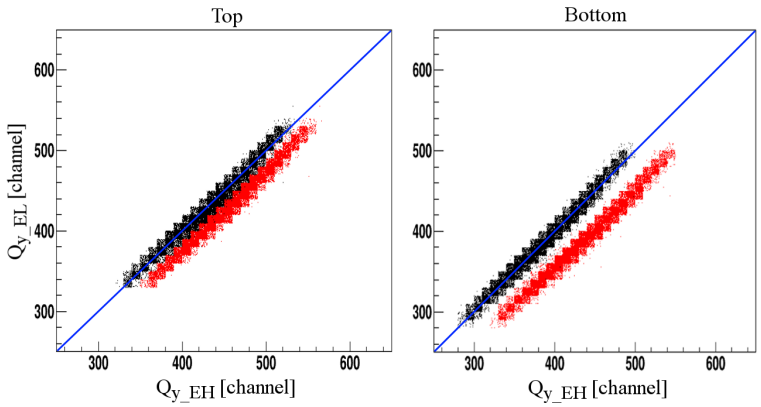

Figure 5.6: Left (right): Two dimensional histogram presenting the charge collected on the top (bottom) of the strip nb. 9 in HE branch on the X-axis, and in LE branch on the Y-axis. The red (black) dots present the non calibrated (calibrated) spectra. The blue line serves to guide the eye, it represents a condition that the charge collected in the LE and HE are exactly the same.

The quality of the calibration can be inspected by performing correlations between the ER and the α particles. For this purpose the short lived (26 ms) ^{216g}Th decay is used. Due to its short life, the probability of random correlations between the

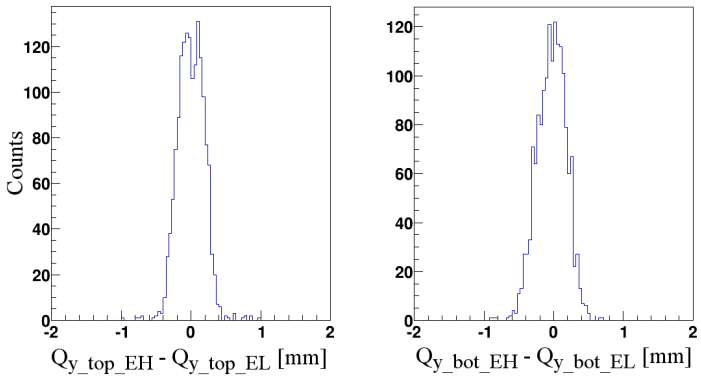

Figure 5.7: Left (right): Difference in charge collected on top (bottom) of strip nb.6 between the EH and EL for ER-α correlated events. The correlations are done for the short lived ^{216g}Th.

	Top charge collection			Bottom charge collection		
Strip	Nb. ev.	Mean [mm]	FWHM [mm]	Nb. ev.	Mean [mm]	FWHM [mm]
1	302	-0.04	2.4	302	0.03	1.2
2	638	-0.04	2.1	638	-0.02	1.6
3	526	-0.04	2.4	526	0.00	1.2
4	1031	0.01	2.4	1031	-0.03	1.6
5	1273	-0.03	2.4	1273	0.00	1.3
6	1577	0.00	1.2	1577	0.00	1.2
7	1377	-0.07	2.4	1377	0.00	1.8
8	1553	-0.02	1.2	1553	-0.10	2.4
9	844	-0.01	2.4	844	0.03	1.8
10	1271	0.01	1.2	1271	0.00	1.2
11	1099	0.03	2.4	1099	0.00	1.4
12	1051	-0.01	1.6	1051	0.00	1.3
13	781	0.00	2.4	781	0.00	1.2
14	671	0.04	1.2	671	0.00	2.1
15	528	-0.02	2.2	528	0.00	1.2

Table 5.3: Position calibration results for both top and bottom charge collection. The column "Nb. events" shows the number of correlated events in the strip for charge collected on top (bottom) of the strip.

events in the HE branch, which are not ER, and the α particles are minimal. The correlation was performed under the condition that the position of the ER and the α particle found in the same strip are within ± 1 mm (2 mm FWHM) in the Y direction of each other.
The position and shape of the centroid obtained by plotting the difference between the charge collected on top (bottom) position for the implanted nucleus and its α decay gives the quality of the calibration. The calibration is good if the centroid is symmetric around 0 (figure 5.7). The results are given in table 5.3.
The range in which the position correlations should be performed is dictated by the FWHM of the centroid. Resolution for the position of the charge collected on the bottom of the strip of ± 0.5 mm (1 mm FWHM) is slightly better than the one obtained for the charge collected on the top of the strip of ± 1 mm (2 mm FWHM) (table 5.3). Consequently, a range of 2 mm FWHM will be used for top position, and 1 mm FWHM for bottom position in the data analysis, unless specified differently.

5.1.2 BOX detector calibration

The box detector measure the remaining energy of the particles escaping the PSSD (α and conversion electrons 2.4.2). Consequently the total energy of an escaped α particle corresponds to the sum of the signals from the PSSD and BOX detectors. Thus, in order to perform the calibration of the BOX it is necessary to look at the sum of the non-calibrated spectra from these detectors, where the PSSD signals are corrected with the "ballistic" calibration.

Element	E_α [keV]	FWHM [keV]	Lit. E_α [keV]
^{216g}Th	7914	80	7923.0
^{215}Ac*	7596	78	7600.0
^{215}Th	7518	59	7523.0
^{215}Th	7399	59	7392.0
^{211,212}Ra*	6890	82	^{211}Ra-6907.0 ^{212}Ra-6898.0
^{211}Fr*	6520	71	6537.0
^{208}Rn*	6111	85	6140.1

Table 5.4: Energy and FWHM of identified summed α lines in the BOX detectors and PSSD are listed. The peaks used for the calibration are marked with a star (*). The literature value for the α energy is given in the last column.

An identification of the α transitions is performed and their mean value is retrieved. This enables calibration of the summed α spectra of the PSSD and BOX detectors.

Since the PSSD was previously calibrated (5.1.1) it is possible to remove the PSSD calibrated α energy part from the summed calibrated spectra, leaving the BOX part of the α spectra. This value is then plotted against the non calibrated α spectra of the BOX detector and fitted with a first order polynomial. The obtained parameters are used for BOX detector calibration. Calibration results can be seen in figure 5.8 on the bottom, and table 5.4.

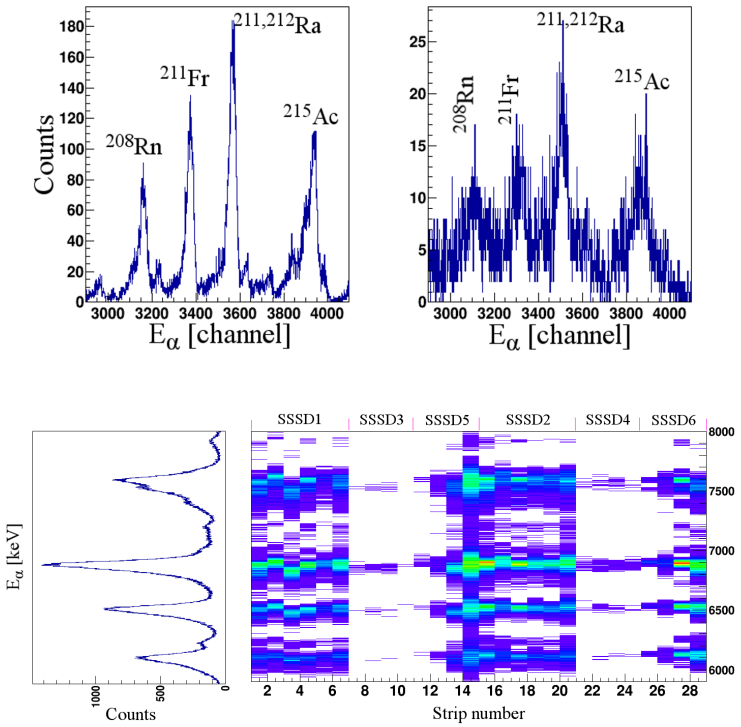

Figure 5.8: Top: Non calibrated α spectra from BOX detectors collected in strip nb.18 (8) on the left (right) plot summed with the α signals collected in the PSSD (position corrected). Identified α transitions are indicated.
Bottom: Calibrated α energy spectra of the BOX detectors summed with the calibrated α energy of the PSSD. Left: the sum of the α energy over all 28 strips of the BOX detectors. Right: α energy in dependence of the strip number. Different SSSD's are indicated on the top of the figure, their position can be seen in figure 2.20.

5.1.3 Germanium detector calibration

The calibration of the germanium clover is performed using the two sources of ^{152}Eu and ^{133}Ba emitting γ and X-rays in an energy range of 30 to 1410 keV (section 5.1).
The centroid of each of the identified γ and X-ray transition is retrieved for each crystal separately. The non-linearity of the amplifier module causes slightly different amplifications in lower and higher energy regions of the spectra which results in a need for two separate calibrations. The separation is performed at channel 3000 (figure 5.10).
The two sets of parameters are used for calibration of the germanium detector. Results of the calibration can be seen in figure 5.11 and in table 5.5.

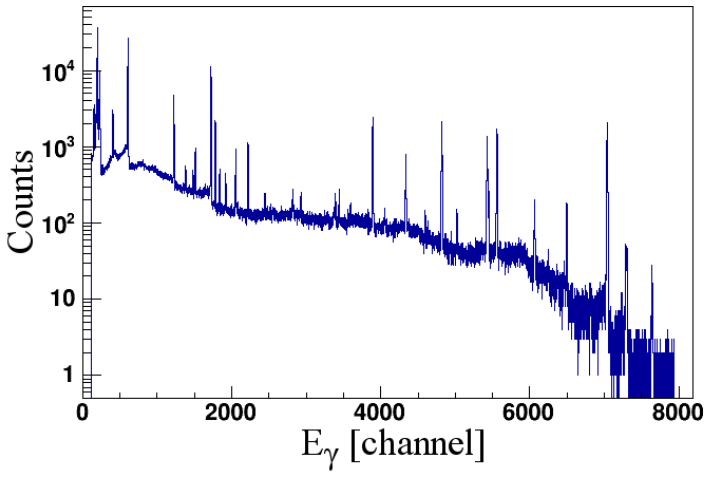

Figure 5.9: Non calibrated γ spectra of ^{152}Eu and ^{133}Ba observed in crystal nb. 1 of the germanium clover.

The efficiency of the Germanium detector was measured during an previous experiment at SHIP. The geometrical configuration of the set up was not changed and the efficiency curve obtained in [106] can be used (figure 5.12).

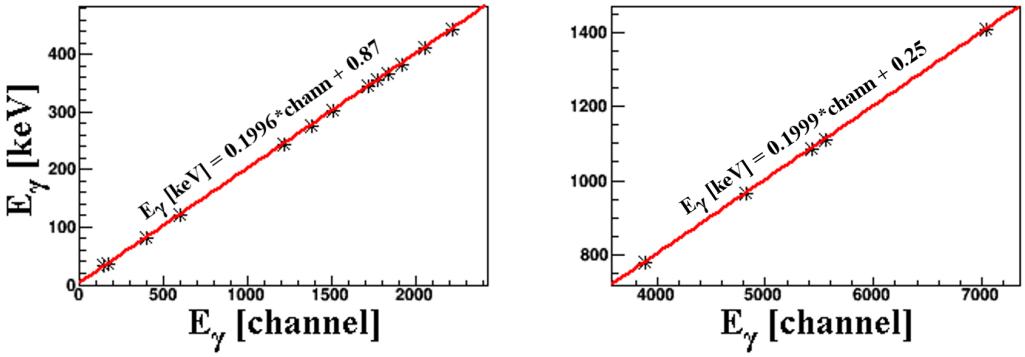

Figure 5.10: Example of the two separate fits (parameters are indicated in the figure) for crystal nb.1 of germanium clover. The spectrum is separated at channel 3000. The low energy spectrum contains the γ-ray transitions from ^{152}Eu and X-rays from ^{133}Ba source. The high energy spectrum contains the high energy γ transitions from the ^{152}Eu source.

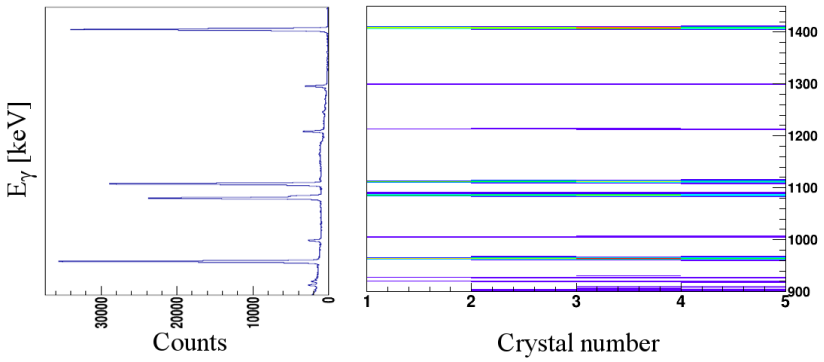

Figure 5.11: Left: Calibrated γ spectrum summed over all four crystals of the germanium clover. Right: Calibrated γ energy spectrum for each crystal. Zoom on both figures is made between 900 and 1450 keV for better visibility.

^{152}Eu			^{133}Ba		
E_γ [keV]	FWHM [keV]	Lit. E_γ [keV]	E [keV]	FWHM [keV]	Lit. E [keV]
122.3	2.1	121.8	31.6	3.2	32.194
244.7	2.4	244.7	35.8	4.1	36.480
344.1	2.4	344.3	81.5	1.9	81.000
367.7	2.4	367.7	273.2	4.7	276.400
411.2	2.4	411.2	302.6	2.6	302.900
444.0	2.6	444.1	355.7	2.4	356.000
778.8	2.6	779.0	383.5	2.4	383.800
867.3	2.6	867.4			
964.0	2.6	964.1			
1085.7	2.6	1085.8			
1112.0	2.8	1112.1			
1407.9	3.1	1408.1			

Table 5.5: Energies of the ^{152}Eu γ-rays and ^{133}Ba γ and X-rays obtained after the calibration and summing of the spectra from all four crystals of the clover are presented. The values of the FWHM are given as well as the literature values for the corresponding transitions.

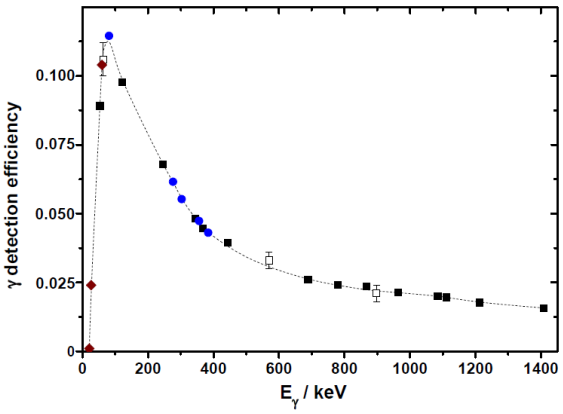

Figure 5.12: Particle-γ coincidence detection efficiency curve of the germanium clover used at SHIP. Relative efficiencies were obtained using ^{133}Ba (full circles), ^{152}Eu (full squares) and ^{241}Am (full diamonds); open squares are obtained from in-beam measurements using ^{211}Po and ^{212m}Ac transitions, details can be found in [106]; the dashed line represents a smoothed connection of the data points. Figure adopted from [106].

5.2 Spectroscopy of ^{258}Db

The ^{258}Db was previously studied using the velocity filter SHIP at GSI by F. P. Heßberger [96, 98] and B. Streicher [100], and at Lawrence Berkeley National Laboratory using the Berkeley gas filled separator by J. Gates [101].
Previous studies of ^{258}Db left some open questions and the performed experiment had as a goal to answer them. It was indicated both through direct production of ^{258}Db and indirect production form the α decay of ^{261}Bh that two long-living states exist and decay by α emission and/or electron capture. Additionally a β decay of ^{258}Db to ^{258}Rf was observed. From a separate experiment the ^{258}Rf α branch was calculated to be 30% [107].
Two γ-ray transitions with energies 221.5 and 156.8 keV were found in coincidence with the α decay of ^{258}Db. The 221.5 keV line was assigned to the decay of long lived state, the second γ-ray with 156.8 keV was not assigned due to the large error bar on the half life.
The daughter element ^{254}Lr was additionally studied in a direct reaction at SHIP by S. Antalić and collaborators [108] (table 5.6). They have proposed a partial level scheme for ^{250}Md. However, they have not been able to assign the γ-ray transition of 165.3 keV.
The results of these studies are summarized in table 5.6. A schematic representation of the ^{258}Db decay chain is given in figure 5.13.
In this study ^{258}Db was directly produced through the 1n channel of the fusion evaporation reaction using a ^{50}Ti beam on a ^{209}Bi target. The measured excitation function can be seen in figure 4.13.

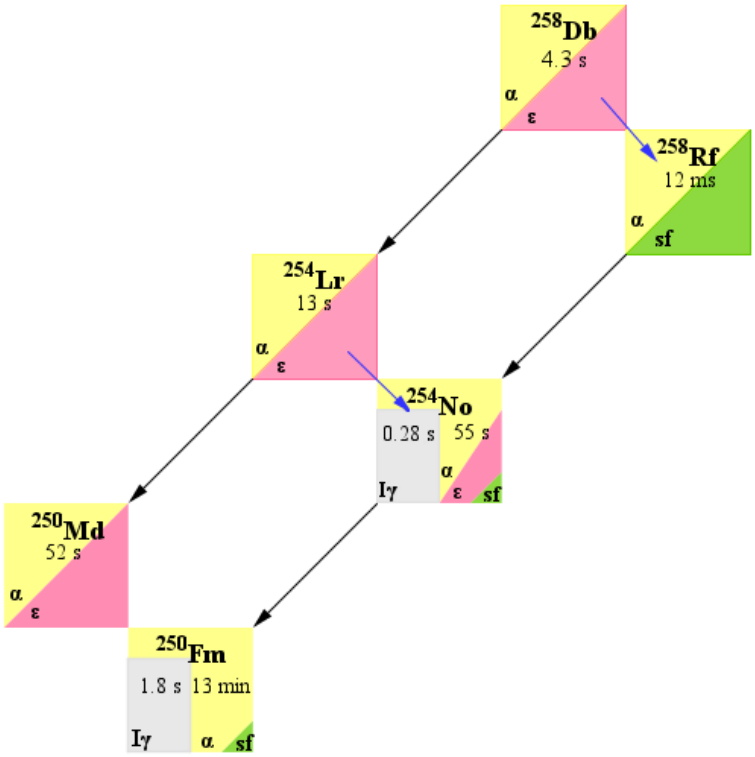

Figure 5.13: Schematic representation of the ^{258}Db decay chain.

Isotope	E_α [keV]	$T_{\alpha_{1/2}}$ [s]	b_α [%]	b_{EC} [%]	b_{SF} [%]
^{258}Db	9089 (10) 9109 (5) 9155 (20) 9166 (10) 9280 (20) 9353 (15)	4.3±0.5	$0.67^{+0.05}_{-0.09}$	$0.33^{+0.09}_{-0.05}$	
^{258}Rf	9050 (30)	$14.7^{+1.2}_{-1.0}$	4		96
^{254}Lr	8408 (20) 8460 (20)	18.4±1.8	0.78±0.22	0.22±0.06	
^{254}No	8100 (30)	55±10	90±4	10±4	
^{250}Md	7750 7820	52±6	7±3	93±3	
^{250}Fm	7396 (15) 7435 (11)	1800±180	>90	<10	

Table 5.6: Summarized spectroscopic data of former experiments performed on ^{258}Db, ^{258}Rf, their daughters ^{254}Lr and ^{254}No, and granddaughters ^{250}Md and ^{250}Fm. Granddaughter information adopted from [102].

5.2.1 Correlation gates

The structure of the ^{258}Db and its daughters was probed with the generic correlation method. Proper position, time and energy gates are necessary to perform the spectroscopy studies, as it was described previously in section 4.2.1.

Position correlations require that the ER and its decay emissions are found in the same strip of the PSSD, in a selected position window in Top and Bottom direction. The position window applied on the top will be ±1 mm and on the bottom ±0.5 mm. This position window was chosen according to the position calibration results (section 5.1.1) and correlation attempts where the optimal ratio between the data and background was obtained.

Time windows are chosen depending on the correlation which is studied (section 4.2.1). The applied time correlation windows are indicated throughout the text.
Energy gates set on the α particles and/or γ-rays are indicated throughout the text.

Selection of the ER is performed using the method described in section 4.2.1. The reaction producing ^{215}Th is not ideal for this purpose as the mass difference with ^{258}Db is too large resulting in different Bρ and therefore different settings of the

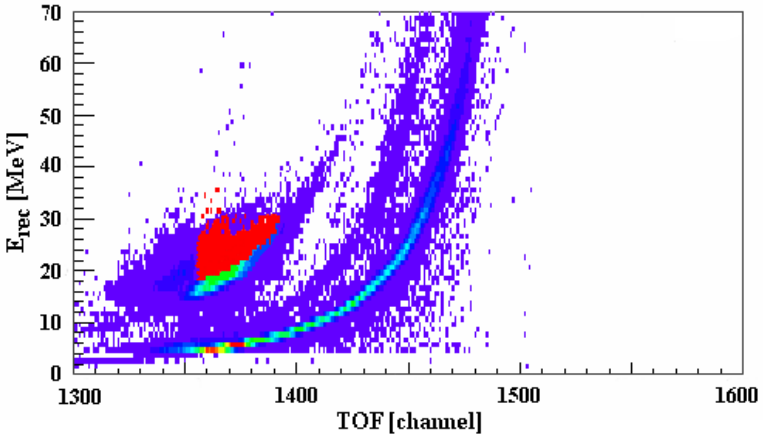

Figure 5.14: Plot of the ETOF matrix from the reaction ^{50}Ti on ^{208}Pb. The position of the ^{256}Rf ER correlated to fission fragments in a time window of 19 ms, are indicated in red on the top left part of the spectrum.

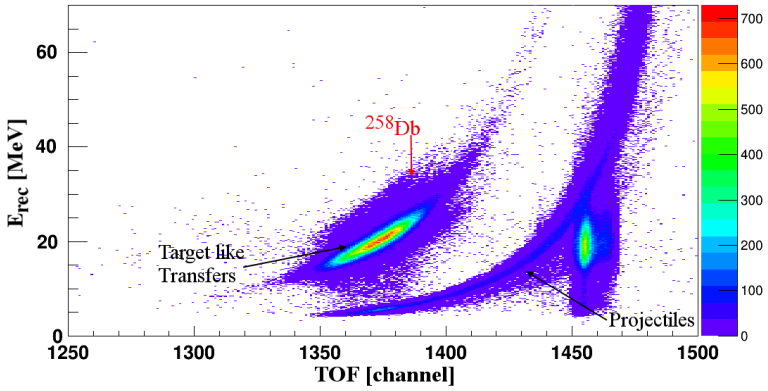

Figure 5.15: Plot of the ETOF matrix from the reaction ^{50}Ti on ^{209}Bi. Different mass regions are indicated. The mixture of ^{258}Db nuclei with the transfer products is visible. The vertical line at channel 1450 is due to readjustments of the voltage of the TOF detector during the experiment. Similar spectra can be made for the other two TOF signals.

spectrometer. A part of the beam time was dedicated to the production of ^{256}Rf in a reaction ^{208}Pb(^{50}Ti,2n)^{256}Rf. This isotope is closer in mass to ^{258}Db than ^{215}Th and therefore makes a better candidate for determining the gate on the ETOF matrix. Moreover, the ^{256}Rf has a fission branch of about 98 % with a half life of 6.2 ms. The position of the ER of ^{256}Rf in the ETOF matrix is determined from the correlations performed between the implanted ER of ^{256}Rf and the fission fragments in a small time window (19 ms, corresponding to 3 half lives of ^{256}Rf). The half life of ^{256}Rf is sufficiently short to avoid random correlations. The fission fragments which follow the implantation event are emitted shortly after the implantation. Therefore the probability to implant a "bad" ER in the same pixel before the fission occurs is much lower than in the case of long lived isotopes.
The probable position of ^{258}Db nuclei in the ETOF matrix is now known (figure 5.15) and can be used to set a gate for the analysis.

5.2.2 Decay of ^{258}Db: structure study

The structure of ^{258}Db and its daughters is probed by studying the α, γ and X-ray decays. The identification of the isotopes and the decay chains is done through the α decay measurement.
The energy distribution of the collected α transitions in the PSSD, in the range of 7.5 to 9.5 MeV can be seen in figure 5.16. The figure on the top shows all α decays gathered in the stop detector in anticoincidence with TOF signals for the complete cycle (15 ms beam off + 5 ms beam on). The bottom figure shows the α decays gathered in "beam off" periods (section 2.2.2). Significant increase of the background can be observed for the data gathered in the complete cycle compared to the data gathered in the beam off cycle. Therefore the decays gathered in beam off periods were primarily used for the analysis purposes and the results were double checked with the anti-coincidence data.
The identification of the observed α decays is shown in figure 5.16. The presence of ^{253}Lr and its daughter product ^{249}Md indicates that a certain amount of ^{257}Db (2n channel) was produced and implanted in the PSSD. The energy of the α decay of ^{257}Db (section 4.2) is close to the energies of the α lines of ^{258}Db. Consequently, the low intensity α decay of ^{257}Db is not well separated from the α decay of ^{258}Db. Transfer products such as ^{212}At, indicated in the figure, ^{211}Po (E_α<7.5 MeV) and others are visible in the data.

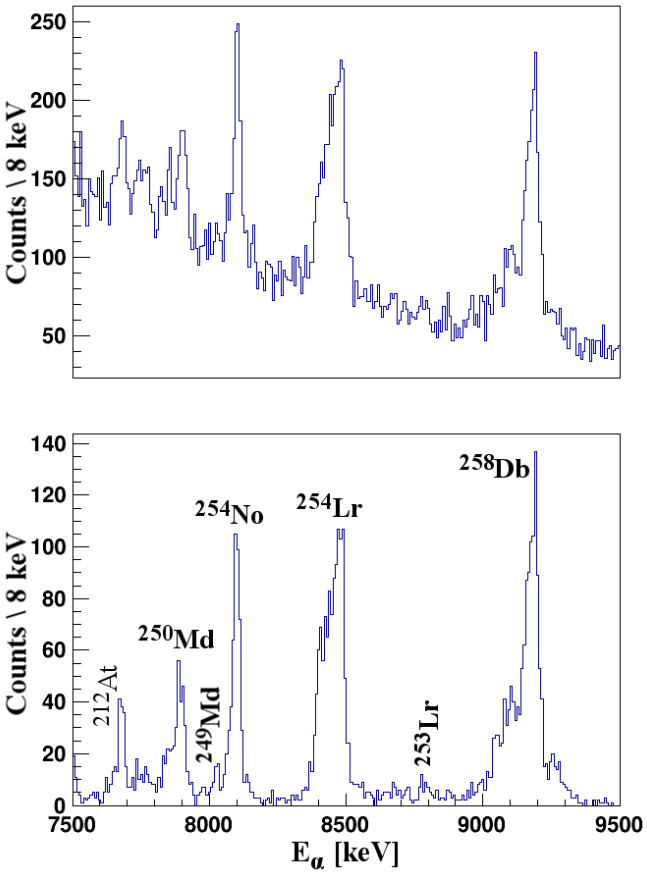

Figure 5.16: Top (Bottom): Total α decay gathered in the stop detector in anticoincidence with TOF (beam pause).

Structure of ^{258}Db

The results from the recoil-α correlations performed in a time window of 22 s ($5xT_{1/2}$) and 13 s ($3xT_{1/2}$, see table 5.6), used to probe the structure of ^{258}Db, are discussed in the following text.

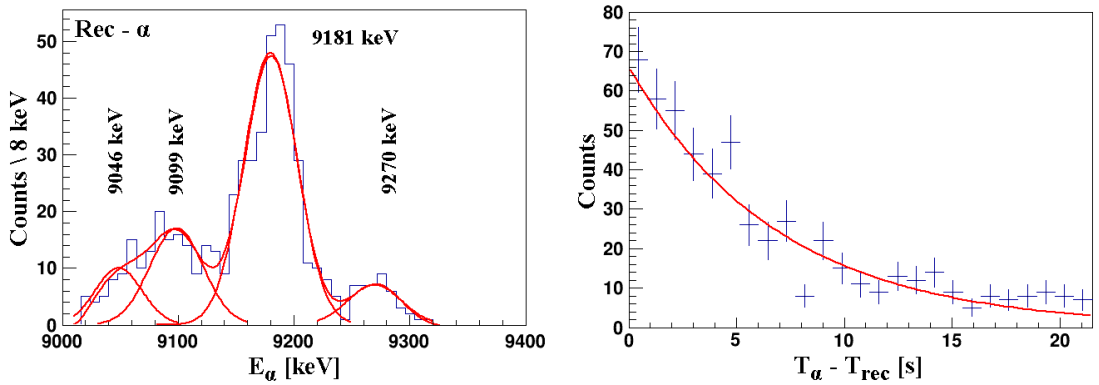

Figure 5.17: Left: Alpha energy spectrum obtained from recoil-α correlations in a time window of 22 s. Right: Decay curve for an α energy range between 9.0 and 9.4 MeV obtained from recoil-α correlations performed in a 22 s time window during the beam off period.

Two Gaussian shaped α decays with energies 9181 (23) and 9270 (23) keV can be observed in the spectrum of figure 5.17, on the left hand side. The region below 9.15 MeV shows a broad distribution which indicates two α decays when a fit is performed with a constrained sigma value of 24 keV. However a clear separation can not be made and the broadness of the distribution can be a consequence of electron summing. Additionally, a shoulder can be distinguished on the left side of the 9181 (23) keV α decay. Since the PSSD has a resolution of 26 keV FWHM for a single α peak, such a behavior indicates a summing of the α decay energy with conversion electrons [33].
If the 9046 (23) keV line is considered as an α decay it can also belong to the α decay of ^{258}Rf [107], which is produced by the β decay of ^{258}Db. The electron capture branching ratio of ^{258}Db was previously reported on the basis of the observed fission activity [96].
The analysis of the fission data, from this experiment, performed by F.P. Heßberger reveals fission fragments belonging to ^{258}Rf observed in correlations with conversion electrons and X-rays [109].
The following analysis of the α chains will try to determine if the α decay of ^{258}Rf is visible as well.
The search for escaped α particles in correlation (time window of 22 s) with recoil

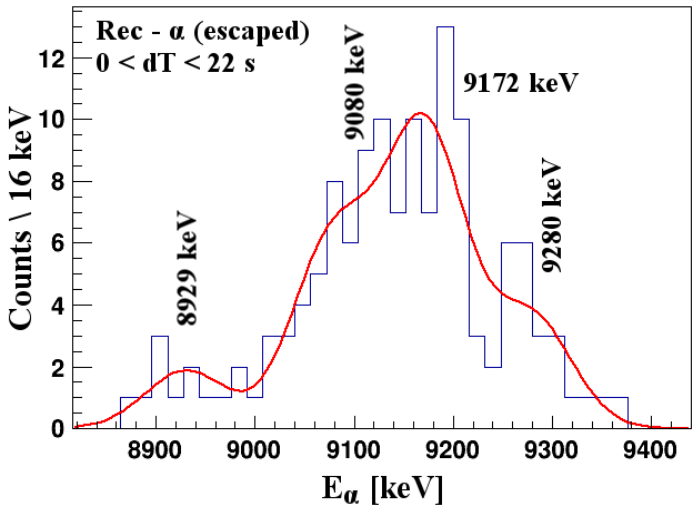

Figure 5.18: Alpha decays registered in the BOX detector correlated to recoil events in the PSSD in a time window of 22 s.

			$T_{1/2}$ [s]	
E_α [keV]	i_α	$E_{\alpha_{range}}$ [MeV]	$\Delta T < 22$ s	$\Delta T < 13$ s
All	1.00	9.00 - 9.36	4.3±0.5	4.4±0.4
9046 (23)	0.13	9.00 - 9.05		
		9.00 - 9.07		
9099 (23)	0.21	9.05 - 9.15	5.0±0.5	4.1±0.6
		9.03 - 9.17	4.8±0.5	4.4±0.6
9181 (23)	0.56	9.15 - 9.25	3.8±0.4	3.4±0.4
		9.13 - 9.27	3.1±0.3	3.5±0.4
9270 (23)	0.10	9.25 - 9.36		
		9.23 - 9.36		
9046 + 9099		9.00 - 9.15	4.6±0.5	4.6±0.7
		9.00 - 9.17	4.7±0.5	4.4±0.6
9181 + 9270		9.15 - 9.36	3.8±0.4	3.4±0.4
		9.13 - 9.36	4.0±0.4	3.5±0.4

Table 5.7: Half lives obtained for different energy regions and two different time windows (22 and 13 s). Due to low statistics some half lives were not determined. The first column indicates the energy of the decay which half life is determined, while the second column indicates the intensity of the transition. $\Delta T = T_\alpha$-T_{rec}.

events reveals an amount of 144 (18% of the total implanted events) events in beam off (figure 5.18), and 219 (17 %) events in beam on+off periods. Two α decays with energies of 9280 (42) keV and 9172 (42) keV can be identified as well as a broad distribution in the range between 9.00 and 9.15 keV, this is in agreement with the α decays found in the implantation detector. Finally, the α decay of ^{257}Db with an energy of 8929 (42) keV is visible as well.
A value of 4.4±0.4 s was obtained for the global half life of the α decays of ^{258}Db in the energy range of 9.0 to 9.4 MeV (figure 5.17, on the right hand side). This value is in agreement with previously reported ones in [98, 101].
The half lives of individual α decays of ^{258}Db were investigated and an indication of two different half lives was found. The obtained results are reported in table 5.7. The α decays with higher energies, above 9.15 MeV, are characterized by a shorter half life of 3.5±0.4 s. The lower energy, below 9.15 MeV, α decays display a longer half life of 4.5±0.6 s. These results further support the conclusions made in [98] of the existence of two α-decaying states in ^{258}Db.

Structure of the (grand) daughter nuclei

The structure of the daughter and the grand daughter isotopes is obtained from the generic correlations and correlations with γ-rays. The time and energy windows used will be indicated in the text.
A general overview of α-α correlations is given in figure 5.19. This figure is obtained for a time window of 400 s due to differences in the half lives (table 5.6) of the produced isotopes. It has to be taken into account that increasing the time correlation window increases the amount of random correlations. Figure a) (c)) shows the energy distribution of the daughter (mother) α decays. Figure 5.19 b) shows the correlations between mother and daughter α transitions. The following correlations can be deduced:

- ^{258}Db -> ^{254}Lr
- ^{258}Db -> ^{254}No
- ^{254}Lr -> ^{250}Md
- ^{257}Db -> ^{253}Lr
- ^{253}Lr -> ^{249}Md
- ^{249}Md -> ^{245}Es

The α decay chain of ^{257}Db is visible as well.
Detailed analysis, with time windows adjusted to the search, is performed and the results are discussed in the following section.

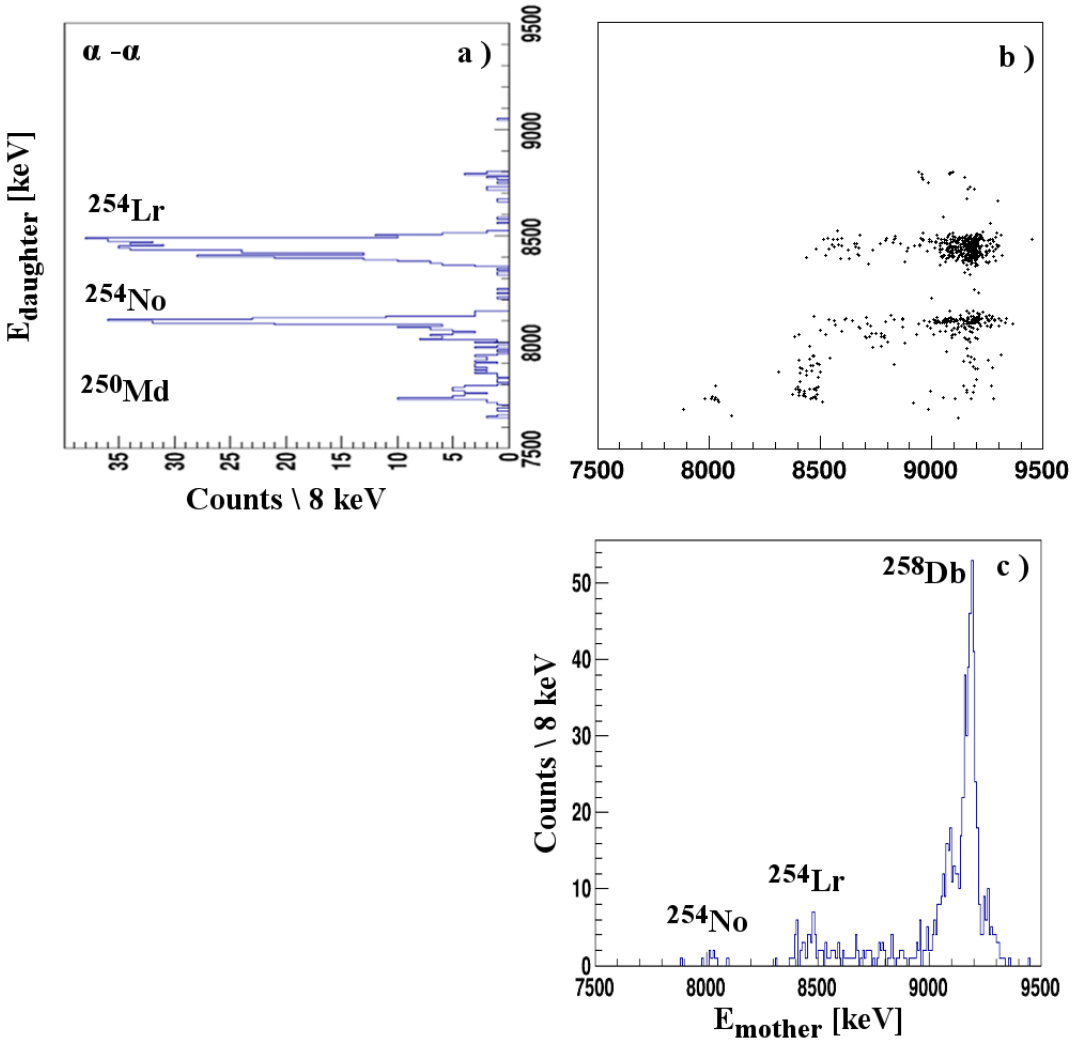

Figure 5.19: The α-α correlations were performed in a time window of 400 s in the pause of the beam. Identified α transitions are indicated.
a) Alpha energy of the daughter nucleus. It is the projection of figure b) on the Y-axis. b) Alpha energy of the daughter nucleus in dependance on the α energy of the mother nucleus. c) Alpha energy of the mother nucleus. It is the projection of figure b) on the X-axis.

^{254}Lr and ^{254}No

The second generation α decays belong to ^{254}Lr and ^{254}No isotopes. The structure of these isotopes is obtained from the α-α correlations to the first generation α decays, or from the recoil-α-α correlations. However, to determine the fine structure of these isotopes complementary information from γ and X-rays are necessary.
Time windows of 92 and 55 s were used for the study of ^{254}Lr, corresponding to 5x$T_{1/2}$ and 3x$T_{1/2}$ of ^{254}Lr (table 5.6). The study of ^{254}No was performed in time windows of 275 and 165 s corresponding to 5x$T_{1/2}$ and 3x$T_{1/2}$ of ^{254}No (table 5.6).

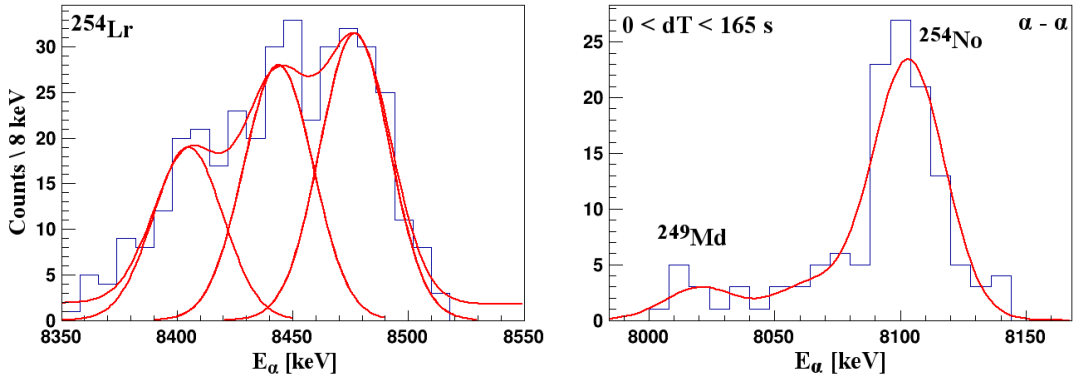

Figure 5.20: Left: Alpha decay transitions of ^{254}Lr found in correlations to mother nucleus in an energy range 9.0 to 9.3 MeV, with a time window of 92 s. Right: Alpha decay transitions of ^{254}No found in correlations to mother nucleus in an energy range 9.0 to 9.3 MeV, with a time window of 165 s.

The α decay of ^{254}No is a single line with an energy of 8102 (14) keV (figure 5.20, on the right hand side). A weak line of the third generation α decay of the ^{257}Db grand daughter ^{249}Md is visible on the left on the ^{254}No α peak in figure 5.23 on the right. Three α decays lines (figure 5.20, left) with energies 8405 (14), 8444 (14) and 8478 (14) keV can be assigned to ^{254}Lr, using the sigma value obtained from ^{254}No.
Differences in the correlations between ^{254}Lr and ^{254}No and the mother nucleus can be observed in figure 5.21.
^{254}Lr is produced from the α decay of ^{258}Db meaning that all ^{258}Db and ^{254}Lr α decays should be correlated among each other. The purple curve in figure 5.21 indicates that the energy region between 9.0 and 9.35 MeV is correlated to the α decays of ^{254}Lr in the energy range 8.35 to 8.55 MeV. Consequently one can conclude that all α decays in the energy range 9 to 9.35 MeV belong to the α

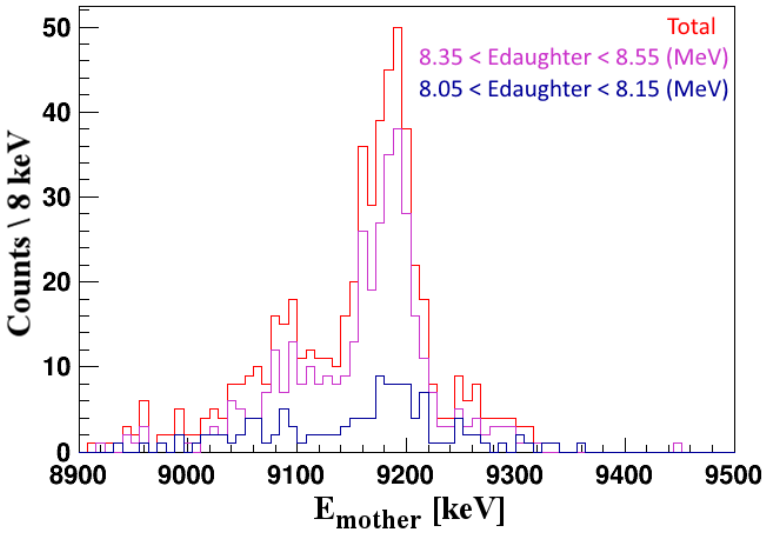

Figure 5.21: Alpha energy lines of the mother nucleus gated by the α decay of daughter nucleus. The red spectrum is the total, the purple is obtained from ^{254}Lr gates (8.35 to 8.55 MeV), while the blue spectrum comes from ^{254}No gate (8.05 to 8.15 MeV). A time window of 165 s was used.

decay of ^{258}Db.
^{254}No is produced in two ways:

- ^{258}Db -> EC -> ^{258}Rf -> α -> ^{254}No
- ^{258}Db -> α -> ^{254}Lr -> EC -> ^{254}No

Considering these two ways for the production of ^{254}No and the impossibility to correlate EC event, it can be expected that the ^{254}No α decay is in correlation with all ^{258}Db and ^{258}Rf α decays. However, an enhancement in the correlation between the ^{254}No and the ^{258}Rf α decays should still be visible. The α decay line with 9046 (23) keV energy, as previously mentioned in section 5.2.2, can belong to the decay of ^{258}Rf. The mother decay energies correlated to the α decay of ^{254}No are indicated in blue in figure 5.21. A slight enhancement in the correlations can be observed at 9060 and 9099 keV but not exactly at 9046 keV. Even though the 9046 (23) and 9060 (23) keV lines are inside the error bars of each other this does not give a clear indication that the α decay of ^{258}Rf is visible in coincidence with ^{254}No.
From the α decay data no firm conclusion can be drawn on the decay path to ^{254}No. Additional information such as the SF branch and electromagnetic transitions are needed to draw a conclusion.

The half life of ^{254}No was determined to 46±10 s in a time window of 165 s (figure 5.23 on the left hand side).

The structure of ^{254}Lr was probed using different energy gates on the α decays of ^{258}Db. The results of this investigation can be found in figure 5.22. Each color in

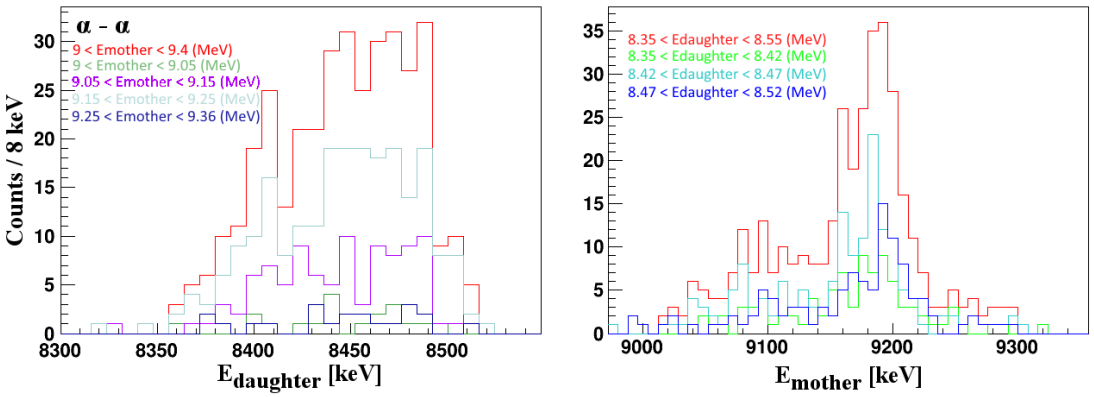

Figure 5.22: Left: ^{254}Lr α decay lines obtained from α - α correlations, with different energy gates applied on the decay of mother nucleus. Right: ^{258}Db α decay lines obtained from α - α correlations, with different energy gates applied on the decay of daughter nucleus. A time window of 92 s was used.

figure 5.22 on the left hand side, corresponds to the α events of ^{254}Lr correlated to a specific α decay of ^{258}Db. Similarly, each color in figure 5.22 on the right hand side, corresponds to the α events of ^{258}Db correlated to a specific α decay of ^{254}Lr. This gives an indication on the behavior of the daughter nucleus. The number of events observed in the α decays of ^{258}Db with energies 9046 (green line, figure on the left hand side) and 9270 keV (blue line, figure on the left hand side) is low (a total of 90 α events in a time window of 65 s), resulting in small amount of correlations to the α decays of the daughter nucleus ^{254}Lr. Consequently it is not possible to give firm conclusions on the observed coincidences between the different mother-daughter decays. The two decays with energies of 9099 (purple, figure on the left hand side) and 9181 keV (light blue, figure on the left hand side) are clearly correlated to all three α decays of ^{254}Lr. Similar conclusions can be drawn from the figure 5.22 on the right hand side.
Such a behavior would indicate different excited states of ^{254}Lr are populated by specific α decays of ^{258}Db. However, the observed α decays of ^{254}Lr are all emitted from the same level which is different from the levels populated by the decays of ^{258}Db. This would further mean that the levels of ^{254}Lr populated through the α decay of ^{258}Db deexcite by γ-ray or conversion electron emission. Consequently, the populated levels of ^{254}Lr can be determined only through the study of the

coincident γ-rays, which is discussed later in this chapter.

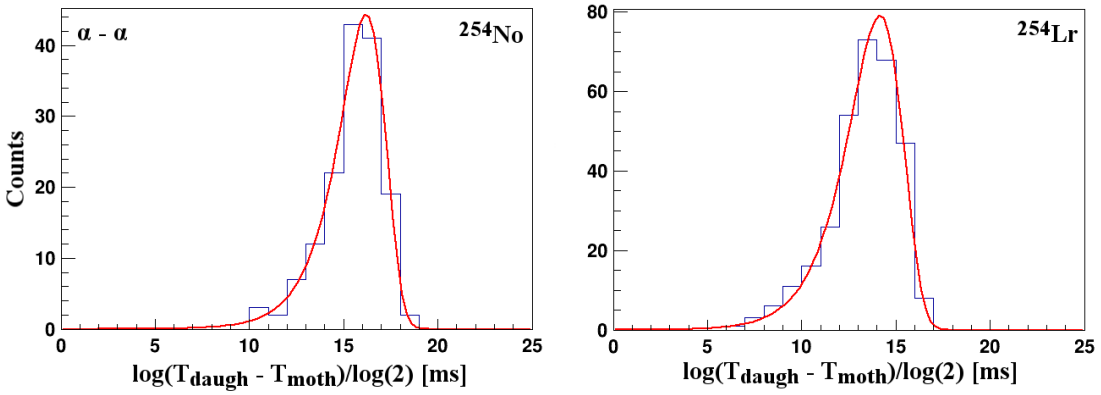

Figure 5.23: Left (Right): Logarithmic half life determination for ^{254}No (^{254}Lr) in a time window of 165 s (92 s). Data gathered in beam off periods.

A global half life of 18.5±1.2 s was determined, in a time window of 92 s, for the α decays of ^{254}Lr in the energy range of 8.35 to 8.55 MeV (figure 5.23 on the right hand side). The value is in agreement with the last reported value of 18.4±1.8 s [108]. The half lives of individual α lines (8405, 8444 and 8478 keV), in different energy ranges for ^{254}Lr, were determined and show differences among each other, but agree within the error bars (table 5.8).

E_α [keV]	i_α	$E_{\alpha_{range}}$ [keV]	$T_{1/2}$ [s]
All	1	8350 - 8550	18.5±1.2
8405 (14)	0.23	8350 - 8420	18.0±1.0
		8350 - 8440	19.0±1.5
8444 (14)	0.36	8420 - 8470	19.0±1.5
		8400 - 8490	18.5±1.5
8478 (14)	0.41	8470 - 8550	19.5±2.0
		8450 - 8550	19.0±1.5
8045 + 8444		8350 - 8470	19.0±1.5
		8350 - 8490	18.5±1.5
8444 + 8478		8420 - 8550	19.0±1.2
		8400 - 8550	18.6±1.5

Table 5.8: The half lives obtained for different α lines of ^{254}Lr. The correlation window used was 92 s. Results obtained for beam off periods.

To address the questions on the fine structure of ^{254}Lr and the possible assignment of the 9046 keV line to ^{258}Rf α decay, investigation of the γ and X-rays and

conversion electrons in coincidence with the α transitions is performed and will be discussed in the following section.
The γ-rays emitted in prompt coincidence with α decays of a mother nucleus must stem from the deexcitation of levels in the α decay daughter. The γ-rays coming from the deexcitation of ^{254}Lr will be detected in prompt coincidence with the α decay lines of ^{258}Db.
Several energy gates in different correlation procedures were used to probe the coincidence between α decays and γ-rays.

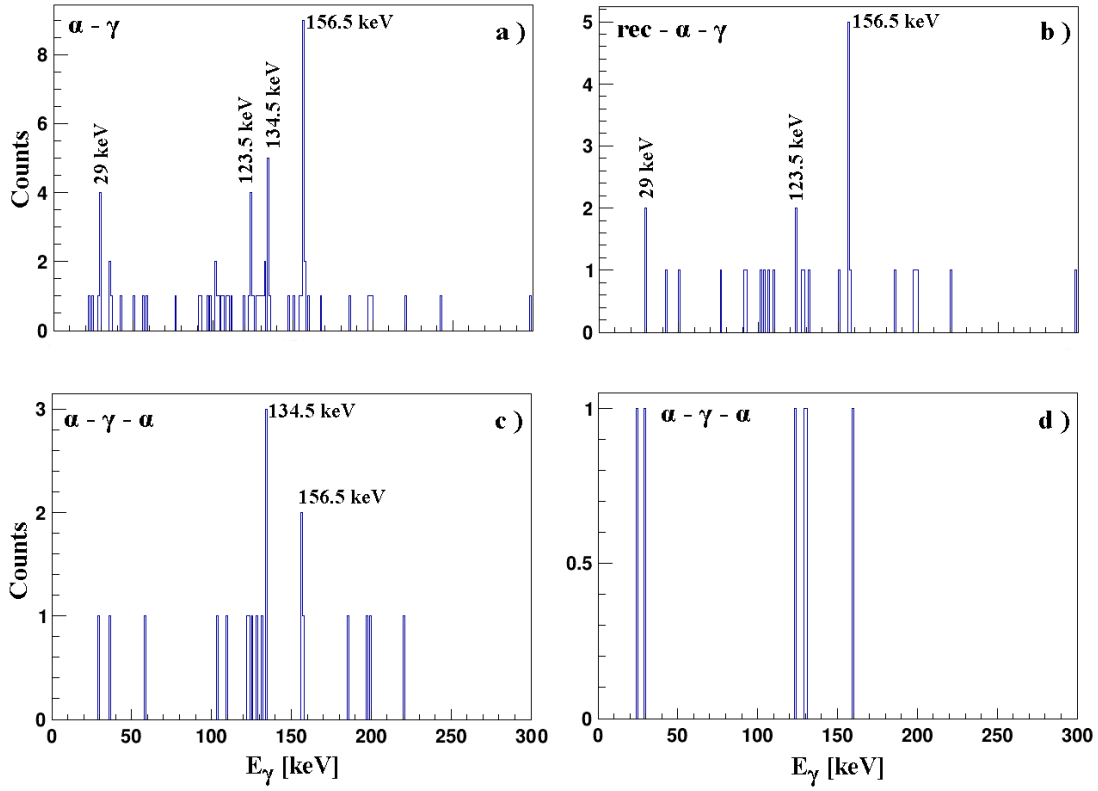

Figure 5.24: a) Gamma-rays in coincidence with α lines in the range between 9.0 and 9.4 MeV (^{258}Db). b) Gamma-rays in coincidence with α lines in the range 9.0 to 9.4 MeV (^{258}Db) correlated to a recoil in a time window of 22 s. c) Gamma-rays in coincidence with α lines in the range 9.0 to 9.4 MeV (^{258}Db) from the α-α correlations, the second α energy is in the range 8.35 to 8.55 MeV (^{254}Lr), the time window was 92 s. d) Gamma-rays in coincidence with α lines in the range 9.0 to 9.4 MeV (^{258}Db) from the α-α correlations, the second α energy is in the range 8.05 to 8.15 MeV (^{254}No), the time window was 275 s. Spectra are obtained in beam off periods.

The observed prompt γ-rays are registered in the same electronics event as the preceding α particle due to the fact that the time stamp of the registered events has a step of 1 μs. Consequently it is possible to investigate the correlation between α particles and prompt γ-rays without any correlation procedure. Energy gates applied either on the α or/and on the γ-ray energies enable first coincidence investigation. Figure 5.24 a) shows such a spectrum. This figure shows γ and X-rays in coincidence with α transitions in an energy range of 9.0 to 9.4 MeV (^{258}Db). However, to conclude to which isotope these transition belong to, it is necessary to further investigate the data. Figure 5.24 b) shows the γ and X-rays in coincidence with α transitions of ^{258}Db which are correlated to an ER within 22 s (section 5.2.2). Figures 5.24 c) and d) show the γ and X-rays in coincidence with the α decays of ^{258}Db correlated to the α decays of ^{254}Lr (8.35 to 8.55 MeV) and ^{254}No (8.05 to 8.15 MeV) respectively. It can be noted that figure d) does not show any γ-rays in coincidence with the α-α correlation between ^{258}Db and ^{254}No.

	E_x [keV]		
	No_{102}	Lr_{103}	Rf_{104}
K_{α_1}	127.357	130.611	133.381
K_{α_2}	120.953	123.867	126.302
K_{α_3}	119.987	122.887	125.407
K_{β_1}	143.506	147.110	150.279
K_{β_2}	147.531	151.227	154.494
K_{β_3}	141.977	145.496	148.550
K_{β_4}	148.100	151.181	155.097
K_{β_5}	144.323	147.944	151.113

Table 5.9: Characteristic X-rays for Lr, No and Rf [110].

Such a behavior is not surprising. As previously said ^{254}No can be produced in two ways. If it is produced through the EC decay of ^{254}Lr the γ and X-rays registered in coincidence with ^{258}Db will be found in coincidence with ^{254}Lr decay lines and not ^{254}No α decay lines. On the other hand, in the case that ^{254}No is produced from the α decay of ^{258}Rf. This α decay would then happen between two even-even isotopes and in such cases the transition is most probably going from ground to ground state so γ-rays are not expected [109]. This neither confirms nor denies the population of ^{254}No through the EC branch of ^{258}Db to ^{258}Rf.
To probe the structure of the ^{254}Lr isotope it is necessary to determine the correlation between different α transitions of ^{258}Db and the observed γ-rays. Energy gates were set on the single α lines of ^{258}Db to search for the γ-rays coming in coincidence. The opposite way was also done and different γ-rays were gated on

		Beam pause	^{254}Lr
E_γ [keV]	$E_{\gamma_{range}}$ [keV]	E_α (n.ev.) [keV]	E_α (n.ev.) [keV]
29	28 - 31	9027 (1) 9084 (1) 9175 (3)	9085 (1)
35	34 - 36	9116 (1) 9140 (1) 9155 (1)	9160 (1)
123	122 - 125	9000 - 9060 (2) 9130 - 9200 (4)	9160 (1) 9200 (1)
133	131 - 134	9020 (1) 9075 (1) 9100 (1)	9020 (1)
135	133 - 136	9020 - 9080 (5) 9187 (1)	9030 - 9070 (3)
157	155 - 158	9030 - 9160 (11) 9250 (1)	9100 - 9160 (3)
199	198 - 201	9115 (1) 9145 (1)	9115 (1)

Table 5.10: Alpha lines preceding the γ-rays listed. The positions in which nothing is written means that there was nothing seen. Column "^{254}Lr" means that the α decays are found in α-γ-α correlations, where the second α decay corresponds to a transition of ^{254}Lr (E gate 8.35 to 8.55 MeV).

to look for the α energy range in ^{258}Db to which they are correlated. The results of these investigations can be found in tables 5.10 and 5.11.
From table 5.11 it can be concluded that the transitions with energies 29 keV and 157 keV belong to ^{254}Lr as they are found to be correlated to the 9181 keV α decay as well as the decays with energies below 9.15 MeV of ^{258}Db. This is further confirmed by the results from the table 5.10 where the transitions with energies 29 keV and 157 keV come out as the strongest lines correlated to the 9181 keV α peak and the decays below 9.15 MeV. Additionally, the transitions with the energy of 123 keV and 135 keV can be observed in coincidence with the ^{254}Lr decays. However, this transitions are seen in coincidence with the low energy 9046 keV line, especially the 135 keV line. It is thus questionable if this transitions could be attributed to ^{254}Lr, it should be kept in mind that they are found in coincidence with the 9181 keV decay as well, or they are X-rays from ^{258}Rf. The energy resolution of the germanium detector of $\sim$ 2 keV FWHM leaves a possibility that they could be the X-rays of ^{258}Rf, as can be seen in table 5.9. However, a more detailed investigation with higher statistics would be needed to draw firm conclusions.

^{250}Md and ^{250}Fm

The third generation α transitions from the ^{258}Db and ^{258}Rf decay chains belong to the ^{250}Md and ^{250}Fm decays (figure 5.13).
The α decay energy of ^{250}Fm is 7.43 MeV (table 5.6). ^{211}Po was produced as a transfer product with an α decay energy of 7.45 MeV. Consequently the α decay of ^{250}Fm is mixed with the decay of ^{211}Po.
The α decay of ^{250}Md is visible in figures 5.19 a) and b), and in 5.25 on the left. An α-α correlation was performed in a time window of 260 s (5x$T_{1/2}$ of ^{250}Md, table 5.6 on the left hand side). The α decays of ^{250}Md can be seen in two energy ranges between 7.7 and 7.8 MeV and 7.8 and 8.0 MeV, indicating an existence of at least two separate decays. Additionally, considering the widths of these energy ranges one could assume that more than two α decays can be found.
A half life of 44$\pm$12 s was obtained for the decay of ^{250}Md. The obtained value is inside the error bars of previously reported half life of 52$\pm$6 s.

The investigation of the fine structure of ^{250}Md was performed using the γ and X-rays in coincidence with the α decay of ^{254}Lr in a similar way as described previously for the structure of ^{254}Lr (section 5.2.2).
Five different γ-ray transitions with energies 42 keV (7 events), 75 keV (3 events), 163 keV (2 events), 209 keV (2 events) and 306 keV (4 events) can be correlated to the α decay of ^{254}Lr (figure 5.25 on the right hand side). In order to determine the correlations between the α lines of ^{254}Lr and γ-ray transitions of ^{250}Md a variation of energy gates was used. The results of the investigation can be found

		Beam pause	TOF anticoinc.	^{254}Lr
$E_{\alpha_{moth}}$ [keV]	$E_{\alpha_{range}}$ [keV]	E_γ (n.ev.) [keV]	E_γ (n.ev.) [keV]	E_γ (n.ev.) [keV]
9046 (23)	9000 - 9050	123 (2) 135 (3)	123 (3) 135 (3)	 135 (2)
	9000 - 9070	123 (2) 135 (5) 157 (2)	123 (3) 135 (5) 157 (3)	 135 (3)
9099 (23)	9050 - 9150	35 (2) 133 (2) 135 (2) 157 (7)	 157 (9)	
	9030 - 9170	35 (2) 133 (2) 135 (4) 157 (9)	103 (3) 135 (4) 157 (12)	 135 (2) 157 (2)
9181 (23)	9150 - 9250	29 (2) 123 (2) 199 (2)	 	
	9130 - 9270	29 (2) 123 (2) 157 (2) 199 (2)	29 (3) 157 (4) 	
9270 (23)	9250 - 9360 9230 - 9360			

Table 5.11: Gamma-rays following the α decay of ^{258}Db. Different α energy ranges were tested to determine the structure of the daughter nucleus, ^{254}Lr. The positions in which nothing is written means that there was not a clear separation between γ-rays and background. The column named "TOF anticoinc." contains the beam on+off data. Column "^{254}Lr" means that the γ-rays are found in between two correlated α decays where the second α belongs to ^{254}Lr (energy gate 8.35 to 8.55 MeV).

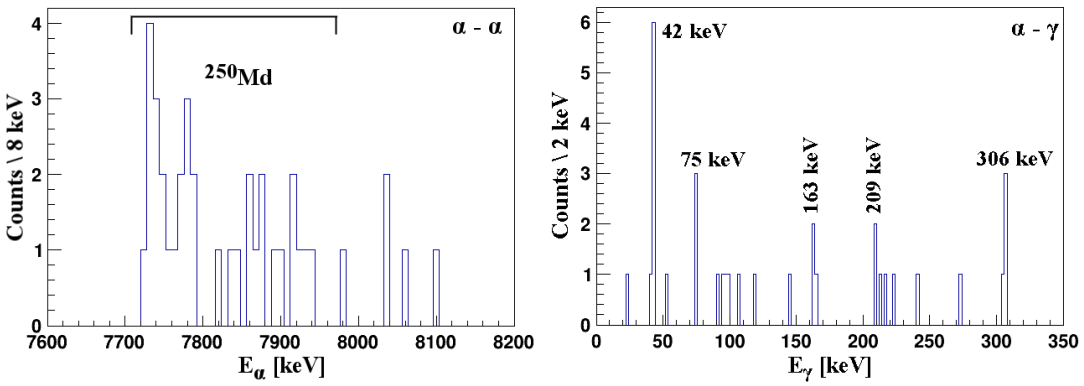

Figure 5.25: Left: Energy of the third generation α decay (^{250}Md) correlated to ^{254}Lr. A time window of 125 s was used. Right: Gamma-rays following the α decay of ^{254}Lr (energy range of α transitions 8.35 to 8.55 MeV). Spectra obtained in beam off periods.

in table 5.12. It can be concluded that the α decay of 8405 keV of ^{254}Lr is followed by a γ-ray of 75 keV, while the 8444 keV α decay is followed by a 42 keV γ-ray. Additionally a γ-ray transition of 306 keV can be seen in coincidence with 8405 keV α decay. The γ-ray of 160 keV is found in coincidence with both 8405 and 8444 keV lines, it could indicate that this is just one α decay of ^{254}Lr as was discussed previously in 5.2.2. However, it could also be that the correlation exists only with the 8405 keV decay since the two γ-rays are found in coincidence with the 8444 keV only when the energy gate is open. Without more statistics firm conclusions could not be drawn on the subject of 163 keV γ-ray line. Finally, the 42 keV line was found in coincidence with the 8478 keV α decay, however only when the energy gate was open and overlapping with the gate for the 8444 keV, consequently this transition can not be attributed to the 8478 keV line.
According to the obtained data a tentative level scheme for ^{250}Md is proposed and can be seen in figure 5.26.
The proposed level scheme is slightly modified compared to the previously published one. The modification is a consequence of a strong γ-ray transition of 75 keV visible in coincidence with the 8405 keV α decay. The 209 keV line is visible when gated on the complete energy range of the ^{254}Lr α decay, but not strictly in coincidence with a specific decay energy.

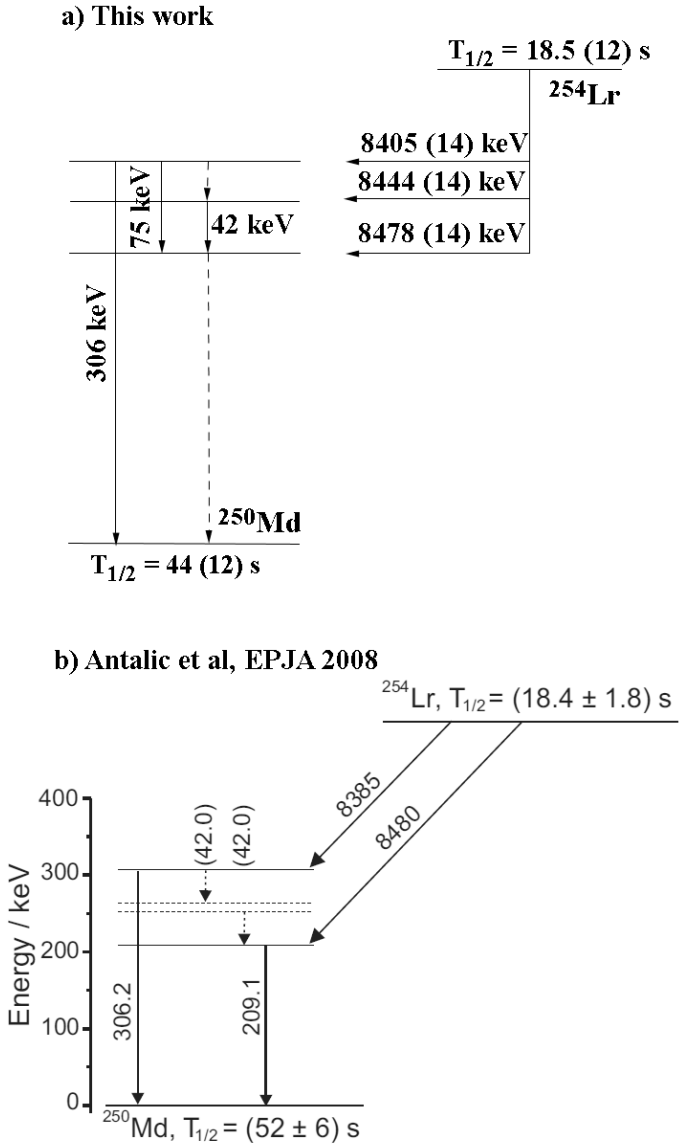

Figure 5.26: a) Tentative level scheme for ^{250}Md. b) Level scheme for ^{250}Md proposed in [108].

			Beam pause	TOF anticoinc.
$E_\alpha[keV]$	i_α	$E_{\alpha_{range}}$ [keV]	E_γ (n.ev.) [keV]	E_γ (n.ev.) [keV]
8405 (15)	0.23	8350 - 8420	75 (2) 163 (2) 306 (3)	75 (4) 163 (3) 306 (3)
		8350 - 8440	42 (4) 75 (3) 163 (2) 306 (3)	42 (3) 75 (5) 163 (3) 306 (3)
		8420 - 8470	42 (3)	43 (4)
8444 (15)	0.36	8400 - 8490	42 (5) 163 (2)	42 (6) 75 (3)
8478 (15)	0.41	8470 - 8530		
		8450 - 8550	42 (3)	42 (3) 65 (3)

Table 5.12: Gamma-rays following the α decay of ^{254}Lr. Different α energy ranges were tested to determine the structure of the daughter nucleus, ^{250}Md.

5.2.3 Conclusion

The motivation for the performed experiments was to address some open questions left from the previous studies. One of the key points was to investigate the existence of two states with different half lives in ^{258}Db. Further it was interesting to probe the α branch of ^{258}Rf which is produced through EC of ^{258}Db. Finally, the proposed level scheme of ^{250}Md is not complete, and the 163 keV γ-ray was not placed due to some ambiguities. Additionally it was not possible to fix the position of the 42 keV γ-ray, but rather, two possibilities for its placement were given.

^{258}Db was directly produced through the 1n channel of fusion evaporation reaction using ^{50}Ti beam on ^{209}Bi target at SHIP, GSI. Spectroscopy studies of ^{258}Db isotope and its daughter and grand daughter isotopes were performed in this thesis (section 5.2.2). The summary of obtained results on the α decay energies and corresponding half lives of all studied isotopes can be found in table 5.13. The attributed γ-rays can be found in table 5.14.

Two different half lives were observed for the α decay of ^{258}Db. The α decays with energy higher than 9.15 MeV are characterized with a shorter half life of 3.5±0.5 s. It was possible to separate two α decays with 9181 keV and 9270 keV in this energy range. The α decays with energies lower than 9.15 MeV have a slightly longer half

Isotope	E_α [keV]	i_α	$T_{1/2}$ [s]
^{258}Db (^{258}Rf)	9046 (23)	0.13	4.5±0.6
^{258}Db	9099 (23)	0.21	
	9181 (23)	0.56	3.5±0.5
	9270 (23)	0.10	
^{254}Lr	8405 (14)	0.23	18.5±1.2
	8444 (14)	0.36	
	8478 (14)	0.41	
^{254}No	8102 (14)		46±10
^{250}Md	7700 - 8000		44±12

Table 5.13: Energies and half lives of the isotopes studied in this work.

life of 4.5±0.6 s.
All α decays of ^{258}Db were found in coincidence with the α decays of ^{254}Lr indicating that ^{254}Lr emits all α particles from the same level. The obtained half life of ^{254}Lr is 16±1 s which is slightly shorter than the last reported value of 18±1.8 s. Few γ-ray transitions were found in coincidence with the α decays of ^{258}Db belonging to ^{254}Lr. Unfortunately, it was not possible to clearly separate the γ-rays from X-rays. Consequently, no conclusions were drawn on the populated levels of ^{254}Lr and no level scheme was proposed.

Isotope	E_γ [keV]	Preceded by: E_α [keV]
^{254}Lr	29	^{258}Db: 9181
	157	^{258}Db: 9099
^{250}Md	43	^{254}Lr: 8405
	306	
	75	^{254}Lr: 8444

Table 5.14: Gamma-rays attributed to the isotopes studied in this work.

The α decays of ^{250}Md were found in coincidence with the α decays of ^{254}Lr. It was again concluded that all decays of ^{250}Md are emitted from the same level. The obtained half life of 44±12 s is slightly lower than the previously reported one of 52±6 s, but is in agreement inside the error bars. Few γ-rays were found in coincidence with the α decay of ^{254}Lr belonging to deexcitation of ^{250}Md. A tentative level scheme, slightly different than previously proposed one, is proposed in figure 5.26.

^{254}No is produced through two different decay channels:

- ^{258}Db -> α -> ^{254}Lr -> EC -> ^{254}No

- ^{258}Db -> EC -> ^{258}Rf -> α -> ^{254}No

Populating ^{254}No through the EC of ^{254}Lr is well known and was previously investigated determining a β branch of 28.3±1.9% for ^{254}Lr. The EC of ^{258}Db to ^{258}Rf was also previously observed by studying the fission of ^{258}Rf. And similar results were obtained from the current study [109].
The α branch of ^{258}Rf was reported to be 30% by Gates [107]. We have seen indications of the α decay of ^{258}Rf. However, these indications suggest that the α branching of ^{258}Rf is much lower than the previously reported value of 30%. Detailed discussion can be found in section 5.2.2. Additional investigations using γ and X-rays are necessary to determine correctly the α branching ratio of ^{258}Rf.

Conclusion

Mechanisms which are responsible for the existence and stability of the superheavy nuclei are still not completely understood. They can be probed by synthesizing and studying the structure of transfermium (Z>100) elements. The isotopes in the vicinity of the $N = 152$ deformed shell gap are ideal candidates to study these mechanisms due to their increased stability. The nuclei of ^{257,258}Db are the ones which were chosen to perform this investigation in the presented manuscript.

^{257}Db was produced through the 2n channel of fusion-evaporation reaction at LISE, GANIL (chapter 4). Due to some technical difficulties following this experiment, only one third of the dedicated beam time was used for the spectroscopy of this isotope. Nevertheless, we have still been able to draw some conclusions on the structure and behavior of this nucleus. Two states, both decaying by α particle emission with different half lives, were identified. A half life of 2.2±0.6 s was attributed to the α decay with 8973 (24) keV energy. The α decay of 9177 (24) keV was characterized with a half life of 0.8±0.3 s. A clear separation in coincidences between the α decays of ^{257}Db and ^{253}Lr was observed. The 8973 keV ^{257}Db α line is followed by the 8808 (24) keV α of ^{253}Lr with a half life of 1.0±0.3 s, while the 9177 keV line is followed by the 8745 (24) keV α decay of ^{253}Lr with a half life of 2.0±0.5 s. Unfortunately, it was not possible to draw conclusions on the γ-rays found in coincidence with the ^{257}Db α decay. Thus, no level scheme was proposed. A followup experiment, performed at GANIL in spring 2015 with a completely new detector system, aimed at answering the questions which were still unresolved after the first experiment. However, the results of this experiment were not discussed in this work.

^{258}Db was produced through the 1n fusion-evaporation reaction channel at SHIP, GSI (chapter 5). Two α decays with 9181 (23) keV and 9270 (23) keV energies were identified and characterized with a half life of 3.5±0.5 s. Clear separation of the α decays in the energy range 9.0 to 9.15 MeV was not possible. Their half life was estimated to 4.5±0.6 s. Consequently, a strong indication of the existence of two levels with different half lives in ^{258}Db was found. From the correlations to ^{254}Lr, it was concluded that all α decays of ^{254}Lr are emitted from the same

level with a half life of 18.5±1.2 s. Few γ-rays from excited states in ^{254}Lr were found in coincidence with ^{258}Db α decays. However, it was not possible to deduce a tentative level scheme.
From the correlations between the α decays of ^{254}Lr and ^{250}Md, it was again concluded that all ^{250}Md α lines are emitted from the same level with a half life of 44±12 s. Few gamma-rays with 43 keV, 75 keV and 306 keV originating from the deexcitation of ^{250}Md, were found in coincidence with the α decays of ^{254}Lr. They were placed in a proposed partial level scheme of ^{250}Md (figure 5.26).
Finally, an indication of the α decay of ^{258}Rf to ^{254}No was observed, but the α decay branching ratio is indicated to be significantly smaller than previously reported by Gates [107].

The performed experiments provided new and confirmed information on the structure of the two studied isotopes. Nevertheless, the low statistics gathered during several performed experiments is not sufficient to allow firm interpretations of the data. To address these issues and provide better quality experiments in the region of superheavy nuclei, a new facility S^3 is being built at GANIL. This facility will provide a possibility for a higher production rate of these nuclei. It will be equipped with the new generation spectroscopy station, SIRIUS. This multi-detector system will contain two tracking detectors, a DSSD, a "Tunnel" detector and an array of germanium detectors. The tracking detectors for S^3 are currently under development at GANIL and at CEA, Saclay. The recent progress in their development is discussed in chapter 3.
The tracking detectors for S^3 are big size (200x100 mm^2) gas detectors working on the basis of secondary electron detection (SED). The spatial resolution is oscillating between 0.9 and 1.8 mm FWHM for strip and inter-strip positions respectively, depending on the prototype. A time resolution of 273 (10) ps FWHM was achieved for the real size SED prototype. These results are not far from the requirements set by the S^3 community, which are a spatial resolution of 1.5 mm FWHM and 300 ps FWHM. Some additional work still needs to be done to optimize the final detector.
Finally, this new facility will be able to produce, in the coming years, superheavy nuclei up to $Z = 115$ using both cold and hot fusion-evaporation reactions. For example, the isotope of $^{261}_{106}$Sg will be produced with two to ten times higher rates than it is produced nowdays at the existing facilities in cold fusion-evaporation reactions. The final goal of S^3 is to reach 20 fb cross section sensitivity. Consequently, this would permit better quality spectroscopy studies and, for example, enable determination of the spins and parities characterizing energy levels in ^{257,258}Db isotopes or the value of the α branching ratio of ^{258}Rf.

Conclusion

Les mécanismes responsables de l'existence et de la stabilité des noyaux super lourds ne sont à l'heure actuelle toujours pas totalement compris. Il est possible de les sonder au travers la synthèse et l'étude de la structure des noyaux transfermium ($Z > 100$). Les isotopes au voisinage de la fermeture de couche déformée $N = 152$ sont des candidats idéaux pour une telle étude du fait de leur stabilité accrue. Les noyaux de ^{257,258}Db sont ceux qui ont été choisis pour effectuer l'analyse présentée dans ce manuscrit.

Le ^{257}Db a été produit par réaction de fusion-évaporation, au travers de la voie 2n, sur LISE (GANIL, chapitre 4). Du fait de difficultés techniques, seulement un tiers du temps de faisceau n'a pu être utilisé pour effectuer la spectroscopie de cet isotope. Nous avons cependant été tout de même en mesure de tirer des conclusions quant au comportement et à la structure de ce noyau. Deux états décroissant par l'émission d'une particule α avec des temps de demi-vie différents ont été identifiés. Une demi-vie de 2.2±0.6 s a été attribuée à la décroissance α possédant une énergie de 8973 (24) keV. La décroissance de 9177 (24) keV a été associée à une demi-vie de 0.8±0.3 s. Une nette distinction des coïncidences entre les décroissances du ^{257}Db et du ^{253}Lr a été observée. La décroissance α de 8973 keV du ^{257}Db est suivie par la décroissance α de 8808 (24) keV du ^{253}Lr, associée à une demi-vie de 1.0±0.3 s. La raie à 9177 keV est quant à elle suivie par la décroissance α de 8745 (24) keV du ^{253}Lr, avec une demi-vie de 2.0±0.5 s. Malheureusement, il n'a pas été possible de conclure sur les rayonnements γ trouvés en coïncidence avec la décroissance du ^{257}Db. Ainsi, aucun schéma de niveaux n'a pu être proposé. Pour tenter de résoudre ce problème, une expérience a été effectuée au GANIL au printemps 2015, utilisant un tout nouveau système de détection. Les résultats de cette expérience, trop récente, n'ont pas été discutés dans ce manuscrit.

Le ^{258}Db a été produit par réaction de fusion-évaporation, au travers de la voie 1n, sur SHIP (GSI, chapitre 5). Deux décroissance α d'énergies 9181 (23) keV et 9270 (23) keV ont été observées et associées à un temps de demi-vie similaire de 3.5±0.5 s. D'autres raies α ont été observées entre 9.0 et 9.15 MeV sans possibilité de séparation. Leur temps de demi-vie a été estimé à 4.5±0.6 s. Cela constitue donc une forte indication de l'existence de deux niveaux d'énergie, aux temps de demi-vies différents, dans le ^{258}Db. Il a été conclu de l'observation des corrélations avec le ^{254}Lr que l'intégralité de ses décroissances α proviennent du même niveau d'énergie, avec un temps de demi-vie de 18.5±1.2 s. Plusieurs raies γ issues d'états excités du ^{254}Lr ont été trouvées en coïncidence avec les décroissances α provenant du ^{258}Db. Il n'a cependant pas été possible d'établir un schéma de niveau du fait principalement de la statistique trop faible.

De même, il a été déduit que l'ensemble des décroissances α du ^{250}Md proviennent du même état, avec un temps de demi-vie de 44±12 s. Là encore, plusieurs raies γ, issues de niveaux excités du ^{250}Md, ont été observées à 43 keV, 75 keV et 306 keV, et trouvées en coïncidence avec la décroissance du ^{254}Lr. Leur placement est indiqué dans le schéma de niveau partiel proposé figure 5.26.
Enfin, une indication de la décroissance α du ^{258}Rf vers le ^{254}No a été observée, avec un rapport de branchement significativement plus faible que ce qui avait précédemment été déterminé par Gates [107].

Les expériences analysées dans cette thèse ont permis de confirmer les résultats de précédentes études, ainsi que d'apporter de nouvelles informations sur les deux isotopes d'intérêt. Cependant, la faible statistique accumulée lors des différentes expériences n'a pas été suffisante pour permettre une interprétation non ambigüe des données. Pour répondre à ce genre de problème, ainsi qu'améliorer la qualité des expériences dans la région des noyaux super lourds, une nouvelle installation S^3 est en cours de construction au GANIL. Ce dispositif offrira la possibilité d'obtenir un taux de production plus élevé lors de la production de ces éléments et sera équipé de la station de spectroscopie dernière génération SIRIUS. Ce multi-détecteur sera composé de deux détecteurs dédié au suivi des produits de fusion-évaporation ("tracking"), un détecteur silicone à double face segmentées, un détecteur "Tunnel" ainsi que plusieurs détecteur germanium. Les détecteurs de "tracking" pour S^3 sont actuellement en développement au GANIL et au CEA de Saclay. Les récentes avancées dans leur développement ont été discutées au chapitre 3. Ces détecteurs sont des détecteurs gazeux de grande taille (200x100 mm^2) fonctionnant sur le principe de l'émission d'électrons secondaires (SED). Leur résolution spatiale varie de 0.9 à 1.8 mm FWHM pour les positions milieu de piste et entre-deux pistes respectivement. Une résolution temporelle de 273 (10) ps FWHM a été obtenue pour le prototype grandeur nature de SED. Ces résultats sont proches des prérequis imposés par la communauté S^3, à savoir une résolution spatiale de 1.5 mm FWHM et temporelle de 300 ps FWHM. L'optimisation finale du détecteur reste encore à faire.
Pour finir, cette installation sera capable, dans les années à venir, de produire des noyaux super lourds jusqu'à $Z = 115$ en utilisant aussi bien des réactions de fusion-évaporation chaudes ou froides. Par exemple, l'isotope de ^{261}Sg pourra être synthétisé avec un taux de production de deux à dix fois plus important que ce qui se fait, par réaction de fusion-évaporation froide, dans les installations existantes à l'heure actuelle. S^3 vise à atteindre une sensibilité en section efficace de 20 fb. Cela permettrait d'effectuer des études spectroscopiques de meilleure qualité, offrant entre autre la possibilité de déterminer les spins et parités des niveaux d'énergie des noyaux de ^{257,258}Db, ou encore les valeurs des rapports de branchement α dans le ^{258}Rf.

Bibliography

[1] W. Elsasser. Sur le principe de Pauli dans les noyaux II. *Journal de Physique et le Radium*, 5:253–356, 1934. (document)

[2] M. Goeppert-Mayer. On closed shells in nuclei II. *Physics Review*, 75:1969, 1948. (document), 1.1.2

[3] H.E. Suess O. Haxel, J.H.D. Jansen. On the «Magic numbers» in nuclear structure. *Physical Review*, 75:1766, 1949. (document), 1.1.2

[4] A. Ghiorso et al. New elements Einsteinium and Fermium, Atomic Numbers 99 and 100. *Physics Review*, 99:1048, 1955. (document)

[5] A. Ghiorso et al. Isomeric states in ^{250}Fm and ^{254}No. *Physical Review C*, 7:2032–2036, 1973. (document)

[6] J. Qian et al. Spectroscopy of ^{257}Rf. *Physics Review C*, 79:064319, 2009. (document), 4

[7] E. Minaya Ramirez et al. Direct mapping of shell effects in the heaviest nuclei. *Science*, 337:6099:1207, 2012. (document), 4

[8] K. Hauschild et al. High-K, t1/2 = 1.4(1) ms, isomeric state in ^{255}Lr. *Physical Review C*, 78:021302(R), 2008. (document), 4, 4.6, 5.2.3

[9] P.T. Greenlees et al. Shell-Structure and Pairing Interaction in Superheavy Nuclei: Rotational Properties of the Z=104 Nucleus ^{256}Rf. *Physical Review Letters*, 109:012501, 2012. (document)

[10] H.B. Jeppesen et al. Multi-quasiparticle states in ^{256}Rf. *Physical Review C*, 79:031303(R), 2009. (document), 4

[11] R.D. Herzberg. *The chemistry of superheavy elements*. Springer-Verlag Berlin Heidelberg, 2014. 1, 1.1.1, 1.1, 1.9, 5.2.3

[12] K. Heyde. *Basic ideas and concepts in nuclear physics, Second edition*. IOP Publishing, 1999. 1

[13] K.S. Krane. *Introductory nuclear physics*. John Wiley & Sons, Inc, 1988. 1

[14] J.S. Lilley. *Nuclear physics: Principles and Applications*. John Wiley & Sons, Itd, 2001. 1

[15] S. G. Nilsson and I. Ragnarsson. *Shapes and shells in nuclear structure*. Cambridge University Press, 1995. 1

[16] H.A. Bethe and R.F. Bacher. Stationary states of nuclei. *Review of Modern Physics*, 8:82, 1936. 1.1.1

[17] C.F. v. Weizacker. Zur Theorie der Kernmassen. *Zeitung fur physick*, 96:431, 1935. 1.1.1

[18] N. Bohr and J.A. Wheeler. The mechanism of Nuclear fission. *Physical Review*, 110:936, 1939. 1.1.1

[19] S.G. Nilsson et al. Binding states of Individual Nucleons in Strongly Deformed Nuclei. *Physical Review*, 99:1615–1617, 1955. 1.1.2

[20] B. J.P. Gall. Super et hyper déformations du noyau atomique: du discret au continu. *Annales de phusique France*, 24, 1999. 1.2, 5.2.3

[21] http://www.wiley.com/legacy/products/subject/physics/toi/toi.pdf. 1.4, 5.2.3

[22] R.R. Chasman et al. Survey of single-particle states in the mass region A>228*. *Review of Modern Physics*, 49:833, 1977. 1.5, 1.6, 5.2.3

[23] V.M. Strutinsky. Shell effects in nuclear masses and deformation energies. *Nuclear physics A*, 95:420–442, 1967. 1.1.2, 1.1.3

[24] R.-D. Herzberg and P.T. Greenlees. In-beam and decay spectroscopy of transfermium nuclei. *Progress in Particle and Nuclear Physics*, 61:674–720, 2008. 1.1.3, 1.1.4

[25] H. Meldner. Predictions of new magic regions and masses for super-heavy nuclei from calculations with realistic shell model single particle Hamiltonians. *Arkiv foer Fysik*, 36:593–8, 1967. 1.1.3

[26] S.G. Nilsson et al. On the nuclear structure and stability of heavy and superheavy elements. *Nuclear Physics A*, 131:1–66, 1969. 1.1.3

[27] M. Bender et all. Shell stabilization of super- and hyperheavy nuclei witwith magic gaps. *Physics Letters B*, 515:42–48, 2001. 1.7, 1.1.4, 5.2.3

[28] M. Bender and P.-H. Heenen. Self-consistent mean-fiels mmodel for nuclear structure. *Review of Modern Physics*, 75:122–180, 2003. 1.1.4, 1.2

[29] J. O. Rasmussen. Alpha-Decay Barrier Penetrabilities with an Exponential Nuclear Potential: Even-Even Nuclei. *Physical Review*, 113:1593, 1959. 1.3.1

[30] D.N. Poenaru and M. Ivascu. Estimation of the alpha decay half-lives. *Journal de Physique*, 44:791–796, 1983. 1.3.1

[31] E. Rurarz. Alpha emitters in the region from Ce to Os. *Acta Physica polonica B*, 14:917, 1983. 1.3.1

[32] A. Chatillon et al. Spectroscopy and single-particle structure of the odd-Z heavy elements ^{255}Lr, ^{251}Md and ^{247}Es. *European Physics Journal A*, 30:397–411, 2006. 1.11, 5.2.3

[33] Ch. Theisen et al. Internal conversion and summing effects in heavy-nuclei spectroscopy. *Nuclear Instruments and methods in physics research A*, 589:230, 2008. 1.3.3, 2.3, 5.2.2

[34] K. Eckerman and A. Endo. *MIRD: Radionuclide Data and Decay Schemes 2nd edition*. The Scociety of nuclear medicine, 2009. 1.3.3

[35] P. Walker and G. Dracoulius. Energy traps in atomic Nuclei. *Nature*, 399:35–40, 1999. 1.4, 1.12, 1.4, 5.2.3

[36] K.E.G. Lobner. Systematic of absolute transition probabilities of K-forbidden gamma-ray transitions. *Physics Letters B*, 26:369–370, 1989. 1.4, 1.4

[37] Y. Oganessian. Synthesis and Decay of Heaviest Nuclei with ^{48}Ca-Induced Reactions. *Nuclear Physics A*, 787:343c–352c, 2007. 2.1, 2.2, 5.2.3

[38] Private communication with Hongliang Lu. 2.1

[39] V. Zagrebaev and W. Greiner. Synthesis of superheavy nuclei: A search for new production reaction. *Physical Review C*, 78:034610, 2008. 2.1

[40] G.G. Adamian et al. Isotopic dependence of the production cross sections of superheavy nuclei. *Romanian Journal of Physics*, 57:9–17, 2012. 2.1

[41] W. Li et al. Fusion probability in heavy-ion collisions by a dinuclear-system model. *Europhysics Letters*, 64:750–756, 2003. 2.1

[42] K. Siwek-Wilczynska T. Cap and J. Wilczynski. Nucleus-nucleus cold fusion reactions analyzed with the l-dependent "fusion by diffusion" model. *Physical Review C*, 83:054602, 2011. 2.1

[43] Hongliang Lu et al David Boilley. Fusion hindrance of heavy ions: Role of the neck. *Physical Review C*, 84:054608–1, 2011. 2.1

[44] K-H. Schmidt and W. Morawek. The conditions for the synthesis of heavy nuclei. *Reports on Progress in Physics*, 54:949, 1991. 2.1

[45] K. Morita et al. Experiment on the Synthesis of Element 113 in the Reaction ^{209}Bi(^{70}Zn,n)^{278}113. *Journal of the Physics Society of Japan*, 73:2593–2596, 2007. 2.1

[46] Y.T. Oganessian et al. Synthesis of the isotopes of elements 118 and 116 in the Cf^{249} and Cm^{245}+Ca^{48} fusion reactions. *Physical Review C*, 74:044602, 2006. 2.1

[47] P. Ambruster. Nuclear structure in cold rearrangement processes in fission and fusion. *Reports on Progress in Physics*, 62:465–525, 1999. 2.1

[48] R. Anne et al. The Achromatic Spectrometer LISE at GANIL. *Nuclear Instruments and methods in Physics Research A*, 257:215–232, 1987. 2.2.1

[49] http://pro.ganil-spiral2.eu/laboratory/experimental-areas/lise. 2.2.1

[50] S. Grevy et al. Production of Super Heavy Elements at GANIL: Present status and Perspectives. *Journal of Nuclear and Radiochemical Sciences*, 3:9–12, 2002. 2.4, 2.2.1, 5.2.3

[51] R. Anne et A.C. Mueller. LISE3: a magnetic spectrometer-Wien filter combination for the secondary radioactive beam production. *Nuclear Instruments and Methods in Physics Research B*, 70:276–285, 1992. 2.2.1

[52] J. Rubert et al. First intense isotopic titanium-50 beam using MIVOC method. *Nuclear Instruments and methods in Physics Research B*, 276:33–37, 2012. 2.2.1

[53] G. Munzenberg et al. The Velocity Filter SHIP, Performance and Survey of Current Experiments. *Nuclear instruments and methods*, 186:423–433, 1981. 2.2.2, 2.2.2, 2.2.2

[54] http://www.gsi.de/en/research/accelerator_facility/linear_accelerator.htm. 2.2.2

[55] H. Savajols et al. S3: The Super Separator Spectrometer for LINAC Beams. Technical report, GANIL, 2010. 2.2.3

[56] A. Drouart et al. Fusion-evaporation studies with the Super Separator spectrometer (S^3) at Spiral2. *EPJ Web of Conferences*, 17:14004, 2011. 2.2.3, 2.2.3

[57] B.J.P. Gall et al. Pushing the limits of spectroscopy with S^3. *Acta physica polonica B*, 42:597, 2011. 2.2.3, 3

[58] F. Dechery et al. Toward the drip lines and the superheavy island of stability with the Super Separator Spectrometer S3. To be published in: European Physical Journal A. 2.7, 2.2.3, 2.8, 5.2.3

[59] C. Stodel et al. Targets for S3 at SPIRAL2. *Nuclear instruments and methods in Physics Research A*, 613:480–485, 2010. 2.2.3

[60] H. Savajols et al. S3 status report - SPIRAL2 Scientific Advisory Committee, SPIRAL2 Week 2011. Technical report, GANIL, 2011. 2.2.3

[61] R. Ferrer et al. In gas laser ionization and spectroscopy experiments at the Superconducting Separator Spectrometer (S^3): Conceptual studies and preliminary design. *Nuclear instruments and methodes in physics research B*, 317:570, 2013. 2.2.3

[62] A. Ghiorso et al. Positive identificaton of two alpha-particle-emitting isotopes of element 104. *Physical Review Letters*, 22:1317–1320, 1969. 2.3

[63] O.H. Odland et al. A fast position sensitive microchannel plate detector for ray-tracing of charged particles. *Nuclear Instruments and Methods in Physics Research A*, 378:149–154, 1996. 2.4.1, 3.2

[64] http://wiki.ganil.fr/gap/. 2.4.1, 2.4.1

[65] F. Azaiez et al. Exogam: a gamma-spectrometer for nuclear structure studies at SPIRAL. *Nuclear Physics News*, 7:21, 1997. 2.4.1

[66] W. Mittig. The SPIRAL project at GANIL and future opportunities. *Journal of Physics G: Nuclear and Particle Physics*, 24:1331–1339, 1998. 2.4.1

[67] http://wiki.ganil.fr/gap/wiki/Documentation/Software/Gru. 2.4.1

[68] http://pro.ganil-spiral2.eu/laboratory/detectors/exogam/the-exogam-wiki/electronic-data-acquisition/. 2.4.1

[69] N. Kurz J. Hoffmann and W. Ott. Development of ADC multiplexer for SHIP. Technical report, GSI, 2004. 2.4.2

[70] https://www.gsi.de/work/fairgsi/rare_isotope_beams/electronics/datenverarbeitung/datenerfassung/mbs.htm. 2.4.2

[71] https://www.gsi.de/en/work/fairgsi/rare_isotope_beams/electronics/data_processing/data_analysis/the_go4_home_page.htm. 2.4.2

[72] S3 development collaboration. ANR Project SIRIUS, 2013. 3

[73] J. Piot et al. S^3: Pushing spectroscopy forward. *Acta Physica Polonica B*, 43:285, 2012. 3

[74] H. Faure. *Développement et validation d'un nouveau détecteur silicium de grande taille pour S^3-SIRIUS*. PhD thesis, Université de Strasbourg, 2015. 3

[75] A. Drouart et al. Very large emissive foil detectors for the tracking of low-energy heavy ions. *Nuclear Instruments and Methods in Physics Reaserch A*, 579:1090, 2007. 3, 3.3.3

[76] F. Sauli. Principles of operation of multiwire proportional and drift chambers. CERN, 1976. 3.1, 3.3.1, 3.3.1, 3.6, 5.2.3

[77] G.F. Knoll. *Radiation Detection and Measurement: Third edition*. John Wiley & Sons, Inc, 1999. 3.1, 3.2, 5.2.3

[78] W.R. Leo. *Techniques for Nuclear and Particle Physics Experiments: a how to approach*. Springer-Verlag Berlin Heidelberg, 1987. 3.1, 3.3.1

[79] V. Palladino and B. Sadoulet. Application of classical theory of electrons in gases to drift proportional chambers. *Nuclear Instruments and Methods*, 128:323, 1975. 3.1.2

[80] A. Peisert and F. Sauli. Drift and diffusion of electrons in gases: A compilation. CERN, 1984. 3.1.2

[81] S.A. Korff. *Electrons and Nuclear Counters*. Van Nostrand, New York, 1955. 3.1.3

[82] G. Charpak et al. The use of multiwire proportional counters to select and localize charged particles. *Nuclear Instruments and Methods*, 62:262–268, 1968. 3.3.1

[83] A. Breskin. Progress in low-pressure gaseous detectors. *Nuclear Instruments and Methods*, 196:11–21, 1982. 3.3.1, 3.3.1

[84] Y. Giomataris et al. MICROMEGAS: a high-granularity position sensitive gaseous detector for high particle-flux environments. *Nuclear Instruments and Methods in Physics Research A*, 560:405–408, 1996. 3.3.2, 3.3.2

[85] M. Nakhostin. Performance of a low-pressure Micromegas-like gaseous detector. *Nuclear Instruments and Methods in Physics Research A*, 598:496–500, 2009. 3.3.2

[86] J. Pancin et al. Micromegas at low pressure for beam tracking. *JINST*, 7:CO3017, 2011. 3.3.2, 3.3.3, 3.4.2

[87] I. Giomataris et al. MicrOMEGAs in a bulk. *Nuclear Instruments and Methods in Physics Research A*, 560:405–408, 2006. 3.3.3

[88] P. Baron et al. AFTER, an ASIC for the readout of the large T2K time projection chambers. *IEEE Transaction on Nuclear science*, 55-3, 2008. 3.4.1

[89] S. Ottini-Hustache et al. CATS, a low pressure multiwire proportional chamber for secondary beam tracking at GANIL. *Nuclear Instruments and Methods in Physics Research A*, 431:476–484, 1999. 3.4.1

[90] W.H. Press et al. *Numerical Recipes in C: The art of scientific computing*. Cambridge University Press, 1992. 3.4.1

[91] D. Breton et al. Very high dynamic range and high sampling rate vme digitizing boards for physics experiments. *IEEE Transactions on Nuclear Science*, 52:2853–2860, 2005. 3.4.2

[92] Private communication with J. Pancin. 3.4.3, 3.5, 3.5

[93] M. Vostinar et al. Beam tracking with micromegas and wire chambers in secondary electron detection configuration. *JINST*, 8:C12023, 2013. 3.4.3, 3.24, 3.5, 5.2.3

[94] J. Pancin. Results of the in-beam tests of secondary electrons detectors on CIME at GANIL. Technical report, GANIL, 2010. 3.4.3

[95] B. Fernandez Martinez. *Estudio de Detectores Gaseosos de Electrones Secundarious a Baja Presion para el Trazado de Haces de Iones Pesados de Baja Energia*. PhD thesis, Universidad de Sevilla, 2014. 3.4.3

[96] F.P. Hessberger et al. The new isotope ^{258}105, ^{257}105, ^{254}Lr and ^{253}Lr. *Zeitschift fur Physik A: Atoms and Nuclei*, 322:557–566, 1985. 4, 4.2, 4.5, 5.2, 5.2.2, 5.2.3

[97] F.P. Hessberger et al. Decay properties of neutron-deficient isotopes ^{256,257}Db, ^{255}Rf and ^{252,253}Lr. *European Physics Journal A*, 12:57–67, 2001. 4, 4.2, 4.5, 4.13, 4.2, 4.14, 4.2.3, 4.2.4, 5.2.3, 5.2.3

[98] F.P. Hessberger et al. Decay properties of neutron-deficient isotopes of elements from Z=101 to Z=108. *European Physics Journal A*, 41:145–153, 2009. 4, 4.2, 4.5, 5.2, 5.2.2, 5.2.3

[99] F.P. Hessberger et al. Alpha-decay properties of ^{261}Bh. *European Physics Journal A*, 43:175–180, 2010. 4, 4.2, 4.5, 5.2.3

[100] B. Streicher. *Synthesis and spectroscopic properties of transfermium isotopes with Z =105, 106 and 107*. PhD thesis, Faculty of Mathematics, Physics and Informatics Comenius University, Bratisalva, 2006. 4.2, 4.2.3, 5.2

[101] J.M. Gates. *Cold fusion production and decay of neutron-deficient isotopes of Dubnium and development of excitation systems for group V elements*. PhD thesis, University of California, Berkeley, 2008. 4.2, 4.2.3, 5.2, 5.2.2

[102] http://www.nndc.bnl.gov/chart/. 4.5, 4.6, 5.6, 5.2.3

[103] A. Lopez-Martens et al. Isomeric states in ^{253}No. *European Physics Journal A*, 32:245–250, 2007. 4.2.2, 4.19, 4.2.2, 5.2.3

[104] P. Kuusiniemi et al. Decay studies of 215-217Th using Er-gamma-alpha-gamma coincidences. *European Physics Journal A*, 25:397, 2005. 4.2.2, 4.6, 5.2.3

[105] K. Hauschild et al. Isomer Spectroscopy in ^{216}Th and magicity of ^{218}U. *Physics Review Letters*, 87:072501–1, 2001. 4.2.2

[106] F.P. Hessberger et al. Decay studies of K isomers in ^{254}No. *European Physics Journal A*, 43:55–66, 2010. 5.1.3, 5.12, 5.2.3

[107] J.M. Gates et al. Synthesis of rutherfordium isotopes in the ^{238}U(^{26}Mg,xn)$^{264-x}$Rf reaction and study of their decay properties. *Physical Review C*, 77:034603, 2008. 5.2, 5.2.2, 5.2.3, 5.2.3

[108] S. Antalic et al. Decay studies of neutron-deficient lawrencium isotopes. *European Physics Journal A*, 38:219–226, 2008. 5.2, 5.2.2, 5.26, 5.2.3

[109] Private communication with F.P. Hessberger. 5.2.2, 5.2.2, 5.2.3

[110] C.M. Lederer and V.S. Shirley. Table of Isotopes. *Medical Physics*, 6:540, 1979. 5.9, 5.2.3

List of Figures

List of Tables

Abstract

Investigations on the nuclear structure in the region around $N = 152$ deformed shell gap provide an understanding of the existence of superheavy elements ($Z > 104$). Recent experimental studies have lead to the determination of the size and the strength of this gap. Its influence was studied for nuclei like $^{255}_{103}\mathrm{Lr}_{152}$ and $^{256}_{104}\mathrm{Rf}_{152}$. Valuable information can be obtained by studying further the evolution of the $N = 152$ deformed shell gap. To this purpose, the isotopes of $^{257}_{105}$Db and $^{258}_{105}$Db were produced and are the subject of this work. Even though these two isotopes were previously studied, the currently available data are limited and the level schemes are still not fully determined.
The ^{257}Db was produced through the fusion-evaporation reaction ^{209}Bi(^{50}Ti,2n)^{257}Db at GANIL. The two previously observed long lived states of ^{257}Db were confirmed in this experiment, as well as the two isomeric states of ^{253}Lr.
The ^{258}Db was produced through the fusion-evaporation reaction ^{209}Bi(^{50}Ti,1n)^{258}Db at GSI. A strong indication of the existence of two states in ^{258}Db with different half lives was observed. A new γ-ray transition of ^{250}Md was identified and its placement in the partial level scheme is proposed. The α decay of ^{258}Rf was also observed, suggesting a smaller branching ratio than previously reported.

Keywords: Nuclear spectroscopy, Nuclear structure, Radiative decay, Tracking detectors (nuclear physics), Gas detectors, Superheavy nuclei, $N = 152$ Shell gap

Résumé

L'étude de la structure des noyaux autour de la fermeture de couche déformée $N = 152$ offre des données capitales pour la compréhension de l'existence des éléments super lourds ($Z > 104$). Des expériences récentes ont conduit à la détermination de l'amplitude et de la constance de cette fermeture de couche. Son influence sur des noyaux tels que le ^{255}Lr et ^{256}Rf a été étudiée. L'étude plus poussée sur l'évolution de la fermeture de couche déformée $N = 152$ fournirait des informations précieuses quant à la formation des noyaux super lourds. A cette fin, les isotopes de ^{257}Db et ^{258}Db ont été produits et font l'objet de l'étude présentée dans ce manuscrit. Bien que ces deux noyaux aient déjà été étudiés précédemment, les données disponibles à l'heure actuelle sont limitées et ne permettent pas l'établissement d'un schéma de niveau complet.
Le ^{257}Db a été produit au GANIL par la réaction de fusion-évaporation ^{209}Bi(^{50}Ti,2n)^{257}Db. Les deux états de longue durée de vie observés précédemment ont pu être confirmés, ainsi que les deux états isomériques du ^{253}Lr.
Le ^{258}Db a été produit à GSI par la réaction de fusion-évaporation ^{209}Bi(^{50}Ti,1n)^{258}Db. Une forte indication de l'existence de deux états dans le ^{258}Db de durées de vie différentes a été observée. Une nouvelle transition γ dans le ^{250}Md a été identifiée et son placement dans le schéma de niveau partiel proposé. La décroissance α du ^{258}Rf a également été observée, suggérant un rapport de branchement plus faible que ce qui avait été mesurée auparavant.

Mots-clés: Spectroscopie nucléaire, Structure nucléaire, Décroissance radioactive, Détecteurs de traces (physique nucléaire), Détecteurs de gaz, Ions superlourds, Couches $N = 152$

Discipline: Constituants élémentaires et physique théorique

UFR Sciences, Campus 2 - Côte de Nacre, Boulevard du Maréchal Juin, 14032 Caen CEDEX
Laboratoire: GANIL - Bd. Henry Becquerel, 14076 CAEN Cedex 05